

1

[ATLAS Semivisible Jets]

2

[Elena Laura Busch]

3

Submitted in partial fulfillment of the
requirements for the degree of
Doctor of Philosophy
under the Executive Committee
of the Graduate School of Arts and Sciences

4

5

6

7

8

COLUMBIA UNIVERSITY

9

2024

10

© 2024

11

[Elena Laura Busch]

12

All Rights Reserved

13

Abstract

14

[ATLAS Semivisible Jets]

15

[Elena Laura Busch]

16

Abstract of dissertation (place-holder).

Table of Contents

18	Acknowledgments	xv
19	Dedication	xvi
20	Introduction or Preface	1
21	I Theory	2
22	Chapter 1: The Standard Model	3
23	1.1 Phenomenology: Particles and Forces	3
24	1.1.1 Particles	3
25	1.1.2 Forces	5
26	1.2 QCD and Jets	7
27	1.3 Symmetries	8
28	1.3.1 Spontaneous Symmetry Breaking and The Higgs Mechanism	9
29	1.4 Experimental Validation of the Standard Model	10
30	1.5 Limitations of the Standard Model	11
31	Chapter 2: Physics Beyond the Standard Model	13
32	2.1 Hidden Valley Models	13
33	2.2 Dark QCD	14

34	2.3 Semi-visible Jets	15
35	II Experiment	17
36	Chapter 3: The Large Hadron Collider	18
37	3.1 Accelerator Physics	19
38	3.1.1 The Journey of a Proton	19
39	3.1.2 Magnets	20
40	3.2 Luminosity	21
41	3.3 LHC Timeline	24
42	Chapter 4: The ATLAS Detector	26
43	4.1 Coordinate System and Geometry	27
44	4.2 Inner Detector	28
45	4.2.1 Pixel Detector	29
46	4.2.2 Semiconductor Tracker	31
47	4.2.3 Transition Radiation Tracker	31
48	4.3 Calorimeters	31
49	4.3.1 Liquid Argon Calorimeter	32
50	4.3.2 Tile Calorimeter	35
51	4.4 Muon Spectrometer	36
52	4.5 Magnet System	38
53	4.6 Forward Detectors	39
54	4.7 Trigger and Data Acquisition	40

55	Chapter 5: Particle Reconstruction and Identification	44
56	5.1 Inner Detector Tracks	44
57	5.2 Photons and Electrons	45
58	5.3 Muons	47
59	5.4 Jets	49
60	5.4.1 Calorimeter Clusters	50
61	5.4.2 Particle Flow Algorithm	51
62	5.4.3 Jet Clustering	52
63	5.4.4 Ghost Track Association	55
64	5.5 Missing Transverse Energy	56
65	III Search	58
66	Chapter 6: Monte Carlo and Data	59
67	6.1 Data	59
68	6.2 Simulation	60
69	6.2.1 Simulated Backgrounds	60
70	6.2.2 Signal Simulation	61
71	Chapter 7: Machine Learning Tools	64
72	7.1 Introduction	64
73	7.1.1 Particle Flow Network (Supervised)	65
74	7.1.2 ANTELOPE (Semi-supervised)	75
75	Chapter 8: Analysis Strategy	82

76	8.1 Preselection	82
77	8.2 SVJ Fit and Discovery Analysis Strategies	84
78	8.3 Analysis Regions	88
79	8.3.1 Control and Validation Regions	88
80	8.3.2 Signal Region	90
81	8.4 Background Estimation	92
82	8.5 Fit Strategy and Validation	93
83	8.5.1 SVJ Fit Strategy	93
84	8.5.2 Discovery Strategy	102
85	Chapter 9: Results	105
86	Conclusion or Epilogue	106
87	References	110
88	Appendix A: Trigger Studies	116
89	Appendix B: Machine Learning Approaches	120
90	B.1 Unsupervised: AE vs. ANTELOPE	120
91	B.2 PFN Optimality Checks	121
92	B.3 Supervised: BDT vs. PFN	124
93	B.4 Single Jet vs Jet System ML Approach	124
94	B.5 PFN Training Composition	126
95	B.6 E_T^{miss} and $E_T^{\text{miss}}\phi$ Shapes	128

96	B.6.1 NCB Preselection	128
97	B.6.2 TileCal Correction	130
98	Appendix C: Truth Studies	133
99	C.1 Jet dR Matching	133
100	Appendix D: BumpHunter	135
101	D.1 Signal Mass Resolution m_T Binning	135

List of Figures

103	1.1	Diagram of the 17 particles comprising the Standard Model	4
104	1.2	Fundamental particle interactions of the three fundamental forces described by the	
105		Standard Model [2].	6
106	1.3	An example Feynmann diagram of jet production	7
107	1.4	An illustration of the “hat shaped” potential of the Higgs field, resulting in a non-	
108		zero vacuum expectation value.	9
109	2.1	Illustration of the hidden valley potential.	14
110	2.2	The massive mediator particle Z' of the s-channel realization of a HV model . . .	14
111	3.1	The LHC accelerator complex at CERN [29]	20
112	3.2	The octants of the LHC and location of various beam activities [28]. Stars indicate	
113		the locations of beam collisions, and the associated detectors recording the	
114		outcome of those collisions.	21
115	3.3	(Left) Total integrated luminosity over the course of Run 2. (Right) Average num-	
116		ber of pp interactions per bunch crossing in Run 2. Each curve is weighted by the	
117		integrated luminosity for the year.	23
118	3.4	Timeline of LHC and HL-LHC activities [31]. Integrated luminosity estimates are	
119		approximate, and not reflective of the exact amount delivered to each experiment. .	25
120	4.1	The ATLAS detector [34].	26
121	4.2	ATLAS coordinate system and geometry	29
122	4.3	A 3D visualization of the structure of the ID in the barrel region [35]	30

123	4.4 A 3D visualization of the structure of the ID end-caps [34]. The paths of two charged particles ($\eta = 1.4$ and 2.2) are illustrated.	30
124		
125	4.5 ATLAS calorimetry system [36]	32
126		
127	4.6 Diagram of a segment of the EMB, demonstrating the accordion plate arrangement [37]	33
128		
129	4.7 A LAr pulse as produced in the detector (triangle) and after shaping (curve) [37] . .	34
130		
131	4.8 Readout gap structure in HEC [37]	35
132		
133	4.9 TileCal wedge module [40]	36
134		
135	4.10 Cross section view of the muon spectrometer system [41]	37
136		
137	4.11 Layout of the barrel and end-cap toroid magnets [34]	39
138		
139	4.12 Block diagram of the L1 trigger process. The overall L1 trigger decision is made by the CTP [34].	41
140		
141	4.13 Block diagram of the trigger and data acquisition processes, including L1 and HLT processes [45].	42
142		
143	5.1 Graphic illustrating the various objects and high level features identified by ATLAS object reconstruction, and their interaction with different systems of the ATLAS detector [46]	45
144		
145	5.2 Track reconstruction seeding, finding and fitting illustration [47]	46
146		
147	5.3 Three types of EM object candidates [49].	47
148		
149	5.4 Four types of muon track candidates [51].	49
150		
151	5.5 The fragmentation and hadronization processes undergone by a quark produced in a proton-proton collision [53].	50
152		
153	5.6 A flow chart illustrating the particle flow algorithm progression [58].	53
154		
155	5.7 A comparison of jet clustering with four different jet algorithms. The anti- k_t algorithm is observed to create the most conical jets, where the shape of the jet is immune to the presence of soft radiation [54].	54
156		

149	5.8 A comparison of MC simulation and data for $Z \rightarrow \mu\mu$ events where real $E_T^{\text{miss}} = 0$ [65]. The resolution of the missing energy in the transverse ($x - y$) plane is observed to increase with increasing total $\sum E_T$	57
150		
151		
152	6.1 The transverse momentum slices of the QCD MC simulation, overlayed to show how they come together to create a smooth distribution (left) once weighted properly. The original unweighted distribution is shown on the right, illustrating the enhanced statistics for the high p_T range.	61
153		
154		
155		
156	6.2 Background processes relevant to the SVJ signal. The agreement between the black line (data) and grey line (all MC processes combined) illustrates that this collection of background processes is sufficient to model the expected E_T^{miss} in the selected data events.	62
157		
158		
159		
160	7.1 The Energy/Particle Flow Network concept, from Ref. [71].	66
161		
162		
163		
164	7.2 An annotated diagram of the PFN architecture. y and ϕ represent geometric information for the input particles, z represents energy information, and PID encompasses any other particle ID information in the input.	66
165		
166	7.3 A illustration of the expected dijet behavior of semi-visible jets, where one jet is closely aligned with E_T^{miss}	67
167		
168		
169	7.4 Illustration of track coordinates d_0 and z_0	68
170		
171		
172		
173	7.5 Distributions of the track multiplicity in the leading and subleading jets, comparing signal and background PFN training samples.	68
174		
175		
176		
177		
178		
179	7.6 A diagram demonstrating how the two jet system is rotated in (ϕ, η)	69
170	7.7 The 6 PFN track variables in background MC and signal MC. There are some differences between signal and background, but the track kinematics are largely similar.	69
171		
172		
173	7.8 The 6 PFN track variables in data and background MC, after the scaling and rotation procedure is applied. There is excellent modeling of the data by the MC within the track variables. The slight discrepancy in the phi distribution is due to the modeling of dead TileCal cells by the QCD MC, which will be discussed in Chapter 8. The level of discrepancy is determined to be within tolerance given that the final result will be data driven and the QCD model is used in the PFN training only.	70
174		
175		
176		
177		
178		
179		

180	7.9 PFN score for background MC, data, and signal, comparing a PFN training on 181 QCD-only vs all-background MC samples. The average AUC for the QCD-only 182 training (left) is 0.93, while the average AUC for the mixed background training 183 (right) is 0.84. The sensitivity estimate across the grid is better for the QCD-only 184 training - from the distribution we can conclude that this is because the sensitivity 185 to MET enhanced signals is greatly reduced.	72
186	7.10 PFN architecture loss during training as a function of epoch (left) and the evaluated 187 loss over the signal and background (right).	72
188	7.11 ROC the PFN score for combined signal (true positive) and QCD background (false 189 positive).	73
190	7.12 AUC from the PFN score for each signal in the SVJ grid, shown versus the QCD- 191 only training sample.	74
192	7.13 PFN score for two signals and the total background MC (top), and between data 193 and MC (bottom). The difference between data and MC efficiency is minimal (< 194 5%).	74
195	7.14 A visual representation of the 64 PFN latent space variables which create the input 196 of the VAE component of ANTELOPE. The left shows a 2D histogram of the PFN 197 latent space index (0-63) versus the value assumed by that index. The right shows 198 1D histograms of two particular PFN latent space variables.	76
199	7.15 An annotated diagram of the ANTELOPE architecture.	77
200	7.16 ANTELOPE architecture loss during training as a function of epoch.	78
201	7.17 ANTELOPE score distribution comparing data and the total background MC (left), 202 with good agreement observed between data and simulated background, and com- 203 paring all background MC to signals (right), revealing good discrimination power. 204	79
205	7.18 AUC from the ANTELOPE score for each signal in the SVJ grid.	80
206	7.19 Comparing data and the alternate signal models for the PFN score (left) and AN- 207 TELOPE score (right). The emerging jet signal is an example of the gain of the 208 model-independent ANTELOPE approach, where it has a bimodal shape in PFN 209 score but is clearly tagged as anomalous by ANTELOPE.	81

210	7.20 Comparing data and the alternate signal models in terms of sensitivity (S/\sqrt{B}) for 211 the PFN and ANTELOPE tools, applying the selection that is used in the analysis. 212 The ANTELOPE network is found to provide significant added sensitivity to alter- 213 nate signals such as the gluino → R-hadron and emerging jets, which have higher 214 E_T^{miss} than the SVJs.	81
215	8.1 Preselection cutflow for data (left) and signal (right).	83
216	8.2 Energy and momentum analysis variables at preselection, for data, all background 217 MC and representative signal models. m_T is the key fit variable, and this plot 218 illustrates the smoothly falling background in comparison to the resonant shape of 219 the signals. m_T is further illustrated in Figure 8.9.	85
220	8.3 Orientation analysis variables at preselection, for data, all background MC and 221 representative signal models. While $\Delta\phi(E_T^{\text{miss}}, j)$ variables are not used explicitly 222 in the analysis flow, they help create a picture of the event.	86
223	8.4 Flow of analysis selections, regions, and background estimation/validation fitting 224 strategy. TODO: diagram needs to be corrected	87
225	8.5 Distributions of the subleading jet width width_{j2} (left) and leading jet with width_{j1} 226 (right) in data, background MC and signals at preselection. All SVJ signals are 227 seen to be wider than the background in width_{j2} . The same is not true for width_{j1} , 228 where some signals are observed to closely match the background.	88
229	8.6 2D plots revealing correlations between width_{j2} and m_T (left), width_{j2} and ML 230 score (middle), and m_T with ML score (right). For the top row, the ML score is 231 the PFN score, and for the bottom three, the ML score is the ANTELOPE score. 232 Minimal correlations are observed and are shown to not sculpt m_T , validating these 233 variables for analysis region construction and statistical treatment.	89
234	8.7 m_T in simulation across the CR, VR, and SR for both PFN (left) and ANTELOPE 235 (right) selections.	90
236	8.8 Definition of CR, VR, and SR regions using width_{j2} and the ML score, along with 237 the population of each region in data statistics. The SVJ Fit region is shown on top 238 with the PFN score on the x-axis, and Discovery region is shown on the bottom, 239 with the ANTELOPE score on the x-axis.	91
240	8.9 The resonant shape of the SVJ signals in m_T , in contrast to the smoothly falling 241 m_T background. The high R_{inv} signals (right) boast a wider shape, making them 242 more difficult to detect, while the low R_{inv} signals(left) produce a more narrow 243 resonance in m_T	92

244	8.10 Background-only m_T fits using representative MC in the CR (left), VR (middle), 245 and SR (right).	94
246	8.11 Background-only m_T fits using data in the full statistics CR and VR regions.	95
247	8.12 Post-fit parameters for the PFN CR and VR. $p1$ can also be considered N_{bkg} or the 248 normalization factor.	95
249	8.13 m_T distribution in the data CR, before (left) and after (right) smoothing.	96
250	8.14 Background-only m_T fits using pseudo-data from the CR template.	97
251	8.15 p -value histograms from 100 fits to Asimov data in the CR.	97
252	8.16 Example S+B fits on a background m_T spectrum with injected signal from the point 253 ($2500 \text{ GeV}, R_{inv}=0.2$).	98
254	8.17 Measured signal at a variety of injected values (1x, 2x, and $5\sqrt{b}$), for all signal 255 points in the grid, $R_{inv}=0.2$ (top left), 0.4 (top right), 0.6 (bottom left), and 0.8 256 (bottom right).	99
257	8.18 95% C.L. upper limits for signal models across Z' mass, for four different R_{inv} frac- 258 tions, from the CR region (without systematics).	100
259	8.19 Post-fit function and residuals for the ANTELOPE CR and VR.	102
260	8.20 Post-fit parameters for the ANTELOPE CR and VR.	103
261	8.21 BumpHunter fits on the ANTELOPE m_T spectra for both the CR (left) and VR 262 (right). In a signal-depleted region, good agreement with the background estima- 263 tion is observed.	104
264	8.22 BumpHunter p-values extracted for 100 Asimov toys for both the ANTELOPE CR 265 (left) and VR (right).	104
266	A.1 Trigger yield and efficiency for both the MET trigger and small-R jet trigger ap- 267 proach. Each entry represent a signal point, labelled by the Z' mass and the 268 R_{inv} fraction.	116
269	A.2 The factor of improvement in S/\sqrt{B} for each trigger method compared to the un- 270 triggered case.	117
271	A.3 The ratio of S/\sqrt{B} of jet trigger over E_T^{miss} trigger selection.	117

272	A.4 Analysis variables where high R_{inv} signals a clearly distinct from background and 273 low R_{inv} variables. On the contrary, leading jet p_T is one of the only variables 274 where low R_{inv} signals are distinct from background.	119
275	A.5 OR of jet and E_T^{miss} triggers.	119
276	B.1	120
277	B.2	121
278	B.3 AUC from the PFN score for each signal in the SVJ grid, shown versus the QCD- 279 only training sample (top) and the total MC background (bottom). Note the three 280 missing points will be added shortly - they were delayed due to a DAOD production 281 mistake.	122
282	B.4 Comparison of PFN AUC (top), SIC (middle), and sensitivity in the m_T mass win- 283 dows (bottom) for a single PFN model (left) vs. two models, trained on $R_{inv} < 0.5$ 284 and > 0.5 separately.	123
285	B.5 Preferred cuts on the PFN score for each point in the grid, comparing the effect of 286 adding the NCB preselection.	124
287	B.6 Scans done to check for optimality of PFN training parameters.	125
288	B.7	125
289	B.8 ϕ Performance comparison between single jet and jet system ML approach	126
290	B.9 ϕ Comparison in the AUC score across the grid for the mixed background strategy 291 vs the QCD only strategy. The bottom table highlights that the QCD only strategy 292 gives superior sensitivity across the signal grid.	127
293	B.10 E_T^{miss} in data before and after Tight event cleaning is applied.	128
294	B.11 E_T^{miss} vs jet1 p_T in data before and after Tight event cleaning is applied.	129
295	B.12 η vs ϕ for leading and subleading jets, before and after the application of tight 296 cleaning.	129
297	B.13 Added NCB preselection and impact on E_T^{miss} shape.	130
298	B.14 NCB preselection impact on data and signal yields.	131
299	B.15 Impact of tight cleaning and non-collision background preselection.	132

300	B.16 $E_T^{\text{miss}}\phi$ in data, before (left) and after (right) application of the TileCal correction	
301	tool.	132
302	C.1 Index of jets truth matched (by requirement of $\Delta R < 0.4$) with dark quark.	133
303	C.2 Percent of jets with $\Delta R(j, E_T^{\text{miss}}) < 0.4$ comparing two jet identification strategies.	
304	Leading and subleading jets are seen to be the better metric for identifying jets	
305	associated with the dark quark decay.	134
306	D.1 Example determinations of the 60% mass window means for several signal points.	136
307	D.2 Signal mass resolution for m_T binning for the signal grid in (R_{inv} , mass) space.	136
308	D.3 m_T bins based on the signal mass resolution and the minimum 100 GeV width	
309	requirement, for each R_{inv} signal category.	137

List of Tables

311	4.1 General performance goals of the ATLAS detector [34].	27
312	6.1 Fixed parameters in the Pythia8 HV model	63
313	6.2 Values for m_{dark}	63
314	6.3 Mass points and cross sections of the SVJ search signal grid	63

315

Acknowledgements

316 Insert your acknowledgements text here. This page is optional, you may delete it if not

317 needed.

318

Dedication

319

Dedicated to my friends and family

320

Introduction or Preface

321 Insert your preface text here if applicable. This page is optional, you may delete it if not
322 needed. If you delete this page make sure to move page counter comment in thesis.tex to correct
323 location.

324

Part I

325

Theory

Chapter 1: The Standard Model

328 The Standard Model of particle physics is a universally accepted framework which explains
 329 the interactions of fundamental particles. All known fundamental particles, outlined in Figure
 330 1.1, are represented in the Standard Model. The model describes three of the four known forces:
 331 the electromagnetic force, the weak force, and the strong force. Gravity, the fourth fundamental
 332 force, is not addressed by the Standard Model. The Standard Model was primarily developed over
 333 the course of the 1960s and 1970s, by combining the work of many physicists into one coherent
 334 model. The Standard Model has been established as a well-tested theory by decades of experimen-
 335 tal physics research.

336 This chapter will seek to introduce the phenomenology and mathematical foundations of the
 337 Standard Model, and present the supporting experimental evidence. Phenomenon which are unex-
 338 plained by the Standard Model such as gravity will be considered at the end of the chapter, leading
 339 to an exploration of theories beyond the Standard Model in the subsequent chapter.

340 **1.1 Phenomenology: Particles and Forces**

341 1.1.1 Particles

342 A classic representation of the particles comprising the Standard Model is shown in Figure
 343 1.1. The two primary particles classes are bosons (gauge bosons and the scalar Higgs boson) and
 344 fermions (leptons and quarks). The bosons are carriers of fundamental forces, while the fermions
 345 are the building blocks of matter. Fermions are sorted into three *generations*, and each fermion is
 346 identified by a unique *flavor*.

347 Each entry in the table in Figure 1.1 is accompanied by 3 characteristic numbers: mass, charge,
 348 and spin. The mass of each particle is determined to limited precision by experimental observation,

Standard Model of Elementary Particles

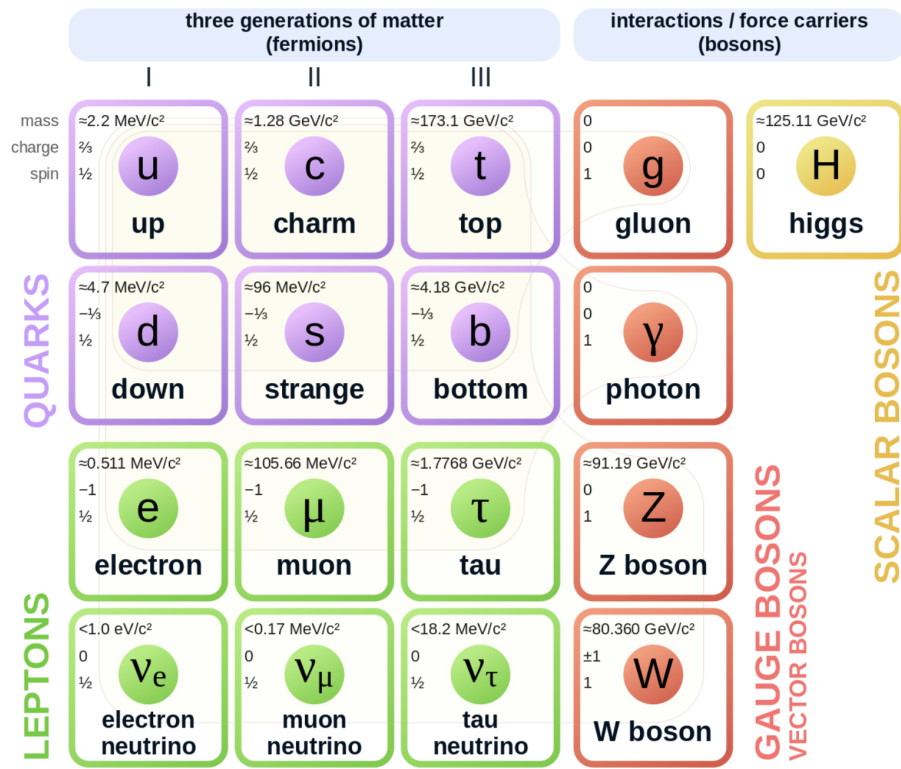


Figure 1.1: Diagram of the 17 particles comprising the Standard Model

349 with the exception of photons and gluons which are known to be massless. Charge refers to the
350 electromagnetic charge, which is integer for leptons and fractional for quarks. Spin is an intrinsic
351 form of angular momentum carried by fundamental particles; all fermions have half integer spin,
352 while bosons have integer spin.

353 Each particle is also known to have an *antiparticle*. Each antiparticle has the same mass but the
354 opposite charge of their Standard Model counter part; for example, the antiparticle of the electron
355 is the positron, which has all the same properties but a positive charge. The photon, Z boson,
356 and Higgs are each their own antiparticle. The nature of antineutrinos is an open question driving
357 neutrino physics research, as it is not currently known whether neutrinos are their own antiparticle.

358 1.1.2 Forces

359 The three fundamental forces explained by the Standard Model are the electromagnetic force,
360 the strong force, and the weak force. The photon is the carrier of the electromagnetic force, which
361 dictates the nature of interactions between electrically charged particles, and is widely covered by
362 introductory physics courses. The electromagnetic force has an infinite interaction range, a result
363 of the massless and non-self interaction nature of the photon. The electromagnetic interaction is
364 described by the theory of quantum electrodynamics (QED).

365 The weak force gives rise to atomic radiation and decay. It allows for the processes of beta
366 decay, which enables conversion between neutrons and protons within the nucleus of an atom. In
367 the process of beta decay, a proton decays into a neutron, a positron, and a neutrino; or, a neutron
368 decays into a proton, an electron and an antineutrino. The weak interaction allows for quark flavor
369 mixing, the which enables beta decay. The W^+ , W^- , and Z^0 are the force carriers of the weak force.
370 The effective range of the weak force is limited to subatomic distances, as a result of the massive
371 nature of the mediator bosons. The unified theory of the electroweak interaction posits that at high
372 enough energies the electromagnetic interaction and the weak force merge into the same force.
373 This threshold is termed the unification energy and calculated to be about 246 GeV [1].

374 The strong force confines quarks into hadron particles, such as protons and neutrons. The

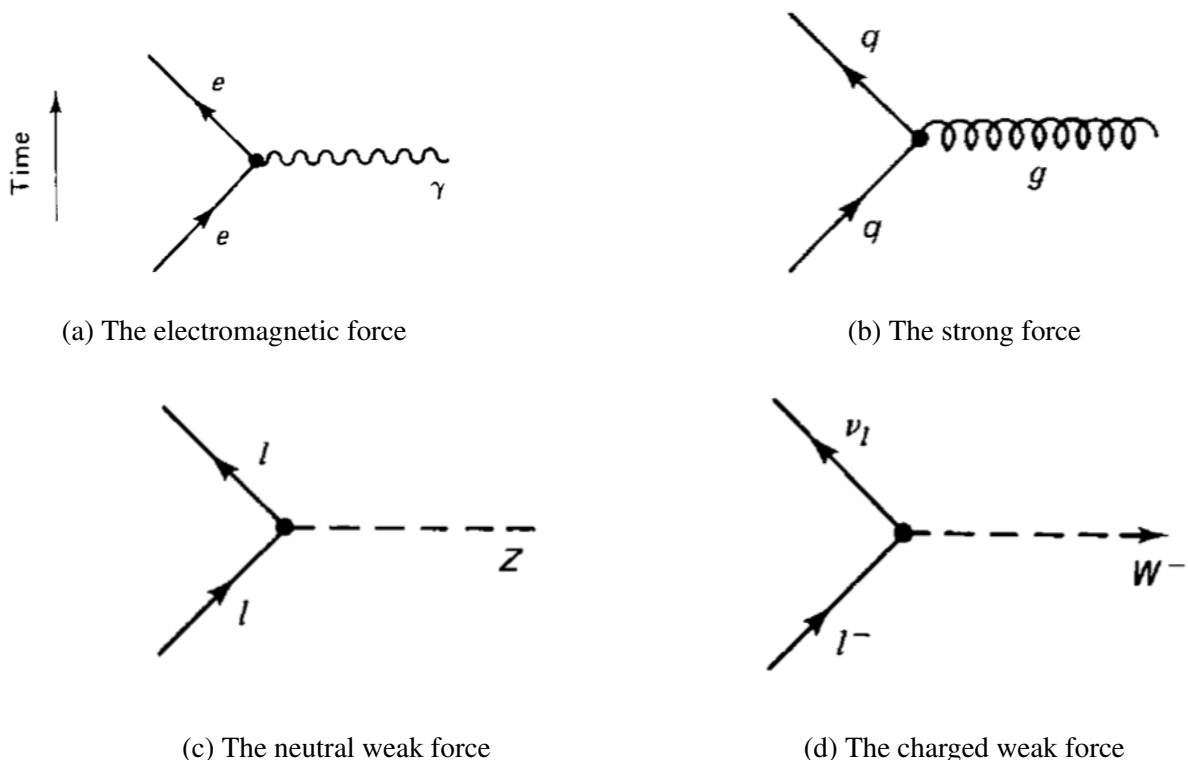


Figure 1.2: Fundamental particle interactions of the three fundamental forces described by the Standard Model [2].

375 strong force also allows for the creation of atomic nuclei by binding protons and neutrons together,
376 and is generally referred to as the “nuclear force” in this context. The gluon is the mediator of
377 the strong force, which is a short-range force which acts at subatomic distances on the order of
378 10^{-15} m. At this range, the strong force is about 100x as strong as the electromagnetic force,
379 which allows for the creation of positively charged nuclei [2]. The strong force is described by the
380 theory of quantum chromodynamics (QCD). In the same way that QED dictates the interaction of
381 electrically charges particles, QCD dictates the interactions of *color-charged* particles. Due to the
382 particular importance of QCD in this thesis, this topic will be explored in detail in section 1.2.

The fundamental Feynmann diagram for each of the three forces discussed here is depicted in Figure 1.2. The fourth fundamental force, gravity, is not currently explained by any known mechanism within the Standard Model.

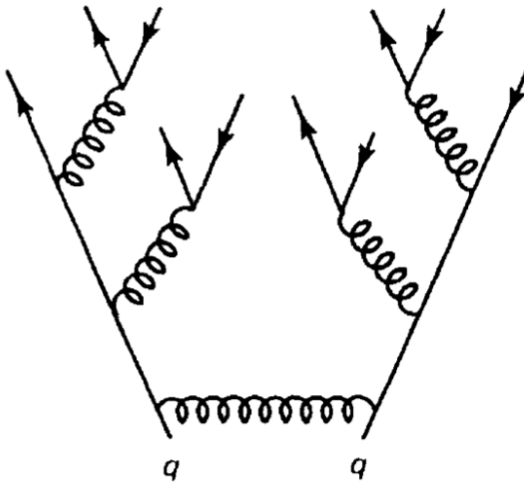


Figure 1.3: An example Feynmann diagram of jet production

386 1.2 QCD and Jets

387 While there is only one type of electric charge, there are three types of color charge; red, green,
 388 and blue. In the process $q \rightarrow q + g$, the color of the quark can change. In order to conserve color
 389 charge, gluons are bicolored, and always carry some positive color charge and some negative color
 390 charge.

391 Color charged particles can only exist in bound states which result in a neutral total color
 392 charge, a principle known as confinement. This requires that quarks and gluons exist in group
 393 states known as hadrons; either mesons in the case of two quarks or baryons in the case of three
 394 quarks. When a quark is separated from a hadron, confinement dictates that other colored objects
 395 are produced around the quark to obey confinement. An example of this process is shown in
 396 Figure 1.3. This ensemble of objects, generally a mixture of quarks and gluons, is termed a *jet*.
 397 Jets are among the most common phenomenon observed by detectors at hadron colliders, and their
 398 complex structure makes them a key focus of many physics analyses.

399 **1.3 Symmetries**

400 The Standard Model is a renormalizable quantum field theory that obeys the local symmetry

401 G_{SM} :

$$G_{SM} = SU(3)_C \times SU(2)_L \times U(1)_Y. \quad (1.1)$$

402 The $SU(3)_C$ symmetry component represents the non-Abelian gauge group of QCD. There
403 are 8 generators for the $SU_C(3)$ group which correspond to 8 types of gluon, each representing a
404 different superposition of color charge [3]. The $SU(2)_L \times U(1)_Y$ symmetry group represents the
405 electroweak sector of the Standard Model, which can be spontaneously broken into the electromag-
406 netic and weak sectors. There are 4 generators for this group, which correspond to four massless
407 gauge bosons W^1 , W^2 , W^3 , and B . From these massless gauge bosons are formed the massive
408 mediators of the weak force, the W^- , W^+ and Z^0 bosons, and the massless electromagnetic force
409 carrier, the photon γ . Spontaneous symmetry breaking and the process by which gauge bosons
410 acquire mass will be addressed in section 1.3.1.

411 Noether's theorem [4] stipulates that any continuous symmetry is associated with a conserved
412 quantity. In the Standard Model, this means that the $SU(3)_C$ symmetry gives rise to conservation of
413 color charge. The $SU(2)_L \times U(1)_Y$ symmetry gives rise to conservation of electromagnetic charge.
414 Conservation of spin results from the Poincaré symmetry described by the theory of special rela-
415 tivity, which combined with Noether's theorem gives us the conservation of energy, momentum,
416 and angular momentum.

417 The SM Lagrangian is invariant under CPT symmetry, or charge, parity, and time reversal.
418 Charge conjugation (C) transform a particle into its corresponding antiparticle by reversing the
419 charge and other quantum numbers. Parity conjugation (P) reverses spatial coordinates, which
420 transforms left-handed particles into right-handed particles and vice-versa. Time reversal (T) is
421 the theoretical process of reversing time. The L subscript in the $SU(2)_L$ group indicates that this
422 symmetry only applies to left-handed fermions. As a result, the $W^{1,2,3}$ gauge bosons of $SU(2)_L$

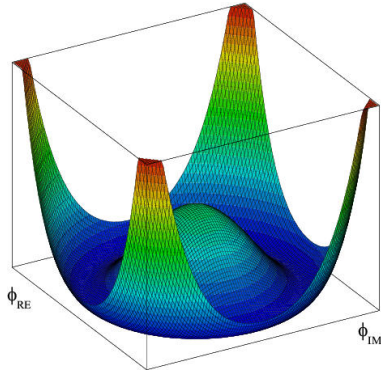


Figure 1.4: An illustration of the “hat shaped” potential of the Higgs field, resulting in a non-zero vacuum expectation value.

only interact with left handed particles, a process which maximally violates P-symmetry in the weak force. A small amount of the CP symmetry violation is also observed in the Standard Model, through the decays of strange flavored mesons [5] and b -mesons [6]. The CPT theorem posits that the violation of CP symmetry implies that T-symmetry must also be violated, so that CPT is a preserved symmetry.

1.3.1 Spontaneous Symmetry Breaking and The Higgs Mechanism

Spontaneous symmetry breaking is the process by which a Lagrangian obeys a symmetry at high energies, but exhibits asymmetric behavior at lower energies. The electroweak symmetry group is spontaneously broken as $SU(2)_L \times U(1)_Y \rightarrow U(1)_{EM}$. The quantity conserved by the $SU(2)_L$ symmetry is weak isospin $T_{1,2,3}$, while the quantity conserved by $U(1)_Y$ symmetry is weak hypercharge Y . Below very high energies, the presence of the Higgs field causes the electroweak symmetry to break. The Higgs field is a scalar field which forms a complex doublet of the $SU(2)$ symmetry group, with four degrees of freedom. The shape of the Higgs field potential, shown in Figure 1.4, results in a ground state with a non-zero vacuum expectation value; thus the Higgs field takes a non-zero value throughout all space, which breaks the symmetry of the weak isospin $SU(2)$ group.

The interaction with the Higgs field mixes the four massless gauge bosons $W^{1,2,3}$ and B . Three Higgs field degrees of freedom mix with the massless gauge bosons, resulting in three massive

441 gauge bosons W^- , W^+ and Z^0 . The massless photon γ is created from the components of the
442 massless gauge bosons which do not interact with the Higgs field. The scalar Higgs boson arises
443 from the one unmixed degree of freedom the Higgs field. Spontaneous symmetry breaking also
444 violates the conservation of weak isospin and weak hypercharge, leaving only electromagnetic
445 charge ($Q = T_3 + \frac{1}{2}Y$) as a conserved quantity associated with the $U(1)_{EM}$ symmetry.

446 **1.4 Experimental Validation of the Standard Model**

447 The theoretical framework of the Standard Model coalesced into a unified theory in the mid-
448 20th century. A cascade of discoveries providing empirical evidence for the model followed
449 closely. In the 1960s, three quarks (up, down and strange) and four leptons (electron, muon,
450 and their associated neutrinos) were the known particulate building blocks of matter and the Stan-
451 dard Model. The discovery of the charm quark in 1974, through the observation of the J/ψ meson
452 [7][8], confirmed the existence of a fourth quark flavor. The discovery of the τ in 1975 [9] provided
453 the first evidence of a 3rd generation of matter. This was quickly followed by the observation of
454 the Υ meson in 1977 [10], which provided evidence for the existence of a fifth quark, the b quark
455 (bottom, or beauty). The existence of a 3rd generation of fermion also explained the observation
456 of CP violation in the weak force, as it allowed for the addition of a complex phase in the CKM
457 matrix (a unitary matrix which describes flavor mixing in the weak interaction). The top quark
458 (t) and tau neutrino (ν_τ) were predicted at this point as the final building blocks of three complete
459 generations of fermions, and they were discovered by experimental observation around the turn of
460 the 21st century [11] [12] [13].

461 The W and Z bosons were predicted by the Standard Model, but to observe them required the
462 construction of a particle accelerator powerful enough to produce them. They were finally observed
463 at CERN in 1983 by the UA1 and UA2 experiments [14] [15] at the newly constructed Super Proton
464 Synchrotron (SPS). Their masses were observed to be compatible with the masses predicted by the
465 Standard Model nearly a decade earlier. The final missing piece then was confirming the existence
466 of the Higgs, which again required the construction of a newer and more powerful collider. CERN

467 achieved this with the construction of the Large Hadron Collider (LHC), and in 2012 the ATLAS
468 and CMS experiments announced the discovery of the Higgs particle [16] [17].

469 **1.5 Limitations of the Standard Model**

470 While the Standard Model has enjoyed decades of experimental results which confirm its pre-
471 dictions, there are several glaring shortcomings. The observed phenomenon for which the Standard
472 Model provides no explanation are summarized below.

- 473 • Gravity - the Standard Model does not account for the fourth fundamental force of gravity.
- 474 • Dark Matter - there is no viable candidate to explain the existence of dark matter, a non-
475 interacting form of matter which must exist to account for gravitational observations which
476 cannot be explained by general relativity, such as the motion of galaxies, gravitational lens-
477 ing, and the structure of the universe [18].
- 478 • Matter-Antimatter asymmetry - the level of CP violation in the Standard Model isn't suf-
479 ficient to explain the large discrepancy between the amount of matter and the amount of
480 antimatter in the universe today, and the origins of this imbalance are not understood.
- 481 • Neutrino masses - the Standard Model assumes that neutrinos are massless and provides
482 no mechanism for them to acquire mass. However, observations of neutrino oscillations
483 indicates they posses some small non-zero mass [19].

484 In addition to these unexplained natural phenomenon, there are several questions about the
485 *naturalness* of the Standard Model. The principle of naturalness states that dimensionless ratios
486 between physical constants should be of order 1, and that nature should not be arbitrarily fine-
487 tuned. While this is largely an aesthetic argument, it points to many aspects of the Standard Model
488 for which there exists no natural explanation.

- 489 • Strong CP - while CP symmetry is violated in the weak force, observations indicate that it
490 is preserved by the strong force [20]. The Standard Model predicts that CP violation in the

491 strong force is possible. There is no principle which motivates this incongruity between the
492 weak force and strong force.

- 493 • Hierarchy Problem - The wide range of masses for elementary particles and the wide range of
494 scales at which the four fundamental forces operate is not motivated by the SM. Specifically,
495 it is not understood why the Higgs mass is observed to be well below the Plank scale λ ,
496 which is the energy level at which the effects of quantum gravity become significant. QFT
497 indicates that the Higgs mass is determined by contributions from all energy scales including
498 λ , meaning that its observed mass is inexplicably small.

499 The limitations of the Standard Model provide a road map for theoretical and experimental
500 particle physicists, who seek to develop new theories which account for these observations, and
501 then to find evidence which might support these *Beyond the Standard Model* (BSM) theories. The
502 next chapter will introduce the BSM theories which motivate the physics search presented in this
503 thesis.

Chapter 2: Physics Beyond the Standard Model

506 In light of the various phenomenon unexplained by the Standard Model, physicists have pro-
 507 posed various extensions to the Standard Model, collectively termed *Beyond the Standard Model*
 508 (BSM) theories. A particular focus of the physics programs at the Large Hadron Collider (LHC)
 509 are BSM models which suggest dark matter candidate particles. If these particles couple to Stan-
 510 dard Model, they could be produced and observed at the LHC. This chapter will explore Hidden
 511 Valley models, and in particular the potential for Hidden Valley models to produce *semi-visible*
 512 *jets*. This will set the theoretical foundations for the experimental search presented in the later
 513 chapters of this thesis. The mechanisms of dark QCD that arise from these models and allow for
 514 the production of semi-visible jets will also be discussed.

515 **2.1 Hidden Valley Models**

516 Hidden Valley (HV) models are a category of BSM models that allow for dark matter (DM)
 517 production at the LHC. They extend the Standard Model with an additional non-Abelian gauge
 518 group [21]. This introduces the possibility of a complex dark sector, which mirrors the complexities
 519 of Standard Model QCD, and introduces the possibility of dark quarks and gluons. The term
 520 “hidden valley” refers to the idea that the DM is hidden from the SM by a high-energy barrier, as
 521 illustrated in Figure 2.1. The dark sector is assumed to communicate with the Standard Model via
 522 a “portal”, or “messenger particle”, that can interact with both Standard Model and HV forces. For
 523 the s-channel scenario, the portal is considered to be a new massive mediator particle Z' .

524 The portal particle allows for the production of dark sector particles at hadron colliders. If
 525 dark quarks are produced via the decay $Z' \rightarrow q_D q_D$ they can hadronize and form dark jets. The
 526 properties of the dark jets are determined by the dynamics of the dark sector, which are explored in

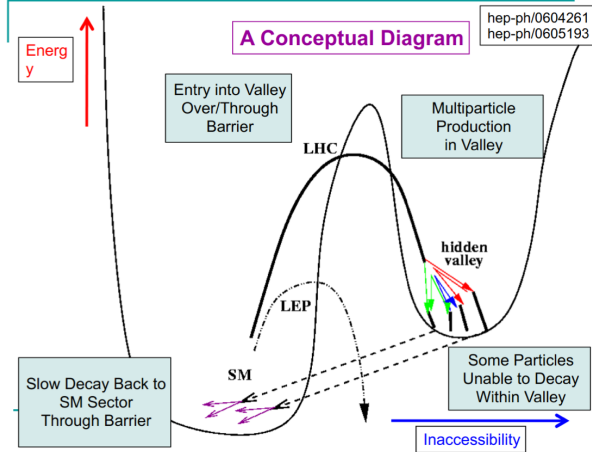


Figure 2.1: Illustration of the hidden valley potential.

527 the subsequent section. Depending on the details of the model, the jets formed by the dark hadrons
 528 can be categorized as fully dark, semi-visible, leptonic, emerging, or other [21].

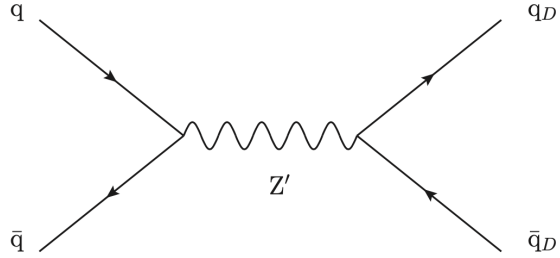


Figure 2.2: The massive mediator particle Z' of the s-channel realization of a HV model

529 2.2 Dark QCD

530 The theoretical underpinning of the semi-visible jet phenomenology is a dark sector with a
 531 gauge group $SU(N)_d$ leading to confinement at a scale Λ_d . For illustration, let's consider the
 532 case of an $SU(2)_d$ gauge theory, which gives rise to two dark fermionic generations $\chi_a = \chi_1, \chi_2$.
 533 Following the work of Ref [22] we can write the fundamental dark Lagrangian as:

$$\mathcal{L}_{dark} \supset -\frac{1}{2} \text{Tr} G_{\mu\nu}^d G^{d\mu\nu} - \bar{\chi}_a (i\cancel{D} - M_{d,a}) \chi_a \quad (2.1)$$

534 The first term allows for the dark gluons to self-interact, while the second term enables the dark
535 quarks to hadronize and acquire mass. The dark quarks are assumed to have a common mass M_d .

536 The coupling strength of the strongly interacting dark quarks is termed α_d . At the confinement
537 scale Λ_d , the dark quarks can form bound states. At the scale $M_d \approx \Lambda_d$ a QCD-like shower occurs.

538 The properties of the hadrons formed by the dark quarks are of particular importance to the
539 observed dark QCD dynamics. Dark-isospin number $U(1)_{1-2}$ and dark-baryon number $U(1)_{1+2}$
540 are accidental symmetries of the theory which determine the stability of the hadrons. In the case
541 of two dark flavors, six dark hadrons can be formed: four mesons ($\chi_1\bar{\chi}_1$, $\chi_2\bar{\chi}_2$, $\chi_1\bar{\chi}_2$, $\bar{\chi}_1\chi_2$) and
542 two baryons ($\bar{\chi}_1\bar{\chi}_2$, $\bar{\chi}_1\chi_2$). The mesons $\chi_1\bar{\chi}_2$ and $\bar{\chi}_1\chi_2$ are charged under dark-isospin and will be
543 stable if this symmetry is unbroken. The baryons would also be stable as they are charged under
544 the dark-baryon number. These four stable hadrons become dark matter candidates of the theory.

545 The $\chi_1\bar{\chi}_1$ and $\chi_2\bar{\chi}_2$ mesons are not charged under either symmetry and are thus expected to decay.
546 The unstable mesons can decay into stable dark mesons, or into an off-shell Z' . The off-shell Z'
547 will then decay into two DM quarks or two SM quarks, and its products will continue to shower
548 until the final state particles are stable.

549 The number of stable and unstable dark states varies substantially depending on the details
550 of the model. The model discussed above can be generalized from $SU(2)_d$ to $SU(N)_d$, with any
551 number of colors N_c or flavors N_f . This affects the ratio of possible stable to unstable mesons,
552 which can directly impact the amount of missing energy. The fraction of missing energy is a
553 variable in many dark QCD models, and is especially important in the case of semi-visible jets.

554 **2.3 Semi-visible Jets**

555 A “semi-visible jet” occurs when the heavy Z' messenger particle decays into dark quarks,
556 which then hadronize in a QCD-like shower. If some of the dark hadrons are stable while others
557 decay to SM quarks via the off-shell Z' , a collimated mixture of visible and dark matter is formed
558 – this is termed a semi-visible jet. If the Z' messenger particle is produced at rest, the two jets will
559 be back-to-back in the transverse plane. If there is an imbalance in the amount of invisible particles

560 between the two jets, one of the jets will be observed to be aligned with missing transverse energy.

561 While there are a myriad of HV and dark QCD models, a handful of model parameters are most
562 important in determining the observable of these showers within a particle detector. The coupling
563 strength α_d is one of the most important, as it controls the fraction of dark hadrons emitted in the
564 shower and their average p_T . The mass of the dark quarks directly impacts the jet mass. If the
565 masses of the dark quark flavors are comparable, the ratio of stable to unstable dark hadrons will
566 be approximately 1:1. However, if there is a mass splitting, stable or unstable dark hadrons may
567 be favored, which impacts the amount of missing energy observed.

568 The ratio of stable to unstable dark hadrons in the shower is a critical variable for capturing the
569 behavior of dark showers. This value is termed R_{inv} :

$$R_{inv} = \frac{\# \text{ of stable hadrons}}{\# \text{ of hadrons}} \quad (2.2)$$

570 Events containing jets aligned with missing transverse momentum are generally considered to
571 be misreconstructed by other DM searches, and therefore discarded. This class of final states is
572 therefore largely uncovered by existing DM searches. The nature of the dark hadron shower is
573 determined by the following parameters: the Z' mass $m_{Z'}$, the Z' couplings to visible and dark
574 quarks g_q and g_{q_D} , the number of dark colors and flavors, the characteristic scale of the dark sector
575 confinement Λ_D , the mass scale of the dark hadrons m_D , and the average fraction of stable hadrons
576 in the decay R_{inv} . The coupling to SM quarks determines the Z' production cross section.

577

Part II

578

Experiment

Chapter 3: The Large Hadron Collider

581 The Large Hadron Collider (LHC) is a 26.7 km circular high-energy particle accelerator, span-
582 ning the Swiss-French border near the city of Geneva, Switzerland [23]. The LHC occupies the
583 tunnel constructed in 1989 for the Large Electron-Positron (LEP) Collider, and reaches a maxi-
584 mum depth of 170m below the surface. The LHC is operated by the European Organization for
585 Nuclear Research (CERN), the largest international scientific collaboration in the world.

586 The LHC accelerates protons and heavy ions, and collides them at four interaction points
587 around the ring, with a design center-of-mass energy per collision of $\sqrt{s} = 14$ TeV. Each interaction
588 point is home to one of four detector experiments, which study the products of the collisions. The
589 largest of these experiments is the ATLAS detector, a general purpose detector designed to study
590 the Standard Model and search for new physics that could be produced in LHC collisions [24].
591 The CMS detector is another general purpose detector, designed and operated independently of the
592 ATLAS detector, but intended to probe the same range of physics [25]. The ALICE experiment is
593 a dedicated heavy ion experiment, and the LHC-b experiment is a dedicated *b*-physics experiment
594 [26] [27].

595 This chapter will cover the multi-component accelerator complex powering the LHC, the state-
596 of-the-art magnets which steer the particle beams, measurements of the intensity and number of
597 collisions produced by the LHC, and finally an overview of LHC activities in the past, present, and
598 future.

599 **3.1 Accelerator Physics**

600 **3.1.1 The Journey of a Proton**

601 From 2010 - 2018, the protons which fed the LHC started as hydrogen gas. The electrons were
602 removed from the hydrogen atoms through the use of strong electric fields. The linear accelerator
603 LINAC2 then accelerated the protons to an energy of 50 MeV. Between 2018 and 2020, LINAC2
604 was replaced with LINAC4, which instead accelerates H^- ions, hydrogen atoms with two electrons.
605 LINAC4 is capable of accelerating the H^- ions to 160 MeV. Before injection to the next part of
606 the acceleration chain, both electrons are stripped from the H^- ions, leaving just protons. From
607 here the protons enter the Proton Synchrotron booster, where they are accelerated up to 1.4 GeV of
608 energy. Subsequently they are sorted into bunches separated in time by 25 ns, where each bunch
609 contains approximately 10^{11} protons. Next the bunches pass through the Proton Synchrotron (PS)
610 and the Super Proton Synchrotron (SPS), where they reach energies of 25 GeV and 450 GeV
611 respectively. Finally they are injected into the LHC as two beams traveling in opposite direction.
612 The original design allowed each beam to be accelerated up to 7 TeV of energy. Due to limitations
613 in the performance of the superconducting LHC magnets, the highest energy actually achieved by
614 the LHC beams during Run 2 was 6.5 TeV, giving a collision center-of-mass energy of $\sqrt{s} = 13$
615 TeV [28]. Figure 3.1 shows the full LHC accelerator complex.

616 Acceleration in the LHC is performed by eight radio frequency (RF) cavities located around the
617 ring. Each RF cavity produces a 2 MV electric field oscillating at 40 MHz. The 40MHz oscillation
618 produces a point of stable equilibrium every 2.5 ns. These points of equilibrium are synchronized
619 with the occurrence of the proton bunches produced in the PS – a proton bunch occupies one out
620 of every ten points of stable equilibrium, such that the bunches maintain a 25 ns spacing [28].

621

The CERN accelerator complex Complexe des accélérateurs du CERN

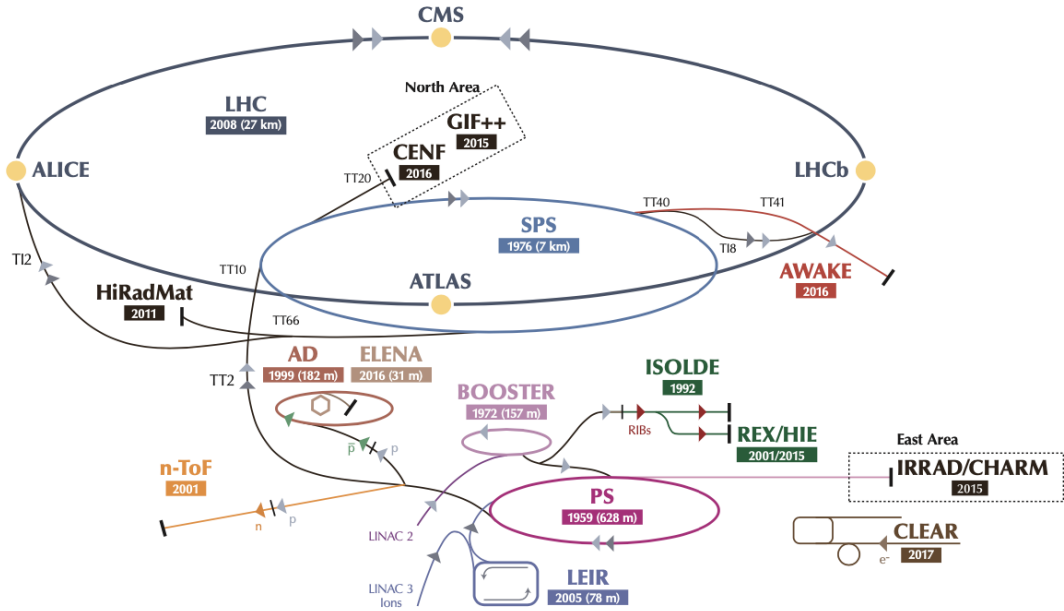


Figure 3.1: The LHC accelerator complex at CERN [29]

622 3.1.2 Magnets

623 In addition to the acceleration cavities, the LHC houses 9593 superconducting magnets which
 624 direct and focus the proton beam on its 27 kilometer journey. The magnets are comprised of super-
 625 conducting Niobium-Titanium coils cooled to 1.9K by superfluid helium. As the beams approach
 626 one of the four collision points around the ring, multipole magnets focus and squeeze the beam for
 627 optimal collisions [28].

628 The LHC is divided into sections, where each section contains an arc and a straight insertion. The arcs are composed of 1232 large dipole magnets which bend the beam
 629 to follow the roughly circular 27 km path. The main dipoles generate powerful 8.3 tesla magnetic
 630 fields to achieve this bend. Each dipole magnet is 15 meters long and weighs 35 tonnes. The
 631 dipoles work in conjunction with quadrupole magnets, which keep the particles in a focused beam,
 632 and smaller sextupole, octupole and decapole magnets which tune the magnetic field at the ends of
 633 the dipole magnets [30].

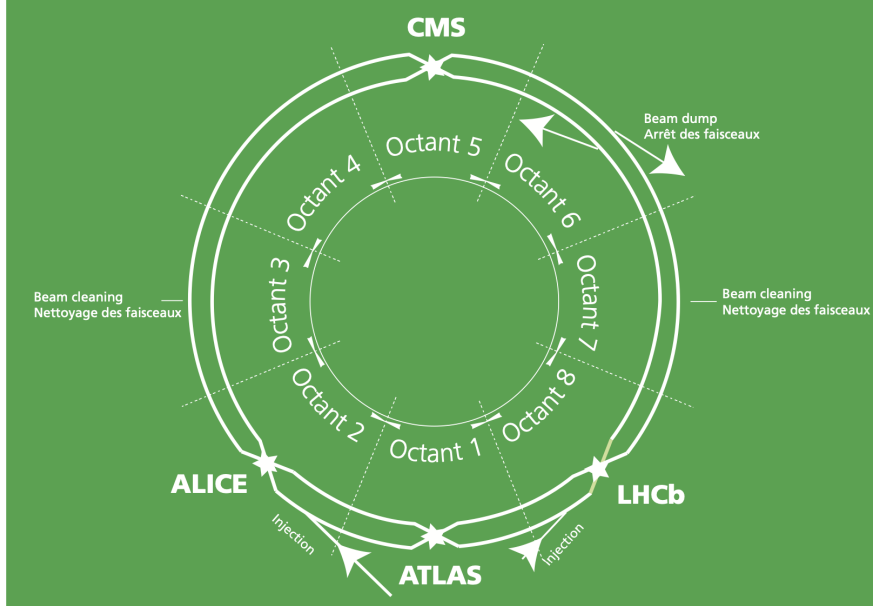


Figure 3.2: The octants of the LHC and location of various beam activities [28]. Stars indicate the locations of beam collisions, and the associated detectors recording the outcome of those collisions.

635 The straight insertion sections have different purposes depending on their location around the
 636 ring: beam collisions, beam injection, beam dumping, or beam cleaning. At the four collision
 637 points, insertion magnets squeeze the beam to ensure a highly focused collision. This is accom-
 638 plished with a triplet of quadrupole magnets, which tighten the beam from 0.2 millimeters to just
 639 16 micrometers in diameter. Insertion magnets also clean the beam, which prevents stray particles
 640 from hitting sensitive components throughout the LHC. When the LHC is ready to dispose of a
 641 beam of particles, beam dump magnets deflect the path of the beam into a straight line towards
 642 a block of concrete and graphite that stops the beam. A dilution magnet then reduces the beam
 643 intensity by a factor of 100,000 before the final stop [30]. Figure 3.2 shows the locations various
 644 beam activities.

645 3.2 Luminosity

646 Collisions at the LHC occur when the two beams of proton bunches cross at one of the four
 647 interaction points. The intensity of collisions is described by the instantaneous luminosity, the

648 formula for which is given in equation 3.1.

$$L = \frac{fN_1N_2}{4\pi\sigma_x\sigma_y} \quad (3.1)$$

649 Here f is the revolution frequency, N_1 and N_2 are the number of particle per bunch for each
650 beam, and σ_x , σ_y are the horizontal and vertical beam widths.

651 The instantaneous luminosity gives the number of the collisions that could be produced at the
652 interaction point per unit of cross-sectional area per unit of time, generally expressed in $\text{cm}^{-2}\text{s}^{-1}$.
653 The integrated luminosity is obtained by integrating the instantaneous luminosity over a given
654 block of time, and measures the total number of collisions which have occurred during that op-
655 eration period. The total integrated luminosity is directly correlated with the size of the datasets
656 collected by the LHC experiments. Total integrated luminosity for Run 2 is illustrated in Figure
657 3.3.

658 High levels of instantaneous luminosity result in multiple pp collisions per bunch crossing,
659 which leads to an effect known as *pileup*. Pileup poses a challenge for detector physics, as recon-
660 structing the products of multiple simultaneous events is far more challenging than reconstructing
661 a single event with no pileup. Pileup conditions vary from year-to-year and run-to-run of LHC op-
662 eration, and the impact of these conditions are taken into account when analyzing the data, as will
663 be discussed further in Chapter 5. Measurement of pileup conditions during Run 2 are illustrated
664 in Figure 3.3.

665 The design peak luminosity of the LHC is $1.0 \times 10^{34} \text{ cm}^{-2}\text{s}^{-1}$. During Run 1 of the LHC the
666 peak instantaneous luminosity was $0.8 \times 10^{34} \text{ cm}^{-2}\text{s}^{-1}$. Over the course of Run 1 the LHC collected
667 a total integrated luminosity of 5.46 fb^{-1} at $\sqrt{s} = 7 \text{ TeV}$, and 22.8 fb^{-1} at $\sqrt{s} = 8 \text{ TeV}$. Following the
668 first long shutdown and upgrade phase of operations, the LHC achieved a center of mass energy
669 $\sqrt{s} = 13 \text{ TeV}$ at the beginning of Run 2 in 2015. The LHC was also able to deliver 2.0×10^{34}
670 $\text{cm}^{-2}\text{s}^{-1}$ peak instantaneous luminosity, double the design value. During LHC Run 2, from 2015-
671 2018, the LHC delivered 156 fb^{-1} of integrated luminosity for proton-proton collisions. Run 3 of

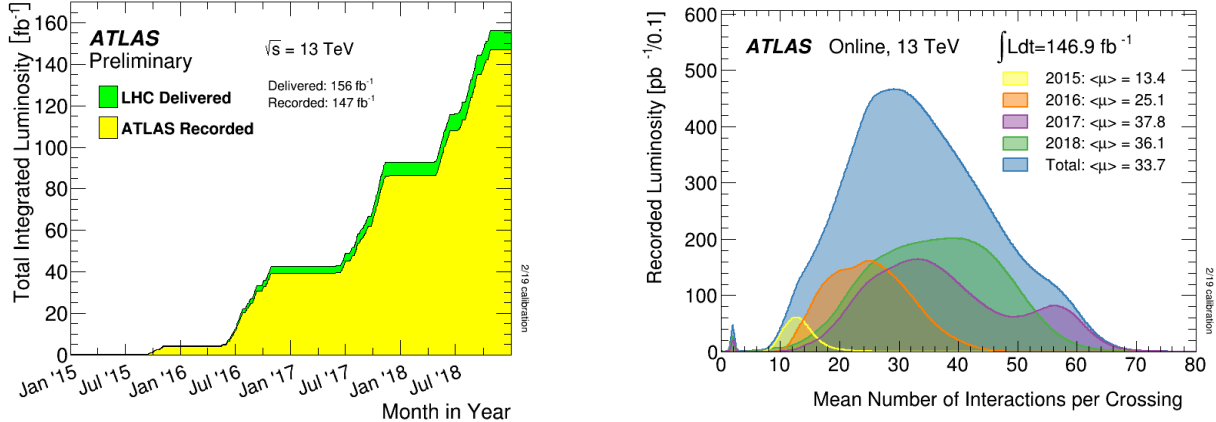


Figure 3.3: (Left) Total integrated luminosity over the course of Run 2. (Right) Average number of pp interactions per bunch crossing in Run 2. Each curve is weighted by the integrated luminosity for the year.

the LHC began in 2022, and is expected to deliver 250 fb^{-1} of integrated luminosity to the ATLAS and CMS experiments by 2026 [31].

The goal of LHC physic analyses is to find and study rare events produced by interesting physics processes. The cross section σ of a given process indicates the probability of that process occurring given the beam conditions of the LHC. Multiplying the cross section by the integrated luminosity of a dataset gives the expected number of events for that process within the dataset.

$$N_{\text{events}} = \int \sigma L(t) dt = \mathcal{L} \times \sigma \quad (3.2)$$

The cross section for most processes of interest, especially BSM processes, is several orders of magnitude below the total cross section for the LHC. Therefore maximizing the number of events produced in collisions is crucial to increase the likelihood of producing events from processes of interest. For this reason, maximizing instantaneous luminosity is a key factor in accelerator design and operation, while mitigating the resulting pileup effects is a key component in detector design and operation.

684 **3.3 LHC Timeline**

685 The first proton-proton collisions at the LHC were achieved in 2010 with a center-of-mass
686 energy of $\sqrt{s} = 7$ TeV. Run 1 of the LHC took place between 2010 and early 2013, during which
687 time the center-of-mass collision energy increased from 7 TeV to 8 TeV. Figure 3.4 shows an
688 overview of LHC activities beginning in 2011, in the midst of Run 1. The data collected during
689 Run 1 led to the discovery of the Higgs Boston in 2012 [32].

690 Between 2013 and 2015 the LHC underwent the first Long Shutdown (LS1) during which
691 time maintenance and renovation was performed on the accelerator chain, including the repair and
692 consolidation of the high-current splices which connect the super-conducting LHC magnets. Run
693 2 of the LHC took place from 2015 to 2018 and achieved a center-of-mass energy of $\sqrt{s} = 13$ TeV.
694 Analysis of data collected in Run 2 is still on going, and is the subject of study in this thesis.

695 Between 2018 and 2022 the LHC underwent the second Long Shutdown (LS2), allowing for
696 further detector and accelerator maintenance and upgrades. Key improvements to the LHC in-
697 cluded the improvement of the insulation for over 1200 diode magnets, and the upgrade from
698 LINAC2 to LINAC4 mentioned in Section 3.1.1. Run 3 of the LHC began in 2022 and achieved a
699 center-of-mass energy of $\sqrt{s} = 13.6$ TeV.

700 Run 3 is scheduled to continue through 2026, at which point the LHC machine and detectors
701 will undergo upgrades for the *high luminosity* LHC (HL-LHC). The HL-LHC will increase the
702 instantaneous machine luminosity by a factor of 5 - 7.5 with respect to the nominal LHC design.
703 The bottom panel of Figure 3.4 shows an overview of the preparation work for the HL-LHC that
704 has been going on concurrently with Run 1, 2, and 3 of the LHC [33].



Figure 3.4: Timeline of LHC and HL-LHC activities [31]. Integrated luminosity estimates are approximate, and not reflective of the exact amount delivered to each experiment.

Chapter 4: The ATLAS Detector

707 The ATLAS detector (**A** Toroidal **L**H**C** Apparatu**S**) is one of two general purpose physics
 708 detectors designed to study the products of proton-proton collisions at the LHC. The detector is
 709 composed of a variety of specialized subsystems, designed to fully capture a wide array of physics
 710 processes. A diagram of the detector is shown in Figure 4.1. The apparatus is 25m high, 44m in
 711 length, and weighs over 7000 tons [34]. The LHC beam pipes direct proton beams to an interaction
 712 point at the center of ATLAS, and the cylindrical detector design captures a complete 360° view
 713 of the *event*¹, tracking all particles that result from the collision.

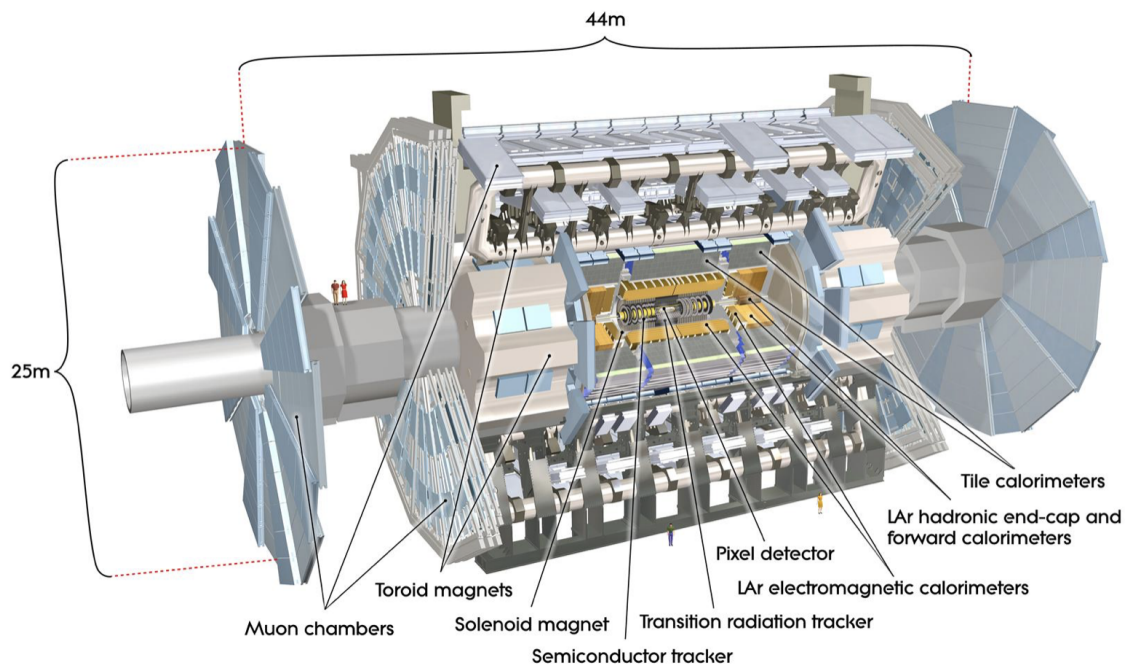


Figure 4.1: The ATLAS detector [34].

¹An ATLAS event is a snapshot of all the measurements associated to a given $p p$ collision

714 The main components of the ATLAS detector are the Inner Detector (ID) which provides high
 715 precision tracking of charged particles leaving the collision vertex, the calorimeter system which
 716 measures the energy of electromagnetic and hadronic objects, and the Muon Spectrometer (MS)
 717 which gives detailed information about muons that reach the outer radii of the detector. A summary
 718 of the resolution and angular coverage of each of these systems is presented in Table 4.1. Two
 719 magnet systems, a 2 T solenoid magnet surrounding the ID, and a 0.5-1.0 T toroid magnet system
 720 situated throughout the MS, produce magnetic fields which bend the trajectory of charged particles
 721 traversing the detector. In addition to the main detector components, dedicated forward detectors
 722 monitor beam conditions and instantaneous luminosity, and an online trigger system reduces the
 723 data rate to a manageable level for storage. Each of these components will be discussed in further
 724 detail in this chapter.

Detector component	Required resolution	η coverage	
		Measurement	Trigger
Tracking	$\sigma_{p_T}/p_T = 0.05\% p_T \oplus 1\%$	± 2.5	
EM calorimetry	$\sigma_E/E = 10\%/\sqrt{E} \oplus 0.7\%$	± 3.2	± 2.5
Hadronic calorimetry (jets)			
barrel and end-cap	$\sigma_E/E = 50\%/\sqrt{E} \oplus 3\%$	± 3.2	± 3.2
forward	$\sigma_E/E = 100\%/\sqrt{E} \oplus 10\%$	$3.1 < \eta < 4.9$	$3.1 < \eta < 4.9$
Muon spectrometer	$\sigma_{p_T}/p_T = 10\% \text{ at } p_T = 1 \text{ TeV}$	± 2.7	± 2.4

Table 4.1: General performance goals of the ATLAS detector [34].

725 4.1 Coordinate System and Geometry

726 The ATLAS detector employs a right hand cylindrical coordinate system. The z axis is aligned
 727 with the beam line, and the $x - y$ plane sits perpendicular to the beam line. The coordinate system
 728 origin is centered on the detector, such that the origin corresponds with the interaction point of the
 729 two colliding beams. The detector geometry is usually characterized by polar coordinates, where
 730 the azimuthal angle ϕ spans the $x - y$ plane. The polar angle θ represents the angle away from the
 731 beam line, or z axis. $\theta = 0$ aligns with the positive z axis, and $\phi = 0$ aligns with the positive x axis.

732 The polar coordinate θ is generally replaced by the Lorentz invariant quantity *rapidity* or y :

$$y = \frac{1}{2} \ln\left(\frac{E + p_z}{E - p_z}\right). \quad (4.1)$$

733 This substitution is advantageous because objects in the detector are traveling at highly rela-
734 tivistic speeds. The relativistic speed also means that the masses of the particles are generally small
735 compared to their total energy. In the limit of zero mass, the rapidity y reduces to the pseudorapid-
736 ity η , which can be calculated directly from the polar angle θ :

$$\eta = -\ln\left(\frac{\theta}{2}\right). \quad (4.2)$$

737 The distance between physics objects in the detector is generally expressed in terms of the solid
738 angle between them ΔR :

$$\Delta R = \sqrt{\Delta\phi^2 + \Delta\eta^2} \quad (4.3)$$

739 Figure 4.2a depicts the orientation of the coordinate system with respect to the ATLAS detector,
740 while Figure 4.2b illustrates the relationship between θ , η , and the beamline axis z . Direct or “head
741 on” proton-proton collisions are more likely to result in objects whose momentum is directed
742 along transverse plane (low $|\eta|$); glancing proton-proton collisions are more likely to result in
743 objects whose momentum is directed along the z -axis (high $|\eta|$). Due to the difference in the
744 nature of these collisions, as well as the cylindrical design of the ATLAS detector, the detector
745 is divided into regions of low and high $|\eta|$. Each subsystem has a “central” or “barrel” region
746 covering low $|\eta|$, while the “forward” or “end-cap” regions cover the area up to $|\eta| = 4.9$. Each of
747 the three main ATLAS subsystems will be discussed in the following sections.

748 **4.2 Inner Detector**

749 The Inner Detector (ID) is the ATLAS subsystem closest to the interaction point. The primary
750 purpose of the ID is to determine the charge, momentum, and trajectory of charged particles pass-

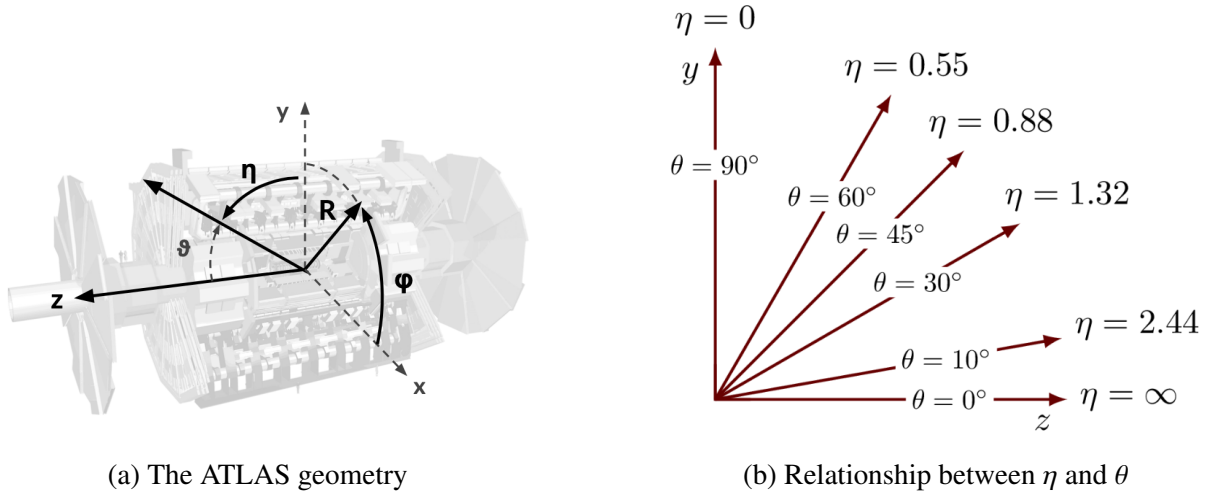


Figure 4.2: ATLAS coordinate system and geometry

751 ing through the detector. With this information the ID is also able to precisely determine interaction
 752 vertices.

753 The ID is composed of three sub-detectors; the Pixel Detector, the Semiconductor Tracker
 754 (SCT) and the Transition Radiation Tracker (TRT) [34]. Figure 4.3 shows the location of these
 755 three subsystems with respect to each other and the interaction point.

756 4.2.1 Pixel Detector

757 The pixel detector is the first detector encountered by particles produced in LHC collisions.
 758 The original pixel detector consists of 3 barrel layers of silicon pixels, positioned at 5 cm, 9 cm
 759 and 12 cm from the beamline. There are also 3 disks on each end-cap positioned 50 - 65 cm
 760 from the interaction point, providing full coverage for $|\eta| < 2.2$. Figure 4.4 illustrates the end-cap
 761 geometry for the ID. The layers are comprised of silicon pixels each measuring $50 \times 400 \mu\text{m}^2$,
 762 with 140 million pixels in total. The pixels are organized into modules, which each contain a set
 763 of radiation hard readout electronics chips. In 2014, the Insertable B-layer (IBL) was installed,
 764 creating a new innermost layer of the pixel detector sitting just 3.3 cm from the beamline. The
 765 pixels of the IBL measure $50 \mu\text{m}$ by $250 \mu\text{m}$, and cover a pseudo-rapidity range up to $|\eta| < 3$.
 766 The IBL upgrade enhances the pixel detector's ability to reconstruct secondary vertices associated

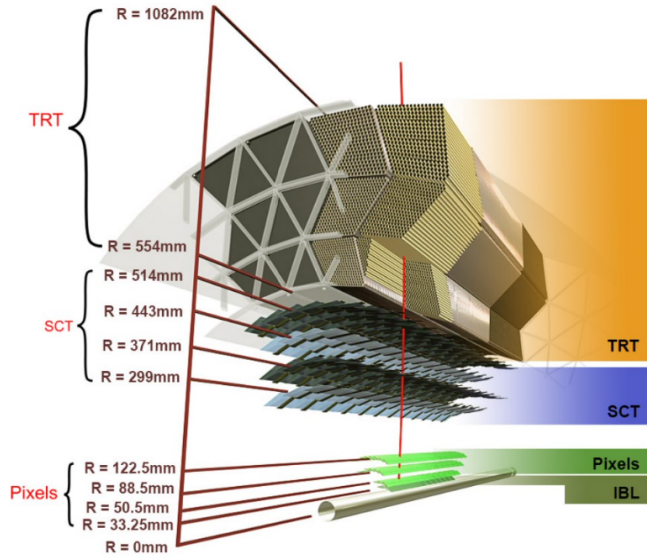


Figure 4.3: A 3D visualization of the structure of the ID in the barrel region [35]

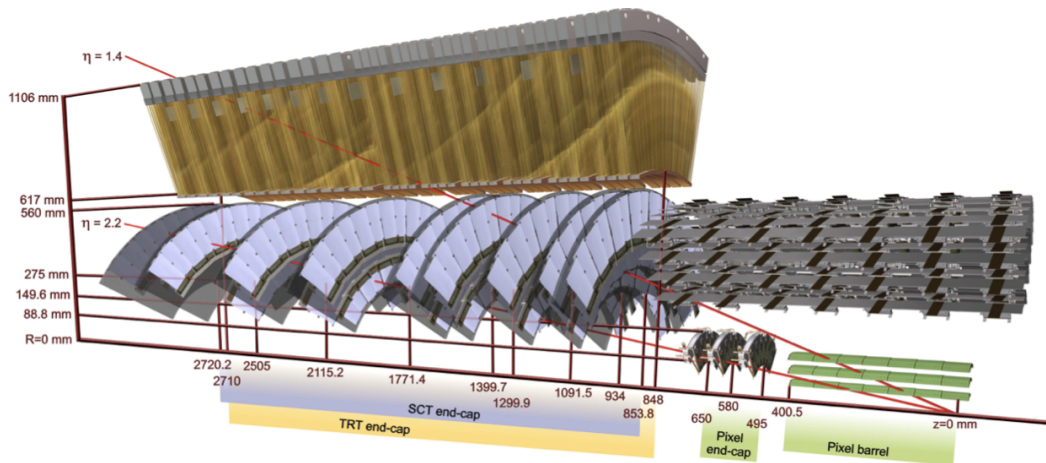


Figure 4.4: A 3D visualization of the structure of the ID end-caps [34]. The paths of two charged particles ($\eta = 1.4$ and 2.2) are illustrated.

767 with short-lived particles such as the b-quark. The improved vertex identification also helped
768 compensate for increasing pile-up in Run 2.

769 **4.2.2 Semiconductor Tracker**

770 The SCT provides at least 4 additional measurements of each charged particle. It employs the
771 same silicon technology as the Pixel Detector, but utilizes larger silicon strips which measure 80
772 μm by 12.4 cm. The SCT is composed of 4 barrel layers, located between 30 cm and 52 cm from
773 the beamline, and 9 end-cap layers on each side. The SCT can distinguish tracks that are separated
774 by at least 200 μm .

775 **4.2.3 Transition Radiation Tracker**

776 The TRT provides an additional 36 hits per particle track. The detector relies on gas filled
777 straw tubes, a technology which is intrinsically radiation hard. The straws which are each 4 mm in
778 diameter and up to 150 cm in length and filled with xenon gas. The detector is composed of about
779 50,000 barrel region straws and 640,000 end-cap straws, comprising 420,000 electronic readout
780 channels. Each channel provides a drift time measurement with a spatial resolution of 170 μm per
781 straw. As charged particles pass through the many layers of the detector, transition radiation is
782 emitted. The use of two different drift time thresholds allows the detector to distinguish between
783 tracking hits and transition radiation hits.

784 **4.3 Calorimeters**

785 The ATLAS calorimeter system is responsible for measuring the energy of electromagnetically
786 interacting and hadronically interacting particles passing through the detector. The calorimeters are
787 located just outside the central solenoid magnet, which encloses the inner detectors. The calorime-
788 ters also stop most known particles, which the exception of muons and neutrinos, preventing them
789 from traveling to the outermost layers of the detector. The ATLAS calorimetry system is composed
790 of two subsystems - the Liquid Argon (LAr) calorimeter for electromagnetic calorimetry and the

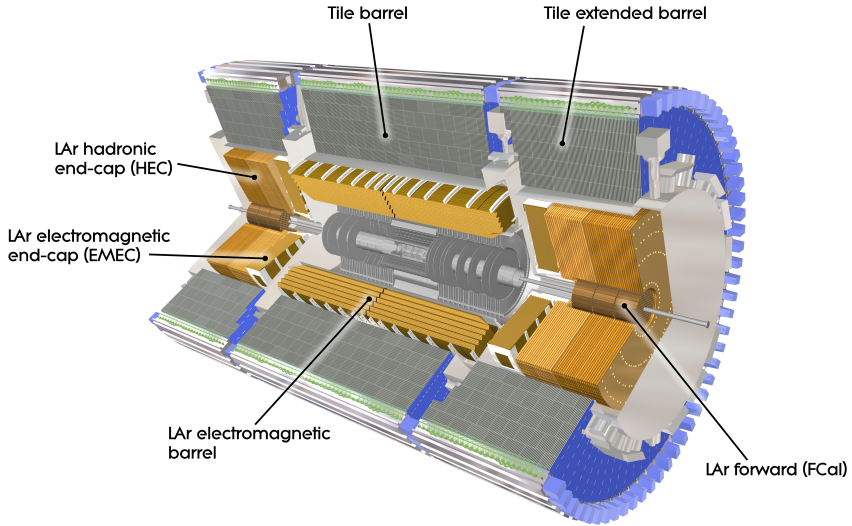


Figure 4.5: ATLAS calorimetry system [36]

791 Tile calorimeter for hadronic calorimetry. The full calorimetry system is shown in Figure 4.5.

792 4.3.1 Liquid Argon Calorimeter

793 The LAr calorimeter is a sampling calorimeter designed to trigger on and measure the ener-
794 gies of electromagnetic (EM) particles, as well as hadronic particles in the high $|\eta|$ regions [37].
795 It is divided in several regions, as shown in Figure 4.5. For the region $|\eta| < 1.4$, the electro-
796 magnetic barrel (EMB) is responsible for EM calorimetry, and provides high resolution energy,
797 timing, and position measurements for electrons and photons passing through the detector. The
798 electromagnetic end-cap (EMEC) provides additional EM calorimetry up to $|\eta| < 3.2$. In the
799 region $1.4 < |\eta| < 3.2$, the hadronic end-cap (HEC) provides hadronic calorimetry. For hadronic
800 calorimetry in the region $|\eta| < 1.4$, corresponding to a detector radii > 2.2 m, the less expensive
801 tile calorimeter (discussed in the next section) is used instead. A forward calorimeter (FCAL)
802 extends the hadronic calorimetry coverage up to $3.1 < |\eta| < 4.9$.

803 The LAr calorimeter is composed of liquid argon sandwiched between layers of absorber mate-
804 rial and electrodes. Liquid argon is advantageous as a calorimeter active medium due to its natural
805 abundance and low cost, chemical stability, radiation tolerance, and linear response over a large

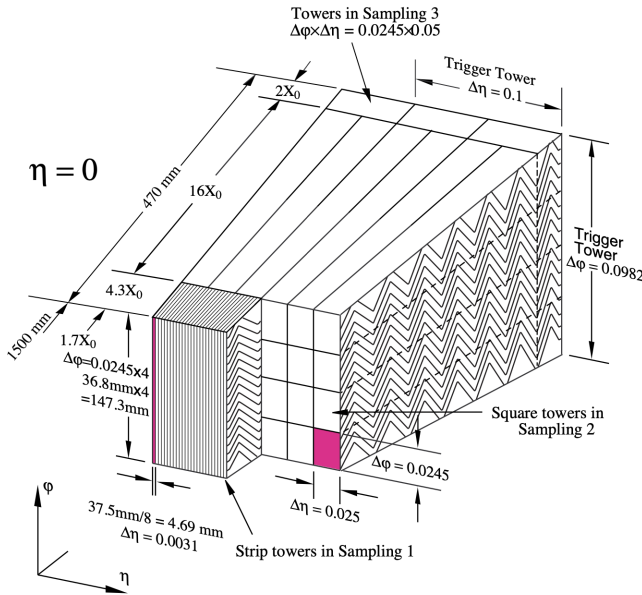


Figure 4.6: Diagram of a segment of the EMB, demonstrating the accordion plate arrangement [37]

806 energy range [38]. The calorimeter is cooled to 87k by three cryostats: one barrel cryostat encom-
 807 passing the EMB, and two end-cap cryostats. The barrel cryostat also encloses the solenoid which
 808 produces the 2T magnetic field for the inner detector. Front-end electronics are housed outside the
 809 cryostats and are used to process, temporarily store, and transfer the calorimeter signals.

810 Electromagnetic Calorimeter

811 For the electromagnetic calorimeters, the layers of electrodes and absorber materials are ar-
 812 ranged in an accordion shape, as illustrated in Figure 4.6. The accordion shape ensures that each
 813 half barrel is continuous in the azimuthal angle, which is a key feature for ensuring consistent high
 814 resolution measurements. Liquid argon permeates the space between the lead absorber plates, and
 815 a multilayer copper-polymide readout board runs through the center of the liquid argon filled gap.

816 The detection principle for the LAr calorimeter is the current created by electrons which are
 817 released when a charged particle ionizes the liquid argon. In the barrel region, the electrons are
 818 driven towards the center electrodes by a 2,000 V potential with a drift time of less than 450 ns

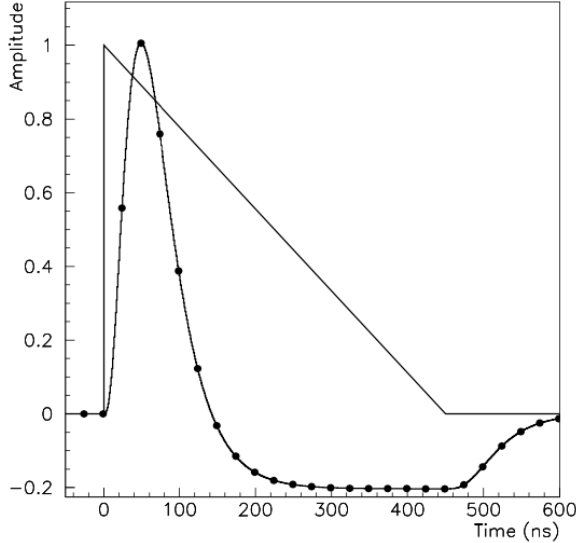


Figure 4.7: A LAr pulse as produced in the detector (triangle) and after shaping (curve) [37]

[39]. In the end-caps the voltage varies as a function of the radius in order to maintain a flat response [37]. The amount of current produced by the ionized electrons is proportional to the energy of the particle creating the signal. Figure 4.7 shows the shape of the signal produced in the LAr calorimeter, before and after it undergoes shaping during the readout process. The shaping of the pulse enforces a positive peak and a negative tail, which ensures that subsequent pulses can be separated with the precision required for the 25 ns LHC bunch spacing.

Hadronic End-cap Calorimeter

The HEC sits radially beyond the EMEC. The copper absorber plates in the HEC are oriented perpendicular to the beamline, with LAr as the active medium. Each end-cap is divided into two independent wheels; the inner wheel uses 25 mm copper plates, while the outer wheel uses 50 mm plates as a cost saving measure. In each wheel, the 8.5 mm plate gap is crossed by three parallel electrodes, creating an effective drift distance of 1.8 mm. This gap is illustrated in Figure 4.8. Each wheel is divided into 32 wedge-shaped modules, each containing their own set of readout electronics.

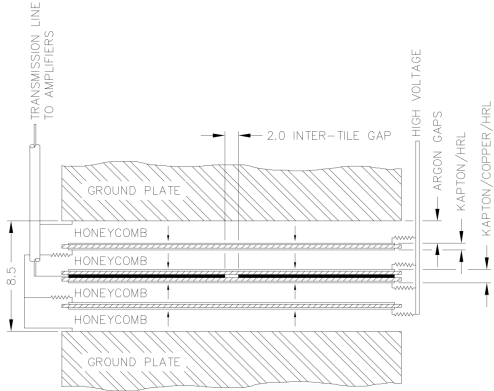


Figure 4.8: Readout gap structure in HEC [37]

833 Forward Calorimeter

834 The forward range ($3.1 < |\eta| < 4.9$) is covered by the FCal, which provides both EM and
 835 hadronic calorimetry. It is composed of three active cylindrical modules; one EM module with
 836 copper absorber plates, and two hadronic modules with tungsten absorber plates [37]. The plates
 837 are oriented perpendicular to the beamline, and LAr is used as the active material throughout. The
 838 electrodes of the FCal consist of tubes that run parallel to the beam line, arranged in a honeycomb
 839 pattern. The resulting LAr gaps are as small as $250 \mu\text{m}$, which enables the FCal to handle the high
 840 particle flux in the forward region.

841 4.3.2 Tile Calorimeter

842 The Tile Calorimeter (TileCal) provides hadronic calorimetry in the region $|\eta| < 1.7$, and sur-
 843 rounds the LAr calorimeter. It is responsible for measurements of jet energy and jet substructure,
 844 and also plays an important role in electron isolation and triggering (including muons) [40]. Tile-
 845 Cal is composed of 3 sections, as shown in Figure 4.5; a barrel calorimeter sits directly outside the
 846 LAr EMB and provides coverage up to $|\eta| < 1.0$. Two extended barrel sections sit outside the LAr
 847 end-caps and cover the region $0.8 < |\eta| < 1.7$.

848 TileCal is a sampling calorimeter composed of steel and plastic scintillator plates as illustrated
 849 in Figure 4.9. A total of 460,000 scintillators are read out by wavelength-shifting fibers. The

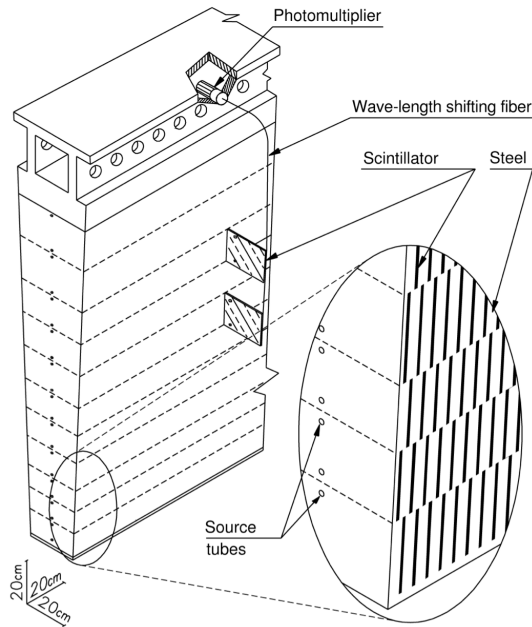


Figure 4.9: TileCal wedge module [40]

850 fibers are gathered to define cells and in turn read out by photomultiplier tubes, which amplify the
 851 scintillation light and convert it to an electrical signal. Each cell has an approximate granularity of
 852 $\Delta\eta \times \Delta\phi = 0.1 \times 0.1$. Each barrel is divided azimuthally into 64 independent modules, an example
 853 of which is show in Figure 4.9. The modules are each serviced by front-end electronic housed in a
 854 water-cooled drawer on the exterior of the module.

855 The detection principle of the TileCal is the production of light from hadronic particles inter-
 856 acting with the scintillating tiles. When a hadronic particle hits the steel plate, a shower of particles
 857 are produced. The interaction of the shower with the plastic scintillator produces photons, the num-
 858 ber and intensity of which are proportional to the original particle's energy.

859

860 4.4 Muon Spectrometer

861 Unlike electrons, photons, and hadrons, muons interact minimally with the ATLAS calorime-
 862 ters, and can pass through large amounts of detector material without stopping. The ATLAS Muon
 863 Spectrometer (MS) provides additional tracking information to improve the identification and mea-

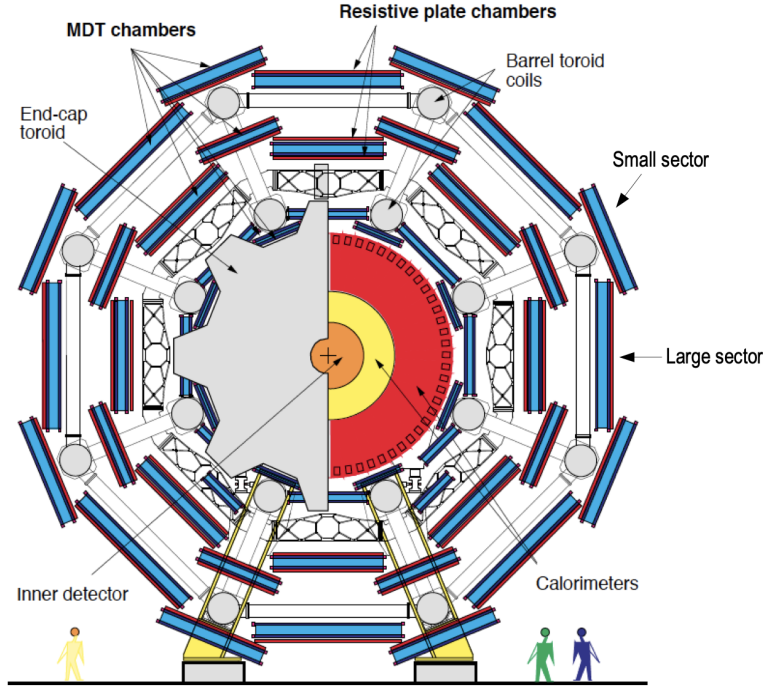


Figure 4.10: Cross section view of the muon spectrometer system [41]

surement of muons [41]. The MS comprises the outermost layers of the detector, and is interspersed with toroid magnets (discussed in Section 4.5), which provide a magnetic field of approximately 0.5 T. The magnetic field bends the trajectory of the muons as they pass through the detector, and the degree of the bend is directly correlated with the muon momentum. The path of the muon is primarily measured by hits in three layers of Monitored Drift Tube (MDT) precision chambers, which cover the range $|\eta| < 2.7$. The barrel layout of the MS is shown in Figure 4.10.

Muon triggering is provided by three layers of Resistive Plate Chambers (RPC) in the barrel ($|\eta| < 1.05$), and 3 - 4 layers of Thin Gap Chambers (TGC) in the end-caps ($1.05 < |\eta| < 2.4$). RPCs and TGCs also provide muon track measurements in the non-bending coordinate (ϕ). RPCs are constructed from two parallel resistive plates separated by a 2mm gap filled with a sensitive gas mixture. This provides a total of six independent measurements for each muon track, with a spatial resolution of ~ 1 cm and a time resolution of ~ 1 ns. Time measurements from the RPCs are primarily associated to hits in the MDT precision chambers to determine the bunch crossing. The time measurement is also used to reject cosmic muons, and to search for delayed signals.

878 TCGs provide triggering in the end-cap regions, and consist of parallel 30 μm wires suspended
879 in a sensitive gas mixture. TCGs provide high radiation tolerance and a fast response time, both
880 features that are necessary for handling the high flux of muons in the forward region.

881 Precision measurements of muon momentum and position are primarily achieved by MDTs.
882 The MDTs are constructed from 30 mm diameter tubes, permeated by a gas mixture of 93% Ar
883 and 7% CO₂ [42]. The average single-tube spatial resolution is 80 μm . Each chamber consists
884 of six drift tube layers, which together provide a muon track segment resolution of 35 μm . The
885 momentum of the muons can be calculated from the bend in the muon trajectory as they pass
886 through the 0.5T magnetic field provided by the toroids. For a $p_T = 1$ TeV track, the average
887 p_T resolution is 11%. In the inner most end-cap wheels, Cathode Strip Chambers (CSC) are
888 used instead of MDTs, covering the region $2.0 < |\eta| < 2.7$. CSCs are multi-wire proportional
889 chambers, with a cathode strip readout. The CSCs have a spatial resolution in the range of 50 μm ,
890 and a maximum drift time of about 30 ns, which makes them superior for handling the high flux of
891 particles in the forward region.

892 4.5 Magnet System

893 The ATLAS magnet system consists of four sets of superconducting magnets: a barrel solenoid,
894 a barrel toroid, and two end-cap toroids [43]. The solenoid magnet produces a 2T magnetic field
895 responsible for bending the trajectories of charged particles as they pass through the inner detector.
896 The three toroid magnets provide a field of 0.5 - 1 T and curve the path of muons passing through
897 the muon spectrometer.

898 The inner solenoid magnet is composed of over 9 km of niobium-titanium superconductor
899 wires, which are embedded into strengthened pure aluminum strips. The solenoid is just 4.5 cm
900 thick, which minimizes interactions between the magnet material and particles passing through the
901 detector. It is housed in the LAr cryostat, as described in section 4.3.1, which further reduces the
902 amount of non-detector material required to support the solenoid. The return yoke of the magnet
903 is provided by the iron absorber of the TileCal.

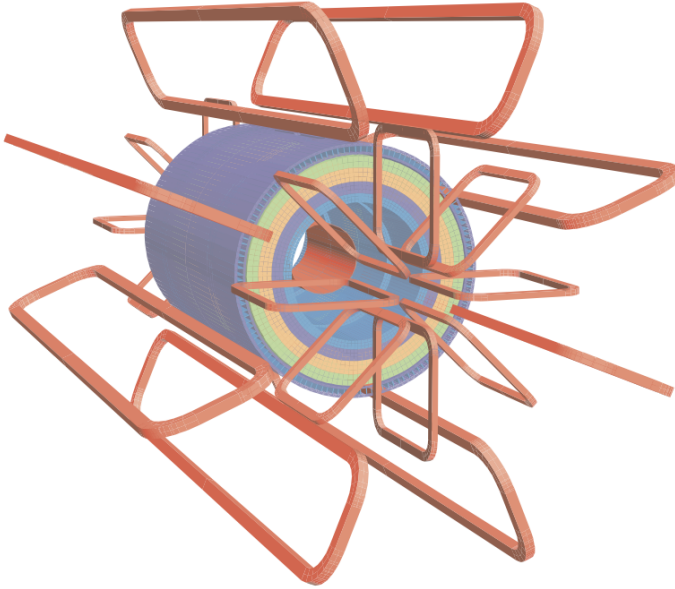


Figure 4.11: Layout of the barrel and end-cap toroid magnets [34]

904 The central ATLAS toroid magnet, providing the magnetic field for the barrel region of the
 905 MS, is the largest toroidal magnet ever constructed at 25.3 m in length [44]. The toroid is com-
 906 posed of eight individual coils, each housed in their own cryostat. The toroidal magnetic field is
 907 advantageous as the direction of the field is almost perpendicular to the path of the charged par-
 908 ticles. 56 km of aluminum stabilized niobium-titanium-copper superconductor wire compose the
 909 magnet. In each end-cap, eight smaller superconducting coils extend the toroidal magnetic field
 910 to particles leaving the detector in the forward direction [43]. Figure 4.11 shows the layout of the
 911 toroid magnets.

912 **4.6 Forward Detectors**

913 In addition to the inner detector, calorimeters, and muon spectrometer, three smaller detectors
 914 provide coverage in the very forward region. The innermost forward detector, at 17 m from the
 915 interaction point, is the **L**Uminosity measurement using **C**erenkov **I**ntegrating **D**etector (LUCID).
 916 LUCID's primary purpose is to measure the relative online-luminosity for the ATLAS detector,
 917 from inelastic $p - p$ scattering. The detector is composed of 20 aluminum Cerenkov tubes which

918 surround the beam pipe and face towards the interaction point.

919 The second forward detector is the Zero-Degree Calorimeter (ZDC), located 140 m from the
920 interaction point in both directions, at the point where the LHC beam-pipe divides into two separate
921 pipes. The ZDC's primary purpose is to detect forward neutrons from heavy ion collisions.

922 The third forward detector is the Absolute Luminosity For ATLAS (ALFA) system, located 240
923 m from the interaction point in both directions. ALFA determines luminosity by measuring elastic
924 scattering at small angles, from which luminosity can be calculated via the optical theorem. The
925 detector is built from scintillating fiber trackers. These are connected to the accelerator vacuum
926 via Roman pots, which allow the detector to come as close as 1mm to the beam without disrupting
927 the machine vacuum. The LUCID and ALFA detectors are crucial to determining the real-time
928 conditions of the beams and the total luminosity delivered to the ATLAS detector [34].

929 **4.7 Trigger and Data Acquisition**

930 The trigger and Data Acquisition systems (TDAQ) are responsible for selecting the most inter-
931 esting events to save for further downstream processing. Because of the high luminosities delivered
932 to the ATLAS detector, not all events recorded can be saved; the 40 MHz bunch crossing rate must
933 be reduced by 5 orders of magnitude to an event storage rate of \sim 1 kHz. The trigger system is
934 composed of three distinct levels: Level 1 (L1), Level 2 (L2) and the event filter [34]. Collectively
935 the L2 trigger and the event filter form the High Level Trigger (HLT).

936 The L1 trigger is implemented in the hardware of the ATLAS calorimeter and muon systems.
937 A block diagram of the L1 trigger is available in Figure 4.12. The primary modality of the L1 trig-
938 ger is to identify muons, electrons, photons, jets, and τ -leptons with high transverse momentum.
939 Particles with high transverse momentum are more likely to originate from direct, high energy
940 collisions, which are most likely to produce interesting physics processes. The L1 trigger also
941 identifies events with large missing transverse energy, which could be indicative of new physics.
942 The L1 muon trigger (L1Muon) relies on RPC and TGC trigger chambers in the barrel and end-
943 cap regions of the muon spectrometer. The L1 Calorimeter Trigger (L1Calo) uses reduced gran-

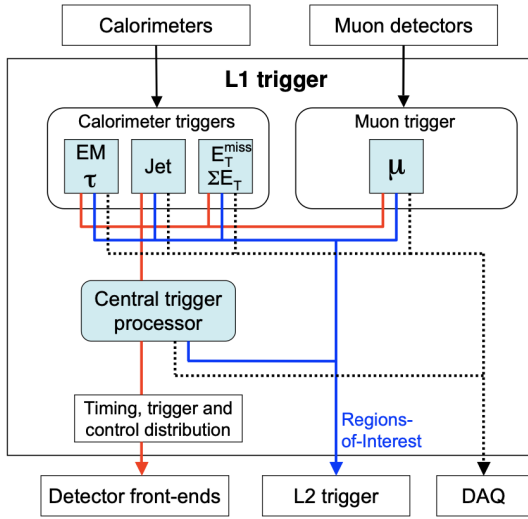


Figure 4.12: Block diagram of the L1 trigger process [34]. The overall L1 trigger decision is made by the CTP.

ularity information collected by all the calorimeter subsystems. Results from the L1Muon and L1Calo triggers are combined by the Central Trigger Processor (CTP), which implements a trigger ‘menu’, listing various combinations of trigger requirements. The maximum L1 acceptance rate is 100 kHz, and the L1 trigger decision must reach the front-end electronics within 2.5 μ s of its associated bunch-crossing.

The L1 trigger defines a Region-of-Interest (RoI) for each passing event. The ROI is represented by the $\eta\phi$ detector region where interesting features were identified by the L1 selection process. Information about the type of feature identified and the threshold which was exceeded to trigger the L1 response is also recorded. The ROI data is sent to the L2 trigger, which uses all of the available information within the ROI at full granularity and precision. The L2 trigger reduces the event rate from 100 kHz to 3.5 kHz, with an average processing time of 40 ms. The final stage of the HLT is the event filter, which reduces the event rate to 200 Hz (<1 kHz). The event filter uses an offline analysis process to select fully rebuilt events which will be saved for further analysis. A diagram of the full ATLAS TDAQ system is shown in Figure 4.13.

All levels of the ATLAS trigger system depend on specialized electronics. Each detector front-end system has a specialized Readout Driver (ROD) which collects information from several front-

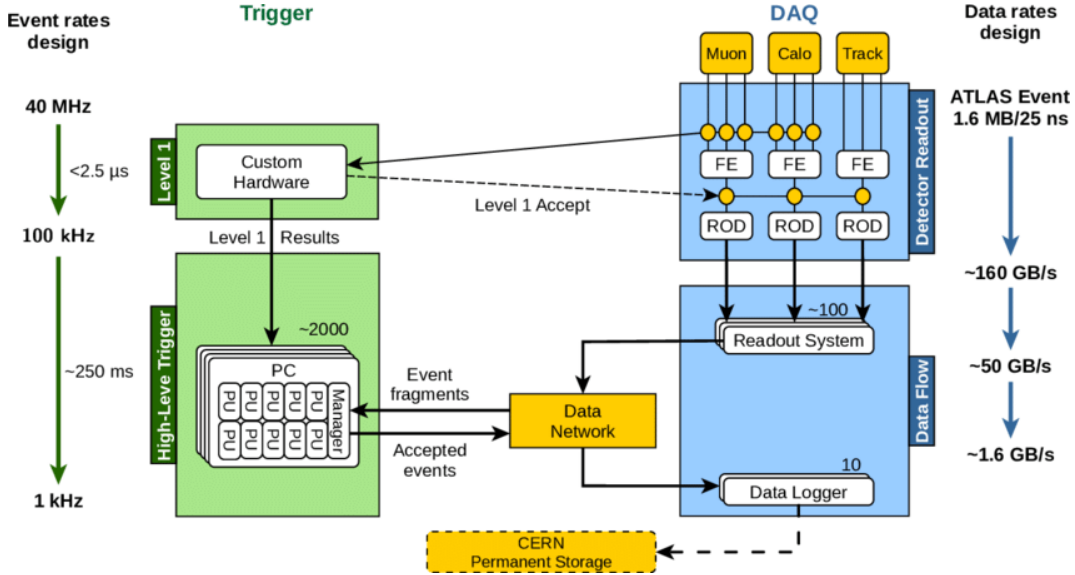


Figure 4.13: Block diagram of the trigger and data acquisition processes, including L1 and HLT processes [45].

960 end data streams at once. The ROD is composed of front-end analogue processing, a L1 buffer
 961 which retains the information long enough for the L1 trigger decision, and dedicated links which
 962 send the front-end L1 triggered data to Data Acquisition System (DAQ). Any digital signals are
 963 formatted as raw data before being transferred to the DAQ. The first stage of the DAQ temporarily
 964 stores the L1 data in local buffers. The ROI data is then requested by the L2 trigger, after which
 965 selected events are transferred to an event building system, before events passing the event filter
 966 are sent to the CERN computer center for permanent storage. The DAQ system not only allows
 967 for the readout of detector data, but is also responsible for the monitoring and configuration of
 968 the hardware and software components which make up the data readout system via the Detector
 969 Control System (DCS).

970 The DCS allows centralized control of all detector subsystems simultaneously. It continually
 971 monitors operational conditions, reports any abnormal behavior to the operator, and can perform
 972 both automatic and manual interventions. The DCS reports on real time detector conditions such
 973 as high or low voltage detector electronics, gas and cooling systems, magnetic field conditions,
 974 humidity and temperature. This information is continually monitored by experts in the ATLAS
 975 control room, so that action can be taken immediately to correct any issues that arise. The DCS also

- 976 handles communication between detector systems, and other systems such as the LHC accelerator,
977 the ATLAS magnets, and CERN technical services [34].

Chapter 5: Particle Reconstruction and Identification

With a design luminosity of $1.0 \times 10^{34} \text{ cm}^{-2}\text{s}^{-1}$, and a peak Run-2 instantaneous luminosity of $2.0 \times 10^{34} \text{ cm}^{-2}\text{s}^{-1}$, reconstructing and identifying the products of LHC pp collisions is one of the most complex tasks for each LHC experiment. The accurate reconstruction and identification of physics objects lays the ground work for all subsequent physics analyses, so it is also one of the most fundamentally important tasks performed by an experiment.

Reconstruction is the process of combining raw and uncalibrated hits across various subsystems into specific unique objects. Two particular subsystems, the Inner Detector (ID) tracker and the calorimeters play particularly important roles and will be discussed in detail. Analysis of the properties of the reconstructed objects identifies them as photon, electrons, muons, or jets. While photons, electrons, and muons are fundamental particles, jets represent a collimated shower of many hadronic particles, whose definition is more flexible. Jet reconstruction, clustering and track association are all of particular import to jet identification, and to the later content of this thesis. Finally, reconstruction also identifies missing transverse energy E_T^{miss} in events, which is a crucial variable for BSM physics searches. Figure 5.1 shows how the physics objects listed here interact with various systems in the ATLAS detector.

5.1 Inner Detector Tracks

As the inner most layer of the detector, the ID measures charged particles close to the interaction point. The various hits of these charged particles throughout the ID are used to reconstruct *tracks* which give the trajectories of charged particles [47]. Track reconstruction begins by clustering hits in the Pixel and SCT detectors, and combining clusters from different radial layers of these detectors. The multi-layer clusters form track *seeds*, which provide initial estimates of mea-

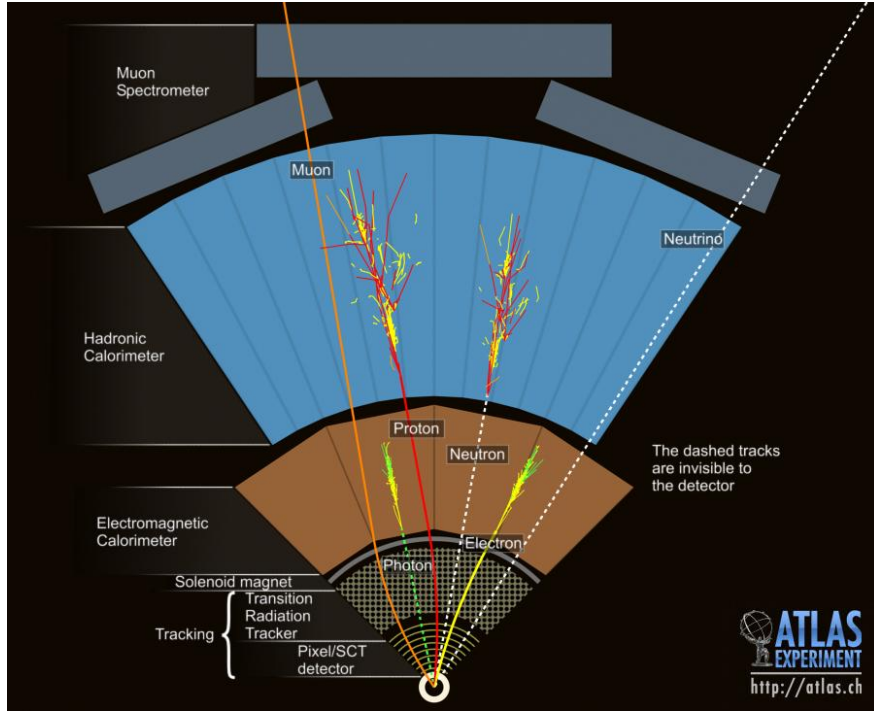


Figure 5.1: Graphic illustrating the various objects and high level features identified by ATLAS object reconstruction, and their interaction with different systems of the ATLAS detector [46]

1001 measurements belonging to an individual track. The requirement of three points allows for a rough
 1002 estimate of the track p_T to be made by calculating the curvature of the track and accounting of the
 1003 magnetic field in the ID.

1004 Track seeds are subject to a variety of quality requirements, such as having a minimum esti-
 1005 mated p_T and passing interaction region compatibility criterion. If these requirements are satisfied,
 1006 the track seeds are passed to the track finding and fitting algorithms. The interplay of these three
 1007 track reconstruction steps is illustrated in Figure 5.2.

1008 5.2 Photons and Electrons

1009 Photons and electrons shower in the LAr calorimeter, and are identified by the energy deposits
 1010 they leave there. Energy deposits in a collection of nearby cells are termed *clusters*, which become
 1011 the starting point for electron and photon reconstruction [48]. The clustering algorithm begins
 1012 when the energy deposit in a certain cell exceeds the noise threshold with a significance of 4σ .

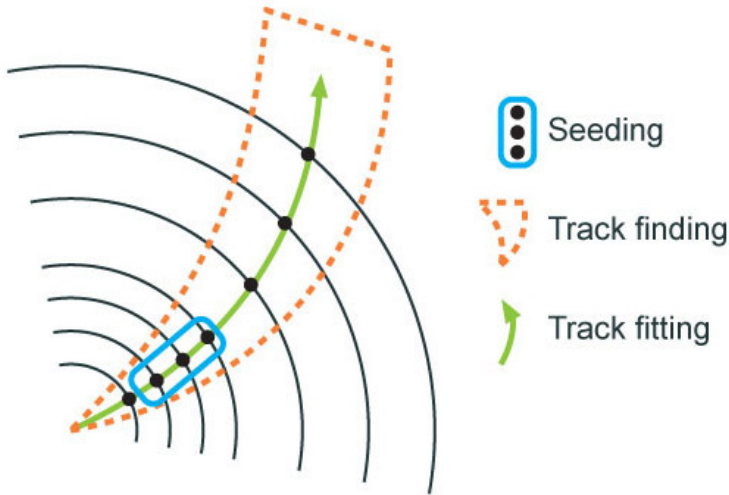


Figure 5.2: Track reconstruction seeding, finding and fitting illustration [47]

1013 The algorithm then collects neighboring cells which have an energy deposit exceeding the noise
 1014 threshold with a significance of 2σ , creating a topo-cluster. Next, these topo-clusters are matched
 1015 to ID tracks, created as described in Section 5.1. The location of the topo-cluster defines a region
 1016 of interest (ROI) in the ID, where additional modified track reconstruction algorithms are run in the
 1017 case that no associated tracks are found. Any ID tracks associated to the topo-cluster are retrofitted to
 1018 allow for additional energy loss due to bremsstrahlung. A converted photon track reconstruction
 1019 algorithm is run to check for tracks coming from secondary vertices consistent with converted
 1020 photons. The secondary vertices are constructed from two oppositely charged tracks consistent
 1021 with a massless particle, or from one track without any hits in the innermost layer of the ID.

1022 For electron identification, the EM cluster is required to match ID tracks that originate from
 1023 the primary vertex at the interaction point. For photon identification, the EM cluster can either be
 1024 matched to tracks coming from a secondary vertex (converted photon), or matched to no tracks
 1025 (unconverted photon). Figure 5.3 illustrates these three cases for EM object identification.

1026 *Superclusters* are built separately for photons and electrons, based on the combined topo-cluster
 1027 and ID track information. First, the EM topo-clusters are tested to see if they meet the minimum
 1028 requirements to become electron or photon seed clusters. For electrons, the cluster must have a
 1029 minimum E_T of 1 GeV, and must be matched to a track with at least 4 hits in the silicon tracking

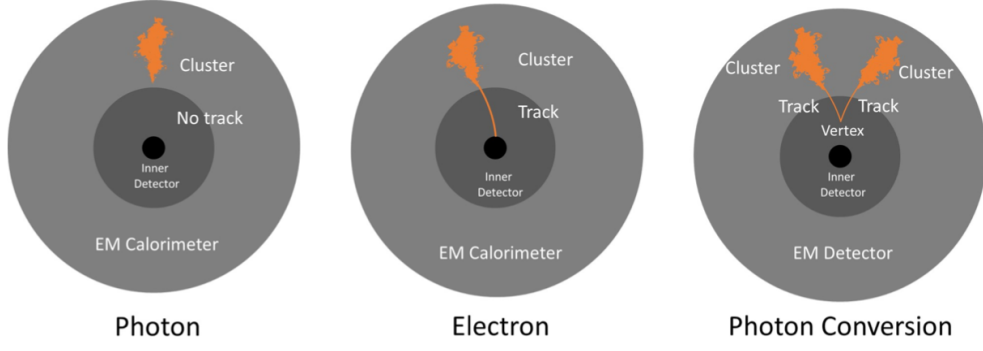


Figure 5.3: Three types of EM object candidates [49].

detectors. For photons, the cluster must have an E_T greater than 1.5 GeV. If the seed cluster requirements are met, the algorithm searches for satellite clusters, which can arise from bremsstrahlung radiation. If the satellite clusters pass the positional, energy and tracking requirements to be associated with the proto-cluster, they are combined into a supercluster.

Electron and photon objects are identified from the superclusters after energy calibration and position corrections are applied. Because photon and electron superclusters are built independently, some clusters can produce both a photon and an electron. In this case an ambiguity resolution procedure is applied to determine if the supercluster can be easily identified as only a photon (no tracks present) or only an electron (good tracks pointing to the primary vertex). In some cases, the identity of the cluster is still ambiguous, in which case both a photon and electron object are created for analysis and flagged as ambiguous. Energy, shower shape, and other analysis variables are calculated from the supercluster and saved with the electron or photon object.

5.3 Muons

Muons are identified through the tracks and energy deposits they leave in the ID, calorimeters, and Muon Spectrometer (MS). Muon identification begins in the Muon Drift Tube chambers by performing a straight line fit between the hits found in each layer, creating *segments*. Segments in the middle layers are then used as seeds for the track building algorithm, which searches for compatible combinations of segments based on their relative positions and angles [50]. A χ^2 fit is

1048 performed on each track candidate. Based on the χ^2 criteria, hits are removed or added such that
1049 the track contains as many hits as possible while satisfying the fit criteria.

1050 The MS track candidates are combined with track information from the ID and calorimeters
1051 according to various algorithms based on the information available from each subdetector. Four
1052 different types of muons arise from the various reconstruction algorithms:

- 1053 • Combined muon: a muon track identified through independent track reconstruction in the
1054 ID and MS, where the combined track is formed using a global refit that uses hit information
1055 from both detectors. Most muons are constructed through an outside-in procedure, in which
1056 a muon track candidate is identified in the MS and then an associated track is found in the ID.
1057 A complementary inside-out procedure is also implemented and identifies additional muons.
- 1058 • Segment-tagged muon: an ID track is identified as a muon if when extrapolated out to the
1059 MS (following the inside-out global fit procedure) it is matched to at least one local MS
1060 segment.
- 1061 • Calorimeter-tagged muon: an ID track is identified as a muon if it is matched to a calorimeter
1062 energy deposit that is compatible with a minimum-ionizing particle. This muon identifica-
1063 tion has the lowest purity, but it used in regions where the MS has only partial coverage due
1064 to cabling and service access routes.
- 1065 • Extrapolated muons: the muon is reconstruction only from the MS track and a requirement
1066 on compatibility with the primary interaction point. The muon track is required to cross at
1067 least two layers of the MS, and three layers in the forward region. These muons are mainly
1068 used to extend muon acceptance into the region $2.5 < |\eta| < 2.7$ where ID track information
1069 is not available.

1070 Figure 5.4 illustrates the four types of muon reconstruction. Overlap between reconstructed
1071 muons using ID tracks is resolved by giving preference to combined muons, then segment tagged
1072 muons, and finally calorimeter tagged muons. Overlap with extrapolated muons is resolved by
1073 giving preference to the muon with a better fit quality and higher number of tracks.

1074 All muon track candidates are required to pass a series of quality selections to be identified in
1075 the final muon collection. The primary qualities considered are the χ^2 goodness of fit for the global
1076 track, the difference in p_T measurement between the ID and MS tracks, and the ratio between the
1077 charge and momentum of the tracks. The quality requirements help reject hadrons, primarily from
1078 kaon and pion decays. Muons candidates consistent with cosmic rays are also rejected.

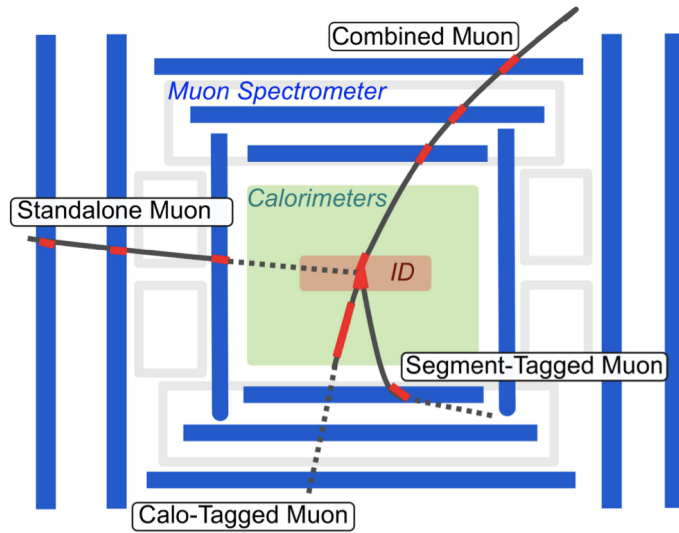


Figure 5.4: Four types of muon track candidates [51].

1079 5.4 Jets

1080 The protons accelerated in the LHC are composed of quarks and gluons, and thus their colli-
1081 sions often result in the release of energetic quarks and gluons, collectively termed *partons*. The
1082 energetic partons can radiate additional gluons, and these gluons can pair produce quarks in a pro-
1083 cess called *fragmentation*. Fragmentation continues until the energy drops sufficiently that color
1084 conservation plays a dominant role. At that point, additional quarks and gluons are produced from
1085 vacuum to create neutral color states for the fragmented collection of partons. This process is
1086 known as *hadronization* [52]. The hadronized partons compose a collimated stream of particles,
1087 known as a *jet*, which is then observed in the detector. The full process that produces jets is known
1088 as a *parton shower*, and is illustrated in Figure 5.5.

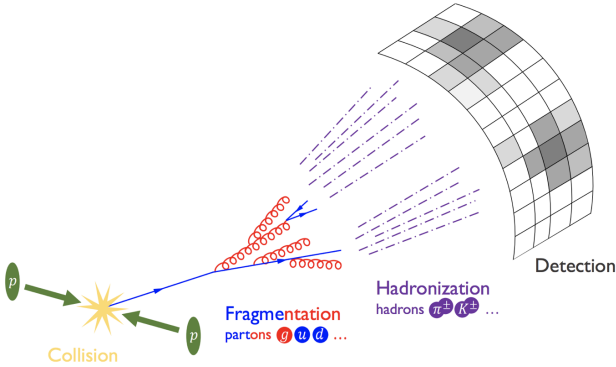


Figure 5.5: The fragmentation and hadronization processes undergone by a quark produced in a proton-proton collision [53].

1089 Jets are identified by the energy deposits they leave in the calorimeter, which are then matched
 1090 to the tracks they leave in the ID. Jet reconstruction generally begins in the calorimeters, with the
 1091 identification of *topo-clusters*. Then jet reconstruction algorithms combine calorimeter informa-
 1092 tion with tracking information. The anti- k_t algorithm [54] as provided by the FastJet library [55] is
 1093 generally used by the ATLAS experiment, with varying reconstruction radius settings. There are a
 1094 variety of jet collections depending on the exact usage of calorimeter and tracking information in
 1095 the reconstruction. Some common collections include particle flow jets (PFlow), track calo-cluster
 1096 jets (TCC), EM topo-cluster jets (EMTopo), and unified flow object jets (UFO). Only particle flow
 1097 jets will be discussed in greater detail due to their importance in this analysis. The following sec-
 1098 tions discuss jet identification in the calorimeters, particle flow jet construction using the anti- k_t
 1099 algorithm, jet clustering and jet substructure characteristics.

1100 5.4.1 Calorimeter Clusters

1101 Jets are first identified by the energy deposits they leave in the calorimeters. The reconstruc-
 1102 tion of jets in ATLAS begins with the construction of *topo-clusters*, which are topologically-grouped
 1103 noise-suppressed clusters of calorimeter cells [56]. The topo-cluster seed is a cell with an energy
 1104 that is at least 4× the average background noise level for the cell. Any cells adjacent to the seed
 1105 cell in three dimensions are added to the cluster if they have an energy deposit that is at least 2x

1106 the average expected noise. This process is repeated, growing the cluster, until no adjacent cells
1107 exceeding the energy deposit threshold remain. As a final step, all adjacent cells are added to the
1108 topo-cluster, irrespective of their energy.

1109 The construction process for topo-clusters allows for the possibility that several independent
1110 signatures are grouped into one topo-cluster. To correct for this, the topo-cluster is scanned for
1111 local maximum, defined by any cell with energy > 500 MeV, and no neighboring cells with greater
1112 energy. If more than one local maximum is identified, the topo-cluster is split among the corre-
1113 sponding energy peaks [57]. In the event that one cell neighbors two or more local maxima, the
1114 cell is assigned to the two highest-energy clusters that is neighbors. This means each cell is shared
1115 at most once, between at most two post-splitting topo-clusters.

1116 Two measurements for the total energy of the topo-cluster are considered. The raw, or electro-
1117 magnetic (EM), scale simply considers the sum of energy from all cells in the topo-cluster. The
1118 local cell weighting (LCW) scale first classifies clusters as electromagnetic or hadronic, and then
1119 applies appropriate corrections for hadronic interactions in the jet energy calculation [56]. The
1120 corrections are derived from Monte Carlo simulations, and account for the weaker response of
1121 ATLAS calorimeters to hadronic interactions (ATLAS calorimeters are *non-compensating*), and
1122 hadronic energy losses due to interactions with dead material [57].

1123 5.4.2 Particle Flow Algorithm

1124 The calorimeters provide excellent jet energy resolution for high energy jets. However, the
1125 granularity of the hadronic calorimeter is restricted to 0.1×0.1 in $\eta \times \phi$. Combining the infor-
1126 mation from the calorimeter with tracking information provides superior angular resolution and
1127 energy resolution. The particle flow (PFlow) algorithm is one of a handful of algorithms which
1128 can perform this task.

1129 An overview of the process is given in Figure 5.6. Tracks from the ID which are selected for the
1130 PFlow algorithm are required to have at least 9 hits in the silicon detector, and missing pixel hits in
1131 places where a hit would be expected. Additionally, the tracks have $p_T > 0.5$ GeV, and $|\eta| < 2.5$.

1132 The algorithm then attempts to match these tracks to EM scale calorimeter topo-clusters. This
1133 matching is performed using the distance metric

$$\Delta R' = \sqrt{\left(\frac{\Delta\phi}{\sigma_\phi}\right)^2 + \left(\frac{\Delta\eta}{\sigma_\eta}\right)^2} \quad (5.1)$$

1134 where σ_η and σ_ϕ represent the angular widths of the topo-clusters, and $\Delta\eta$ and $\Delta\phi$ represent the
1135 distance between the track, extrapolated to the second layer of the EM calorimeter, and barycenter
1136 of the topo-cluster [58]. The topo-cluster closest to the track as measured by $\Delta R'$ is considered
1137 matched to the track. If no topo-cluster is found within the cone size of $\Delta R' = 1.64$, it is assumed
1138 that particle which left the track did not form a topo-cluster in the calorimeter.

1139 The PFlow algorithm predicts the expected single topo-cluster energy for a given track, based
1140 on the track momentum and topo-cluster position. This value is then compared to the observed
1141 energy of the topo-cluster, and the probability that the particle energy was deposited in more than
1142 one topo-cluster is evaluated. If necessary, the algorithm adds more topo-clusters to the track/topo-
1143 cluster system, in order to account of the full shower energy of the track particle.

1144 To reduce the impact of double counting the energy of a given particle by including both its
1145 tracker and calorimeter energy measurements, the calorimeter energy measurements associated to a
1146 given track are subtracted from the total calorimeter measurement. If the expected energy deposited
1147 by the particle exceeds the topo-cluster energy, the full topo-cluster is removed. If the expected
1148 energy is less than the EM scale energy of all the considered topo-clusters, topo-cluster cells are
1149 removed one by one, until the full expected energy deposit of the particle has been removed from
1150 the calorimeter information. The resulting set of tracks and topo-clusters represent the event with
1151 no double-counting of energy between subdetectors [58]. This information is passed to the jet-
1152 finding algorithm.

1153 5.4.3 Jet Clustering

1154 When a parton decays in the detector, its energy deposits often result in multiple calorimeter
1155 clusters. For physics purposes, it is useful to combine clusters that likely resulted from an individ-

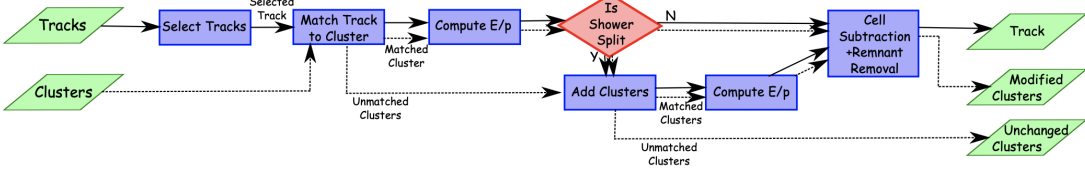


Figure 5.6: A flow chart illustrating the particle flow algorithm progression [58].

1156 ual parton decay, in order to reconstruct the parton. The process of grouping topo-clusters which
 1157 were produced by the same parton decay is *jet clustering*.

1158 The anti- k_t algorithm is the most commonly used algorithm for jet clustering in ATLAS. The
 1159 anti- k_t algorithm is based on sequential recombination algorithms [59]. A sequential recombina-
 1160 tion considers the distance d_{ij} between objects i and j (particles or pseudojets), and the distance
 1161 d_{iB} between an object i and the beam line B . If d_{ij} between two objects is the smallest distance
 1162 among those considered, i and j are combined into a pseudojet. The process continues until the
 1163 smallest distance is d_{iB} at which point the object i is determined to be a jet and removed from the
 1164 objects in consideration. The procedure is repeated with the remaining objects until there are none
 1165 remaining [54].

1166 The anti- k_t algorithm adopts this procedure, but modifies the distance measurements d_{ij} and
 1167 d_{iB} to consider the transverse momentum k_t :

$$d_{ij} = \min(k_{ti}^{2p}, k_{tj}^{2p}) \frac{\Delta_{ij}^2}{R^2}, \quad (5.2a)$$

$$d_{iB} = k_{ti}^{2p}. \quad (5.2b)$$

1168 The addition of the term p allows adjustments to algorithm which govern the relative power of
 1169 the momentum versus the geometrical scale $\Delta_{i,j}$, which is defined as $\Delta_{i,j} = (y_i - y_j)^2 + (\phi_i - \phi_j)^2$
 1170 where y_i and ϕ_i are respectively the rapidity and azimuth of particle i [54]. The radius parameter
 1171 R is chosen and determines the geometric cone size [59].

1172 In the case $p = 1$ the inclusive k_t algorithm [59] is recovered, which is a standard sequential

combination jet clustering algorithm. In the case $p = 0$, the Cambridge/Aachen sequential combination algorithm [60] is recovered. The case $p = -1$ gives rise to the anti- k_t algorithm. The impact of this choice means that the distance d_{ij} between many soft particles is larger than between soft and hard particles. Therefore, soft particles tend to cluster with hard ones before they cluster with other soft particles. They key feature of this behavior is that soft particles do not modify the shape of the jets. This leads to the creation of circular conical jets, a desirable feature which sequential combination algorithms and cone algorithms struggle to achieve. Figure 5.7 compares anti- k_t jet formation with the inclusive k_t and Cambridge/Aachen algorithms mentioned here, as well as the SIScone algorithm [61], which checks for sets of stable cones compatible with the observed radiation.

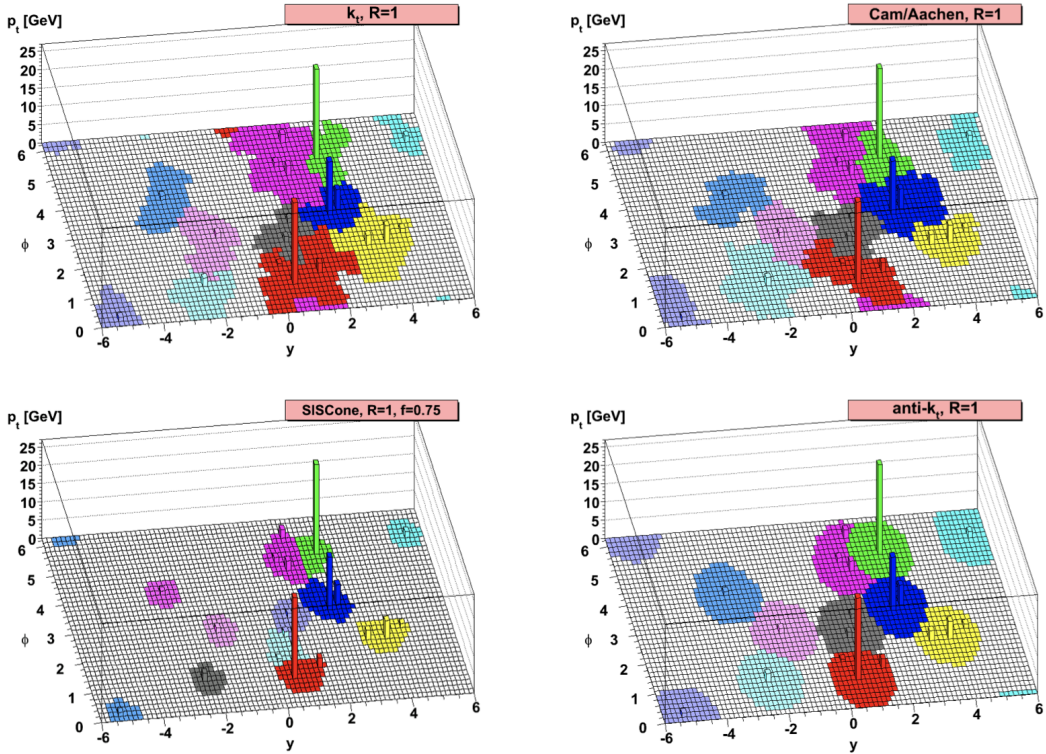


Figure 5.7: A comparison of jet clustering with four different jet algorithms. The anti- k_t algorithm is observed to create the most conical jets, where the shape of the jet is immune to the presence of soft radiation [54].

Any useful jet clustering algorithm must satisfy the requirements of infrared safety and collinear

1184 (IRC) safety. Infrared safety implies that the resulting set of jets is unaltered by the presence of
1185 additional soft particles in the list of seed clusters. As explained above, the anti- k_t algorithm is
1186 natural infrared safe. Collinear safety requires that the final set of jets is not impacted by collinear
1187 splitting of one of the jets. If the hardest particle p_1 is split into a collinear pair (p_{1a}, p_{1b}) (as
1188 is common in the fragmentation process for a hard parton), the jet clustering algorithm must
1189 still recognize (p_{1a}, p_{1b}) as the hardest jet in the collision. If another softer particle p_2 with
1190 $p_{t,1a}, p_{t,1b} < p_{t,2} < p_{t,1}$ is instead considered the hardest particle in the event, a different final
1191 set of jets would be returned. Collinear safety is a requirement of perturbative QCD, to ensure
1192 non-divergent higher-order calculations [62]. The anti- k_t algorithm's tendency to cluster hard par-
1193 ticles first ensures its collinear safety. By satisfying the IRC safety requirement, anti- k_t jets can be
1194 calculated using perturbative QCD, which improves comparisons with theory.

1195 5.4.4 Ghost Track Association

1196 Once a collection of jets has been created, the jet objects can be studied at both the event-level
1197 and the jet-level. In the event-level picture, the momentum, energy, and geometric orientation
1198 of the jets within an event are considered. This yields important information about decay of any
1199 resonant heavy objects, the total energy in the event, and the distribution of energy amongst the jets.
1200 At the jet-level picture, the particles composing the jet are considered. The momentum, energy,
1201 and geometric orientation of the particle tracks provides a low-level picture of the jet, which can
1202 help determine if the properties of the jet are consistent with standard QCD, or if new physics
1203 processes might be represented within the patterns found in the constituent particles. Jet-level
1204 analysis is also widely used in flavor tagging.

1205 For anti- k_t jets with a radius parameter $R = 0.4$, one way of studying the jet-level picture
1206 is through considering the ghost-associated tracks. Track association is process of determining
1207 which tracks should be considered associated with a given jet. In the ghost association algorithm,
1208 the anti- k_t clustering algorithm is used for the collection of tracks and calorimeter clusters [63].
1209 However, the tracks are considered to have infinitesimal momentum (*ghosts*), so their addition to

1210 a jet object does not alter the four-momentum of the jet. This ensures the final jet collection is not
1211 altered by the presence of the ghost tracks in the reclustering, but information about the associated
1212 tracks for each reconstructed jet becomes available [64].

1213 Ghost tracks are of particular importance to this analysis, as a means of providing a low-level
1214 picture of the shape of $R = 0.4$ jets, and discriminating Standard Model QCD-like jets from dark
1215 QCD-like jets.

1216 5.5 Missing Transverse Energy

1217 A simple principle leveraged in ATLAS physics analyses is checking for conservation of mo-
1218 mentum among the products of any pp collisions. The initial state transverse momentum of any
1219 pp collision is always zero, so the transverse momentum of all final state particles should likewise
1220 be zero. The missing transverse energy, E_T^{miss} , is determined by the magnitude of the negative
1221 momentum vector sum of all final state objects resulting from the pp collision.

1222 Specifically, the objects considered in the E_T^{miss} calculation are photons, electrons, muons, jets,
1223 and soft terms. The first four items comprise the hard components of the E_T^{miss} calculation, and
1224 have been discussed previously in this chapter. The final item represents a collection of *soft terms*,
1225 comprising any detector signals not associated to hard detector objects. These can be based on
1226 unassociated tracks, or unassociated soft calorimeter clusters. Both are generally not used in the
1227 same calculation to avoid double counting of soft terms. In this analysis the calorimeter cluster
1228 soft terms are considered in the E_T^{miss} calculation.

1229 E_T^{miss} can arise due to non-interacting Standard Model objects such as neutrinos, fake sources
1230 such as mis-reconstructed objects and dead detector regions, or in some theories, non-interacting
1231 BSM objects such as a dark matter candidate particles. To understand the amount of E_T^{miss} at-
1232 tributable to detector noise and mis-reconstruction, E_T^{miss} is studied in $Z \rightarrow \mu\mu$ where little real
1233 E_T^{miss} is expected [65]. As Figure 5.8 illustrates, the resolution of E_T^{miss} generally decreases as
1234 E_T^{miss} increases, due to detector resolution effects. As E_T^{miss} is an important quantity for most dark
1235 QCD analyses, limitations in the accuracy of the E_T^{miss} calculation must be considered.

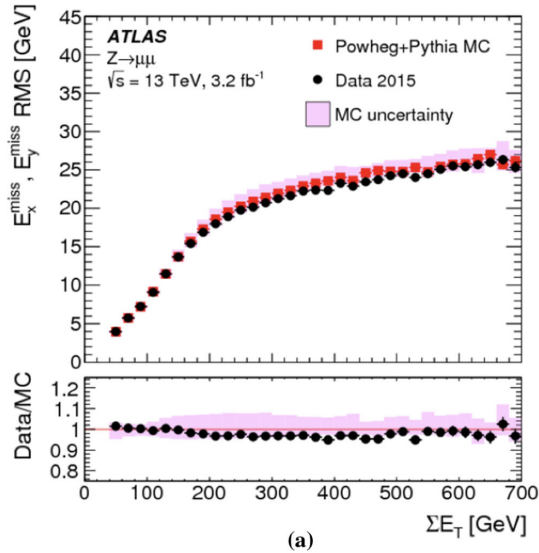


Figure 5.8: A comparison of MC simulation and data for $Z \rightarrow \mu\mu$ events where real $E_T^{\text{miss}} = 0$ [65]. The resolution of the missing energy in the transverse ($x - y$) plane is observed to increase with increasing total $\sum E_T$.

1236

Part III

1237

Search

1238

1239

Chapter 6: Monte Carlo and Data

1240 The search for semi-visible jets via s-channel production presented in the following chapters is
1241 performed with 139 fb^{-1} of proton-proton collision data collected by the ATLAS detector during
1242 Run 2 (2015 - 2018). The full Run-2 dataset is used for the final interpretation. Monte Carlo
1243 (MC) simulations of background processes and the semi-visible jet signal process are used in the
1244 development of the analysis strategy, and in the final interpretation to set limits on the observed
1245 cross-section of the signal model. This chapter will provide details about the full Run-2 dataset,
1246 and the background MC simulations, and the signal MC simulations used in this search.

1247 **6.1 Data**

1248 The 139 fb^{-1} of proton-proton collision data is selected according to the *good runs list* (GRL),
1249 which identify runs with good detector conditions that are suitable for physics evaluation. Events
1250 are further selected to pass a single-jet trigger selection, where events are required to have a jet at
1251 trigger-level with a p_T that exceeds a certain value. The lowest p_T unprescaled single jet trigger
1252 threshold for each period is as follows:

- 1253 • 2015: $p_T \geq 360 \text{ GeV}$
- 1254 • 2016 & 2017: $p_T \geq 380 \text{ GeV}$
- 1255 • 2017: $p_T \geq 380 \text{ GeV}$
- 1256 • 2017 & 2018: $p_T \geq 420 \text{ GeV}$

1257 A post-trigger selection of jet $p_T > 450 \text{ GeV}$ ensures all these triggers are fully within their
1258 efficiency plateaus. The jet collection used is anti- k_t EM particle flow jets with a radius parameter
1259 of $R = 0.4$, also referred to as small-R jets.

1260 Due to the variance in visible and invisible momenta due to the R_{inv} parameter of the signal
1261 model, many signals also have significant E_T^{miss} . The use of a E_T^{miss} trigger to select events was
1262 considered, and the single jet approach described here was found to preserve more signal events
1263 across the grid, particularly in the high resonance mass and low R_{inv} region of phase space. These
1264 studies are documented in Appendix A.

1265 The data are subject to a blinding strategy throughout the analysis design so as to mitigate
1266 analyzer-induced bias. Blinded and unblinded region definitions are described further in Sec-
1267 tion 8.1.

1268 6.2 Simulation

1269 Simulated events are generated with a variety of Monte Carlo (MC) generator processes that
1270 run in stages. The pp hard scatter physics process is simulated, and the final state particles are
1271 subsequently showered and decayed. This full description of the event is then propagated through
1272 a detailed detector simulation based on GEANT4 [66]. The MC simulation is weighted to match
1273 the distribution of the average number of interactions per bunch crossing μ observed in collision
1274 data.

1275 All simulated samples included in this analysis were produced with three different campaigns:
1276 `mc20a` corresponds to 2015-2016 data-taking conditions, `mc20d` to 2017, and `mc20e` to 2018.
1277 These three campaigns are weighted to the integrated luminosities of their respective data-taking
1278 periods and combined to produce simulation for the entire Run 2 dataset. Simulated events are
1279 reconstructed with the same algorithms run on collision data.

1280 6.2.1 Simulated Backgrounds

1281 Though the final background estimation is data-driven, background MC is studied for analysis
1282 optimization and machine learning tool development.

1283 Dijet QCD is the dominant background process. QCD is simulated with PYTHIA8 [67], and
1284 generated in approximate slices of p_T , to ensure high statistics across the momentum spectrum.

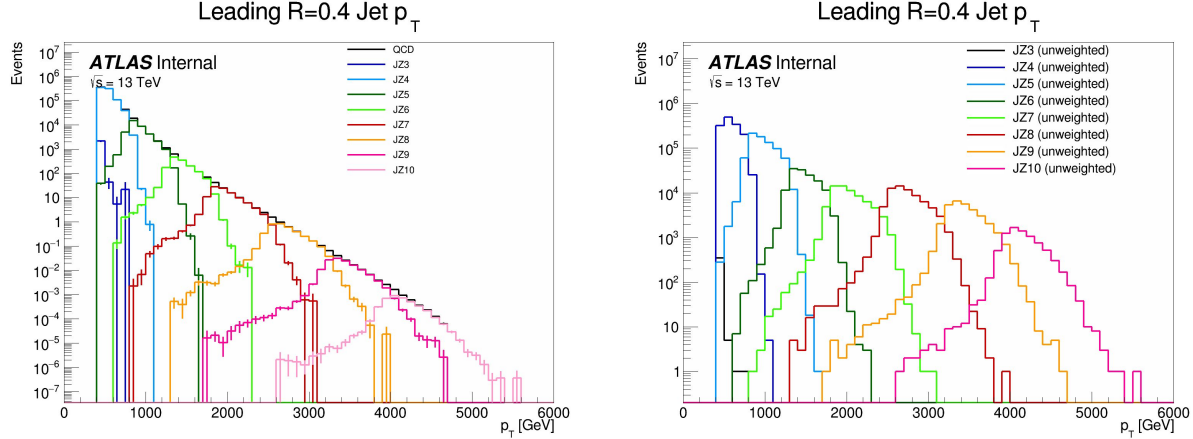


Figure 6.1: The transverse momentum slices of the QCD MC simulation, overlayed to show how they come together to create a smooth distribution (left) once weighted properly. The original unweighted distribution is shown on the right, illustrating the enhanced statistics for the high p_T range.

1285 The slices are then reweighted using MC generated event weights to create a physical distribution.

1286 Figure 6.1 illustrates the 8 momentum slices used in this analysis.

1287 Due to presence of E_T^{miss} in the SVJ signals, additional MC background processes are required
 1288 to create a full picture of the relevant background. The $Z \rightarrow vv$ process contributes to the back-
 1289 ground due to its high missing energy. Leptonic W/Z decays and W/Z+jets are also included as
 1290 they can contribute both additional missing energy and significant hadronic activity. Single top
 1291 and $t\bar{t}$ processes are also considered for their contribution to hadronic activity,. The background
 1292 composition in the selected region (discussed in Section 8.1) is 76% QCD, 12% W/Z+jets, 8%
 1293 top and $t\bar{t}$ processes, and 4% $Z \rightarrow vv$. Figure 6.2 illustrates the background composition for the
 1294 analysis.

1295 6.2.2 Signal Simulation

1296 The Hidden Valley signal model implementation is based on Ref [22]. The s-channel semi-
 1297 visible jet model is governed by a number of parameters. The mass of the mediator $m_{Z'}$ can be set,
 1298 together with the couplings of the Z' to the visible and dark quarks g_q and g_{q_D} . The dark sector
 1299 shower is governed by the number of dark colors N_{c_D} , the number of dark flavors N_{f_D} , and the

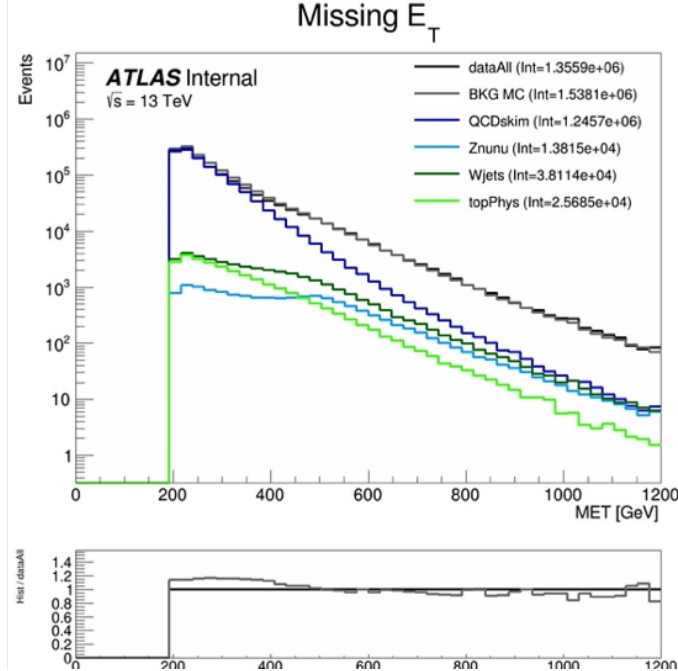


Figure 6.2: Background processes relevant to the SVJ signal. The agreement between the black line (data) and grey line (all MC processes combined) illustrates that this collection of background processes is sufficient to model the expected E_T^{miss} in the selected data events.

1300 dark sector confinement scale Λ_D . There is also the characteristic scale of the dark hadrons m_D ,
 1301 which determines the mass of the dark hadrons, which can be pseudoscalars m_{π_D} or vectors m_{ρ_D} .
 1302 Finally, the average fraction of invisible particles in the final state jet is dictated by R_{inv} .

1303 The chosen parameters for this model were carefully selected in collaboration with theorists to
 1304 be compatible with the new benchmarks established in the 2021 Snowmass process [21]. These pa-
 1305 rameters reflect extensive communication with the Snowmass, CMS, and theory teams. The signal
 1306 generation allows for up to two initial state radiation jets, and uses an MLM merging scheme [67]
 1307 to match jets to the original partons.

1308 The choices of fixed parameters for the Pythia8 HV model are summarized in Table 6.1. A
 1309 detailed discussion of these parameters and their implications on the dark shower topology can be
 1310 found in Ref. [21]. The mass choices for the dark quark and the dark hadrons are also summarized
 1311 in Table 6.2.

1312 Note that the number of dark flavors differs from the Snowmass recommendation of $N_{f_D} = 4$.
 1313 This change is minimal in impact because R_{inv} is set explicitly (rather than allowing it to arise

Parameter	Value
HiddenValley:Ngauge	3
HiddenValley:alphaOrder	1
HiddenValley:Lambda	10.0
HiddenValley:nFlav	2
HiddenValley:spinFv	0
HiddenValley:FSR	on
HiddenValley:fragment	on
HiddenValley:pTminFSR	1.1
HiddenValley:probVector	0.58

Table 6.1: Fixed parameters in the Pythia8 HV model

Parameter	Value [GeV]
m_{π_D}	17
m_{ρ_D}	31.77
m_{q_D}	10

Table 6.2: Values for m_{dark}

naturally from the HV theory), and allows us to remain more comparable with the CMS semi-visible jets analysis and the ATLAS t-channel analysis.

The mediator mass $m_{Z'}$ and the fraction of invisible particles in the final state R_{inv} vary, and are used to define the search grid. $m_{Z'}$ varies between 2.0 TeV and 5.0 TeV, while R_{inv} varies from 0.2 to 0.8. R_{inv} values of 0.2, 0.4, 0.6, and 0.8 are generated for each $m_{Z'}$ mass point. Table 6.3 illustrates the signal grid and the associated cross-section for each signal.

Samples are generated using MADGRAPH5 [68] version 2.9.9 interfaced to PYTHIA8.244P3 [67] for shower and hadronization with NNPDF23LO PDF [69] and the ATLAS A14 [70] to tune the underlying event data.

$m_{Z'}$ (GeV)	Cross section (fb)
2000	2.52e+2
2500	7.42e+1
3000	2.45e+1
3500	8.83e+0
4000	3.49e+0
5000	7.57e-1

Table 6.3: Mass points and cross sections of the SVJ search signal grid

1323

1324

Chapter 7: Machine Learning Tools

1325 **7.1 Introduction**

1326 The search for semi-visible jets presents an opportunity to use novel machine learning (ML)
1327 tools to uncover patterns in the behavior of dark QCD. The subtlety of the shower differences be-
1328 tween dark and SM QCD motivates a complex model that can accept high-dimensional low-level
1329 inputs to best understand key differences between signal and background correlations. Addition-
1330 ally, the large number of theory parameters which can be chosen arbitrarily and affect the shape of
1331 the dark QCD shower motivate exploring a data-driven machine learning approach, which could
1332 be sensitive to a wider variety of dark QCD behavior.

1333 To this end, two machine learning approaches are developed for this search, which are used
1334 in tandem. The first is a supervised ML method where the ML algorithm is built to maximize
1335 exclusion sensitivity to the specific generated SVJ signal models used in this analysis. Here, su-
1336 pervised refers to the use of full and correct labels for all events considered during model training,
1337 which necessitates training over simulated data. The second is a semi-supervised method, where
1338 training of the model is data-driven and labels are only partially provided during training. The
1339 semi-supervised ML algorithm broadens the discovery sensitivity of the search, and reduces the
1340 dependence on the exact theory parameters chosen for signal model simulation.

1341 The two different ML algorithms used in this approach will be explained in the following
1342 sections, along with their application in the SVJ analysis strategy.

1343 7.1.1 Particle Flow Network (Supervised)

1344 **Architecture Fundamentals**

1345 A Particle Flow Network (PFN) [71] architecture is selected for two reasons: *permutation in-*
1346 *variant input modeling* to best describe the events consisting of an unordered set of particles, and a
1347 *low-level input modeling* using tracks to take advantage of the available high-dimensional informa-
1348 tion to best exploit available correlations within the event. Permutation invariant input modeling
1349 is an architecture priority as ordered input modeling has been observed to bias the performance of
1350 low-level modeling tools as in [72]. Low-level input modeling is an architecture priority to capture
1351 the intricacies of dark QCD showers which may not express themselves in higher level variables,
1352 as explored in [22]. A comparison to a high-level *boosted decision tree* (BDT) is available in
1353 Appendix B.3.

1354 The PFN is used to model input events as an unordered set of tracks. Given the inherently
1355 unordered and variable-length nature of particles in an event, this choice of modeling as a *set*
1356 can enable the model to better learn the salient features of the dataset that enable a signal-to-
1357 background classification. Constructing the PFN involves the creation of new basis variables \oplus
1358 for each particle in the event. Permutation invariance is enforced by summing over the \oplus basis for
1359 every particle in the event to create a new permutation invariant latent space basis O . Finally the
1360 classifier F is a function of the sum over this new basis. The creation of the latent space basis O
1361 from M particles \vec{p} with d features each can be expressed as:

$$O(\{\vec{p}_1, \dots, \vec{p}_M\}) = \sum_{i=1}^M \Phi_i(\vec{p}_i) \quad (7.1)$$

1362 where $\Phi : \mathbb{R}^d \rightarrow \mathbb{R}^l$ is a per particle mapping, with l being the dimension of the new basis O .
1363 Figure 7.1 gives a graphical representation of the use of summation in the PFN over per-particle
1364 information to create a permutation-invariant event representation.

1365 Figure 7.2 provides an annotated diagram of the PFN architecture as used in this analysis.

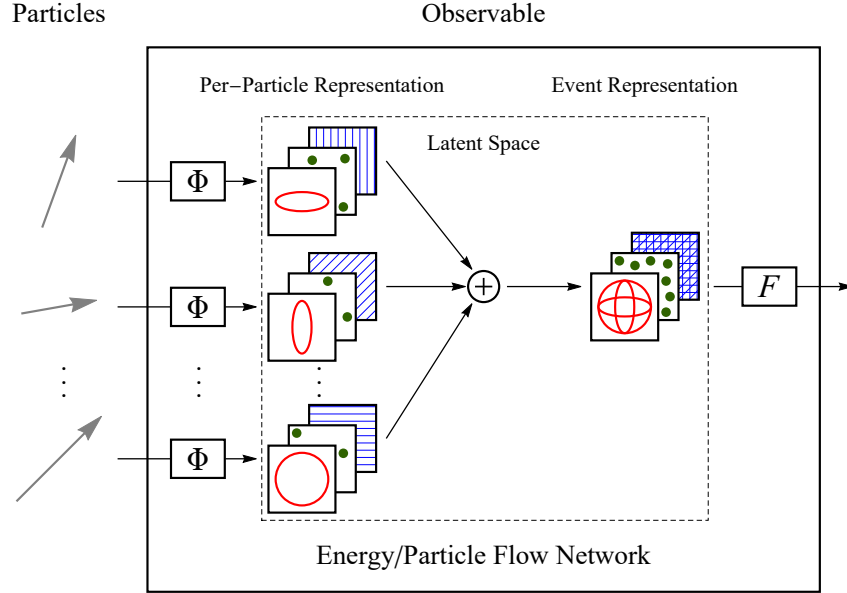


Figure 7.1: The Energy/Particle Flow Network concept, from Ref. [71].

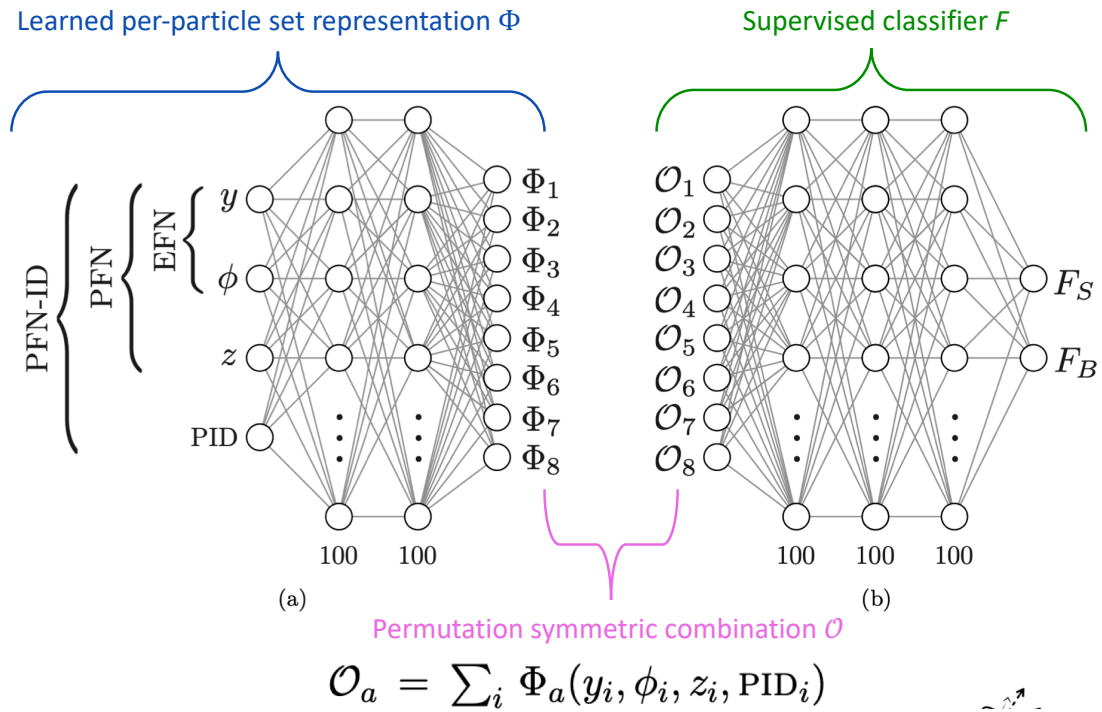


Figure 7.2: An annotated diagram of the PFN architecture. y and ϕ represent geometric information for the input particles, z represents energy information, and PID encompasses any other particle ID information in the input.

1366 **Input Modeling, Scaling, and Rotation**

1367 In this implementation, the particle input information comes from all tracks associated to the
1368 leading and subleading jets. The track association method is Ghost association, as discussed in
1369 Section 5.4.4. A single jet tagger strategy was also considered, but utilizing tracks from both
1370 leading jets creates a complete low-level picture of the event, which both focuses on the objects
1371 most likely to be associated to the decay of the dark quark (as will be justified in Chapter 8)
1372 and the relationship between those objects. If we consider the dijet topology of semi-visible jets
1373 as illustrated in Figure 7.3, the advantage of modeling both leading jets simultaneously becomes
1374 clear. In the semi-visible jet model presented in [22], E_T^{miss} in the event is expected to arise due to
1375 an imbalance in the number of visible tracks of the two jets associated to the dark quark decay.

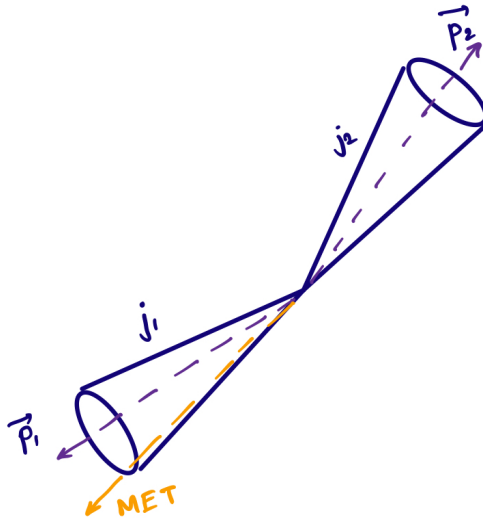


Figure 7.3: A illustration of the expected dijet behavior of semi-visible jets, where one jet is closely aligned with E_T^{miss} .

1376 Each track is described using six variables: the four-vector of the track (p_T , η , ϕ , E), and the
1377 track displacement parameters d_0 and z_0 , where d_0 measures displacement in the radial direction
1378 from the beamline and z_0 measures displacement along the beamline from the primary interac-
1379 tion point. Figure 7.4 illustrates these coordinates. Up to 80 tracks per jet are allowed, which is
1380 a threshold chosen to generally include all the tracks in the jet, which leads to maximal perfor-

1381 mance. Figure 7.5 shows the track multiplicity in the leading and subleading jet for the signal and
 1382 background samples used in training.

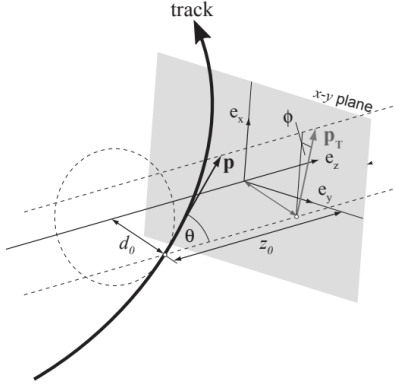


Figure 7.4: Illustration of track coordinates d_0 and z_0 .

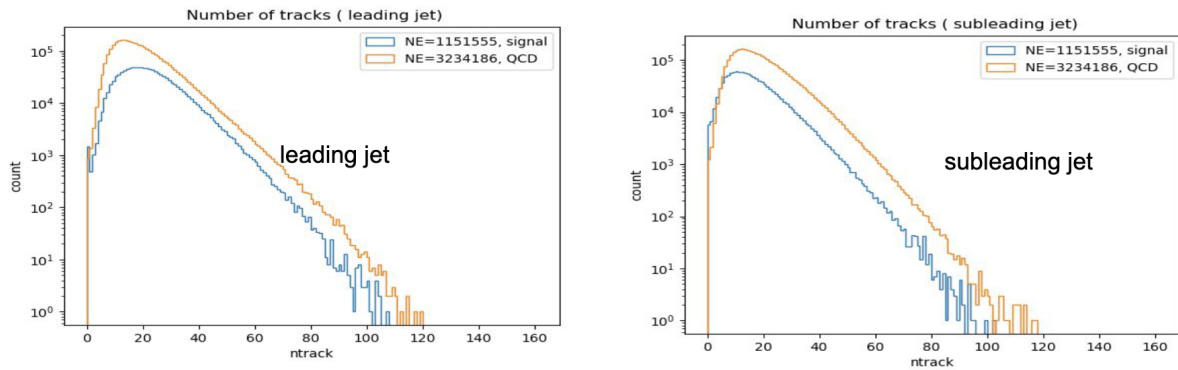


Figure 7.5: Distributions of the track multiplicity in the leading and subleading jets, comparing signal and background PFN training samples.

1383 These tracks (up to 160 total) are the input to the PFN. Referencing Equation 7.1, this corre-
 1384 sponds to $M = 160$ and $d = 6$. The two leading jets and their associated tracks are rotated so
 1385 that the center of the system is aligned with $(\eta, \phi) = (0, 0)$. Each track is normalized to its relative
 1386 fraction of the total dijet system energy and transverse momentum- this enforces agnosticism to the
 1387 total energy and transverse momentum of the event. The rotation and scaling are motivated by the
 1388 procedures described in [71] to improve the optimality of the PFN learning. Figure 7.6 illustrates
 1389 the rotation process.

1390 Finally, each of the 6 track variables is scaled so that its range is $[0,1]$. This is a common

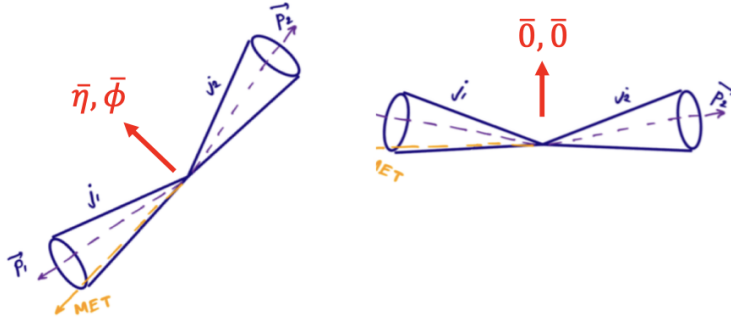


Figure 7.6: A diagram demonstrating how the two jet system is rotated in (ϕ, η) .

1391 preprocessing step that ensures the input data is bounded over a similar range, so that arbitrarily
 1392 large values don't develop an outsized impact on the model. Figure 7.7 show each of 6 track
 1393 variables before and after scaling and rotation have been applied, demonstrating the impact of
 1394 these procedures, as well as the track level similarities differences between the background SM
 1395 QCD processes and the signal SVJ processes. Figure 7.8 illustrates that the data is well modeled
 1396 by the MC at track level.

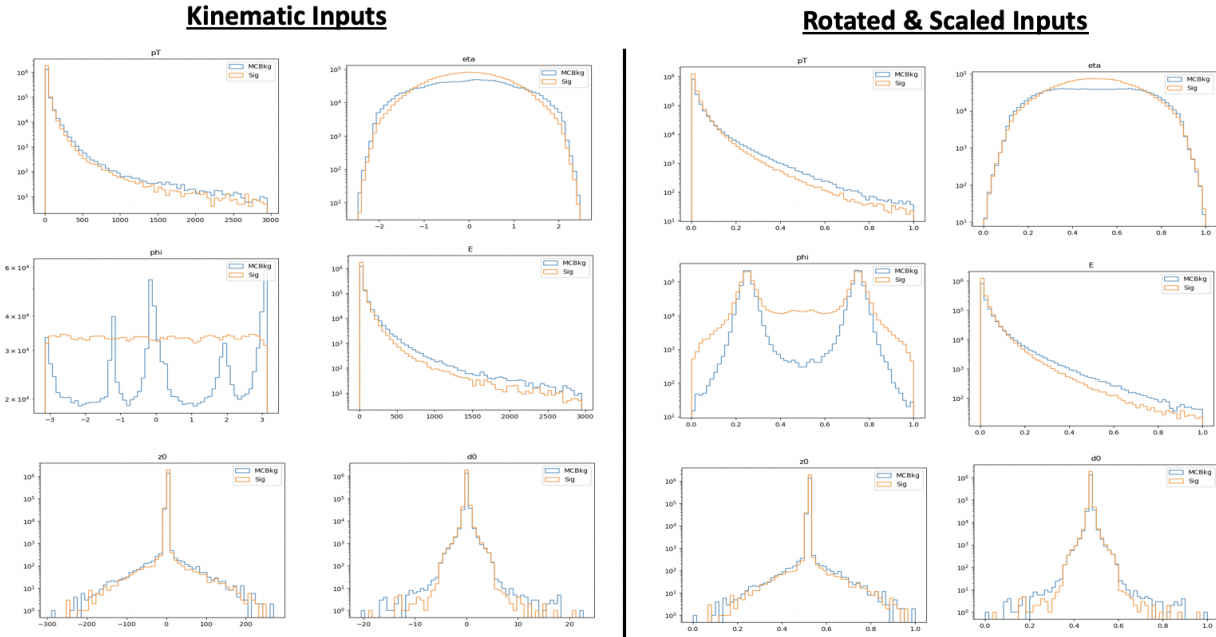


Figure 7.7: The 6 PFN track variables in background MC and signal MC. There are some differences between signal and background, but the track kinematics are largely similar.

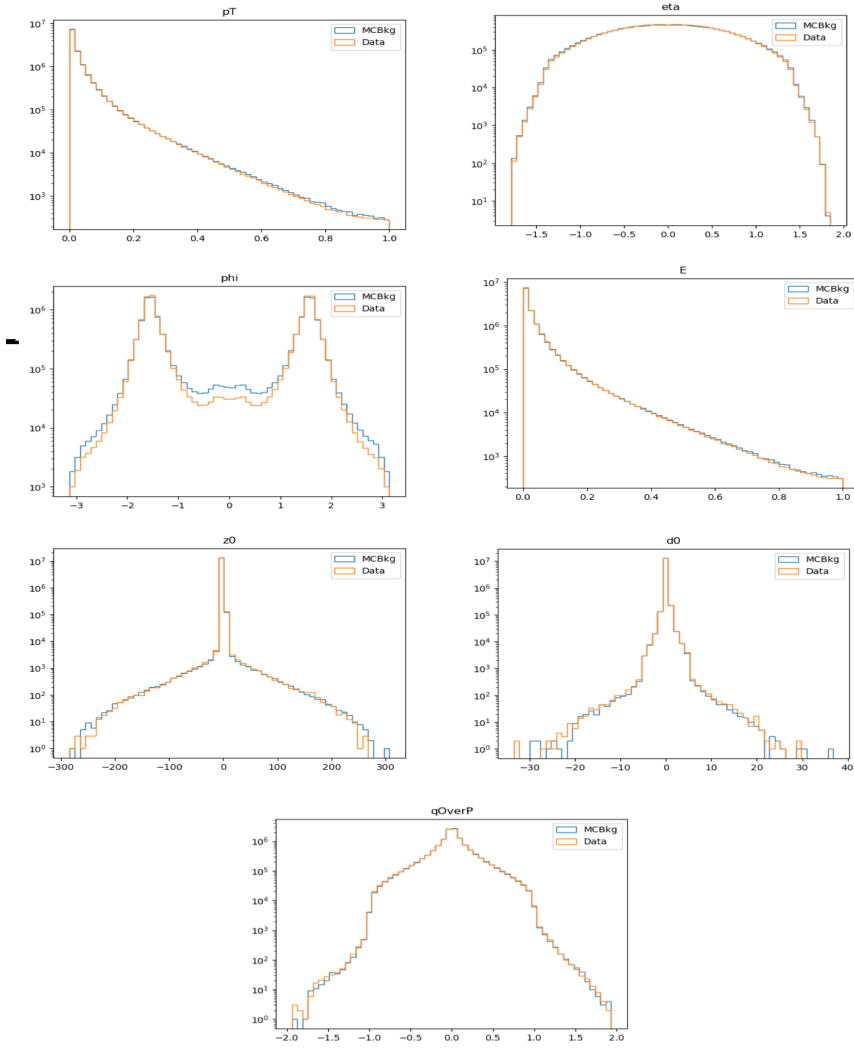


Figure 7.8: The 6 PFN track variables in data and background MC, after the scaling and rotation procedure is applied. There is excellent modeling of the data by the MC within the track variables. The slight discrepancy in the phi distribution is due to the modeling of dead TileCal cells by the QCD MC, which will be discussed in Chapter 8. The level of discrepancy is determined to be within tolerance given that the final result will be data driven and the QCD model is used in the PFN training only.

1397 **Training**

1398 As seen in Figure 7.2, two separate architectures are defined and combined to do the super-
1399 vised training. The PFN uses a masking layer to suppress any zero-padded inputs, making the
1400 architecture length agnostic. The masking layer ignores any all-zero inputs in the summation layer.
1401 Additionally, The summation layer in the PFN enforces permutation invariance, so the network is
1402 unordered. The Φ network has 3 dense layers of dimensionality 75 with RELU activation, with
1403 27.5k trainable parameters and an output Φ latent space dimension of 64.

1404 The classifier F network similarly has 3 dense layers with 75 nodes with RELU activation, and
1405 a final softmax layer to determine the event-level classification with a categorical cross-entropy
1406 loss. The Adam optimizer is used with an initial learning rate of 0.001.

1407 The PFN is trained in a fully supervised way using SVJ signal MC and QCD MC events. Al-
1408 though several SM processes are expected to contaminate the SR (see Chapter 8), QCD is the dom-
1409 inant background. Training against a QCD-only sample is determined to produced better results
1410 than training on a more complete background - when training with a background which repre-
1411 sents samples that are more enriched in E_T^{miss} , the ability of the PFN to identify high E_T^{miss} signals
1412 is reduced. When training with a QCD-only background, there is greater contamination from
1413 E_T^{miss} enhanced backgrounds in the final SR - however the increased signal acceptance means that
1414 overall sensitivity is still higher with a QCD-only training. This can be seen in the comparison of
1415 output classifier distributions in Figure 7.9.

1416 500k events from both background and signal are used in training, where the signal is a com-
1417 bined file of all simulated signal points and the full QCD background which is sampled according
1418 to it's MC weights to produce the proper p_T input shape. A study was done to check the optimality
1419 of the inclusive signal model PFN as compared to one trained on high and low R_{inv} points sepa-
1420 rately, to better capture the differences in high and low E_T^{miss} across signals and backgrounds, but
1421 a small effect is found and the decision is taken to keep the inclusive model (Appendix B.2).

1422 The network is trained for 100 epochs. A train/test/validation split of 78%, 20%, and 2% is used
1423 for the final PFN training. Figure 7.10 shows the loss during training, which is stable and flattens

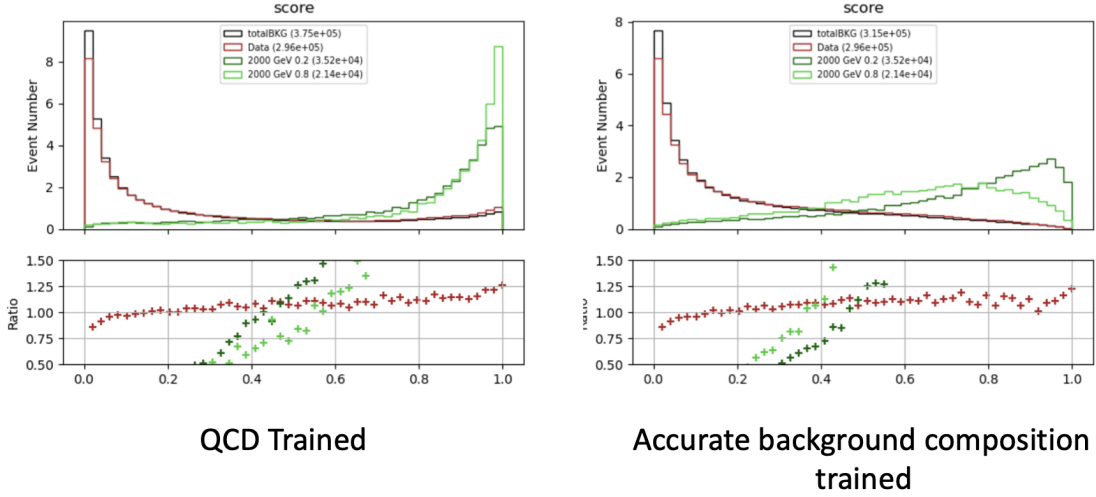


Figure 7.9: PFN score for background MC, data, and signal, comparing a PFN training on QCD-only vs all-background MC samples. The average AUC for the QCD-only training (left) is 0.93, while the average AUC for the mixed background training (right) is 0.84. The sensitivity estimate across the grid is better for the QCD-only training - from the distribution we can conclude that this is because the sensitivity to MET enhanced signals is greatly reduced.

1424 by the end of training, and the final evaluated losses that provide signal-background discrimination
 1425 over the test set.

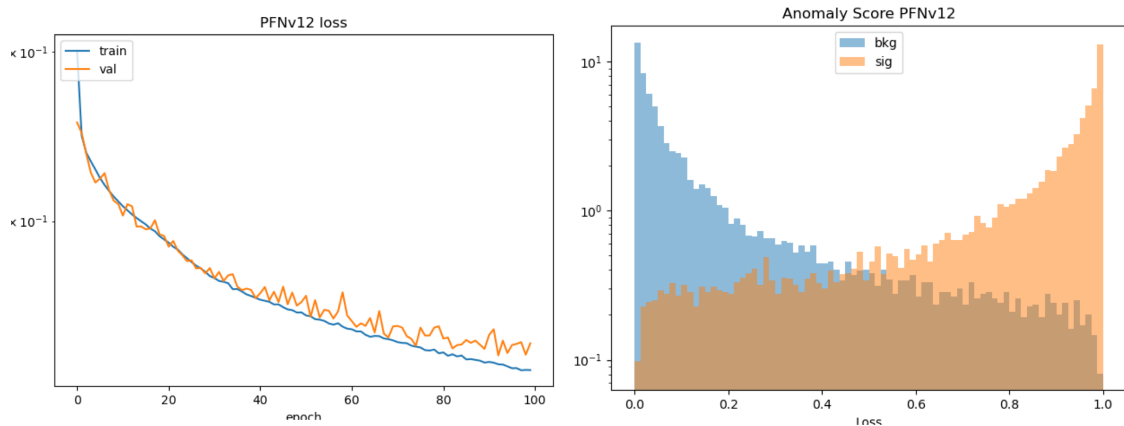


Figure 7.10: PFN architecture loss during training as a function of epoch (left) and the evaluated loss over the signal and background (right).

1426 Optimization studies were performed on the PFN, varying the number of training epochs, num-
 1427 ber of training events, batch size, learning rate, number of neurons, and dimension of the Φ space.
 1428 A summary of these studies is presented in Appendix B.2. The model presented here represents an
 1429 optimal choice across these parameters.

1430 **Performance**

1431 The performance of the PFN can be assessed via the area-under-curve (AUC) of the receiver
1432 operating characteristic (ROC) associated to evaluating the PFN on the test set of signal and back-
1433 ground events. Figure 7.11 shows the ROC curve of the PFN when classifying the QCD back-
1434 ground from the combined signal, with an AUC of 0.93. Figure 7.12 shows the AUC of the PFN
1435 across the SVJ signal grid, demonstrating strong discrimination capability even in the varying cor-
1436 ners of phase space. Figure 7.13 shows the output score distribution in two signals, data, and the
1437 total background MC. A selection of PFN score > 0.6 for all SR events is chosen to maximize
signal sensitivity across the grid.

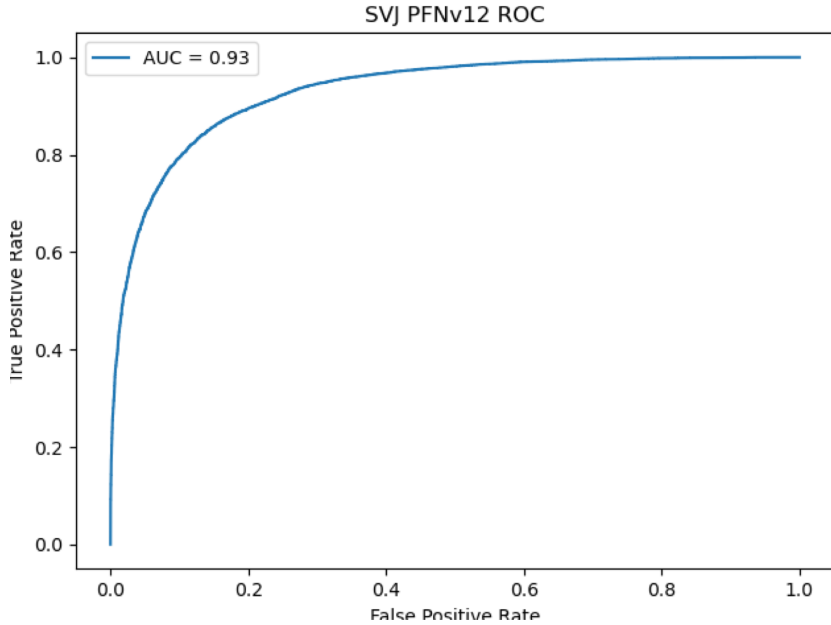


Figure 7.11: ROC the PFN score for combined signal (true positive) and QCD background (false positive).

1438

1439 Another supervised approach was studied using a BDT as the primary selection tool, trained
1440 over high-level variables describing each event. Studies comparing the PFN and BDT approaches
1441 are provided in Appendix B.3. Ultimately the low-level high-dimensional approach offered by the
1442 PFN was selected for its increased performance and lessened kinematic dependence.

1443 Appendix B shows more studies on the ML methods and comparisons of varying approaches.

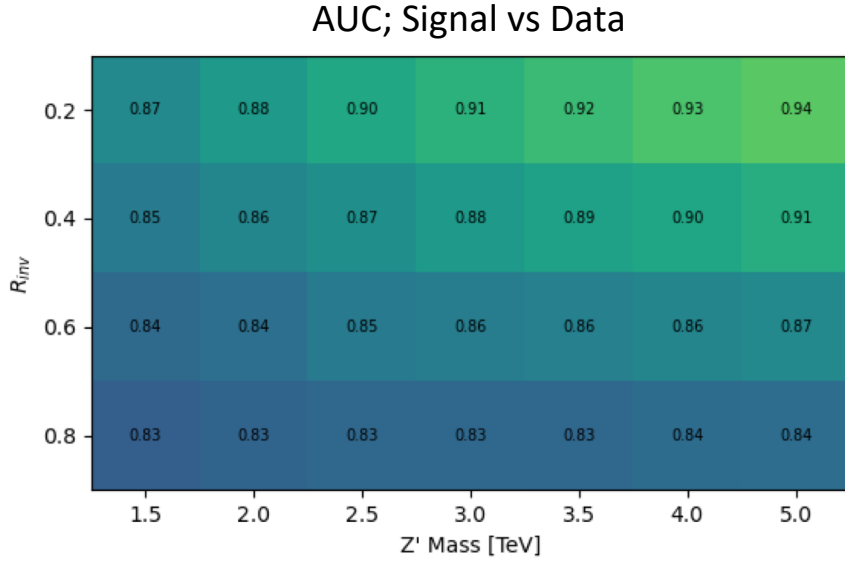


Figure 7.12: AUC from the PFN score for each signal in the SVJ grid, shown versus the QCD-only training sample.

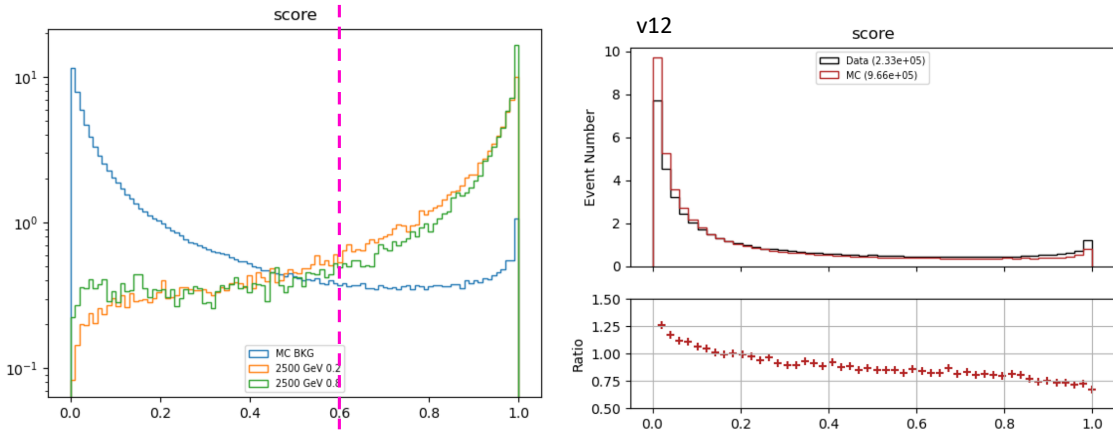


Figure 7.13: PFN score for two signals and the total background MC (top), and between data and MC (bottom). The difference between data and MC efficiency is minimal (< 5%).

1444 7.1.2 ANTELOPE (Semi-supervised)

1445 The semi-supervised analysis approach broadens the discovery sensitivity of the search through
1446 the use of semi-supervised ML, where training of the model is data-driven and labels are only
1447 partially provided during training. While broad sensitivity is a general key goal of LHC searches,
1448 it is particularly motivated in the case of dark QCD models, which can lead to widely varying
1449 topologies depending on the values of model parameters. In the case of SVJs, the R_{inv} fraction in
1450 the jet can dramatically vary the E_T^{miss} , shower shape, and other key features, making it difficult to
1451 find a single standard analysis variable that can distinguish all signal topologies from QCD.

1452 **Architecture Fundamentals**

1453 The model-independent search region of this analysis is implemented with a novel ML ap-
1454 proach that builds on the ANTELOPE architecture to construct a tool that is capable of performing
1455 low-level anomaly detection with permutation-invariant inputs. This tool, referred to as **ANomaly**
1456 **deTEction on particLe flOw latent sPacE (ANTELOPE)**, is a custom solution designed for this
1457 analysis.

1458 ANTELOPE uses the supervised signal vs. background training of the PFN network described
1459 in the previous section to generate a permutation invariant latent space that is representative of the
1460 original input variables, encodes the input events into these latent space variables O , and trains a
1461 *variational autoencoder* (VAE) over the events modeled as PFN latent space variables. A VAE
1462 is a common architecture used for anomaly detection and data-driven ML training. It has been
1463 used in previous ATLAS searched to model jet level information, such as the search presented
1464 in [73] using the recurrent architecture described in [72]. One of the limitations of a recurrent
1465 architecture is the need to order the low level inputs, which affects the performance of the tool. Jet
1466 constituent information is intrinsically unordered, and therefore a permutation invariant approach
1467 removes this element of arbitrary decision making from the modeling process. A visual example
1468 of the ANTELOPE inputs is given in Figure 7.14.

1469 The input to the model is the same 6 track variables for the leading 160 tracks of the leading

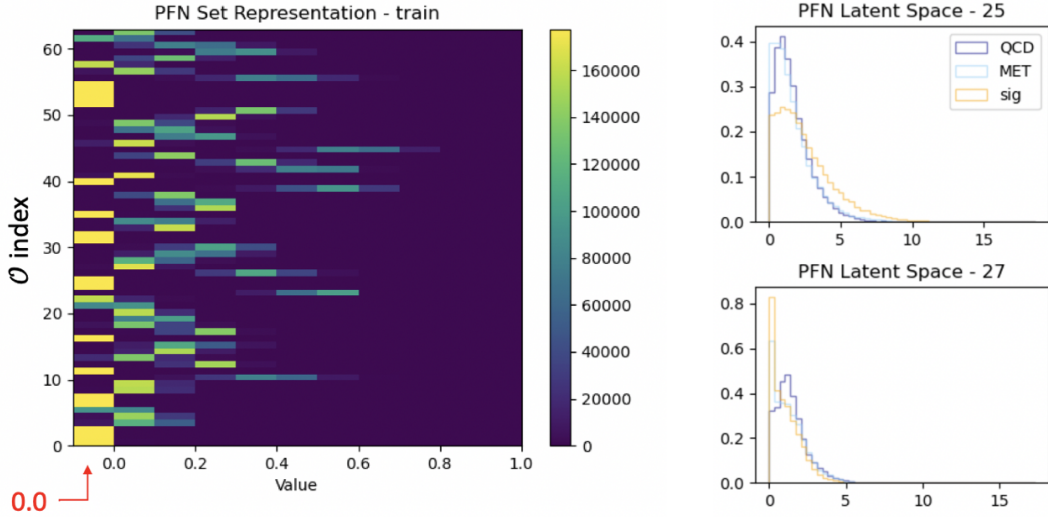


Figure 7.14: A visual representation of the 64 PFN latent space variables which create the input of the VAE component of ANTELOPE. The left shows a 2D histogram of the PFN latent space index (0-63) versus the value assumed by that index. The right shows 1D histograms of two particular PFN latent space variables.

1470 two jets, as presented in Section 7.1.1. The track information is encoded to the PFN Φ latent
 1471 space using the pre-trained Φ network (trained according to the steps outline in Section 7.1.1. The
 1472 resulting Φ basis is summed to created the fixed length symmetric representation O . The VAE is
 1473 then trained in an unsupervised way using inputs encoded to O from data events only. The VAE is
 1474 given no knowledge of the signal model during training. It is able to perform anomaly detection
 1475 through an encoder stage which does a lossy compression on the input to a lower-dimensional
 1476 latent space, and a decoder stage that samples from that latent space and generates an output of the
 1477 original dimensionality. By using the reconstruction error as a loss, this process enables the VAE
 1478 to develop a knowledge of the underlying data structure, thereby isolating new out-of-distribution
 1479 events by their high reconstruction error. This strategy is semi-supervised because the tool has
 1480 some knowledge of correct labels (eg. through the PFN latent space embedding) but is followed
 1481 by a data-driven unsupervised stage.

1482 Figure 7.15 provides a diagram of the ANTELOPE architecture.

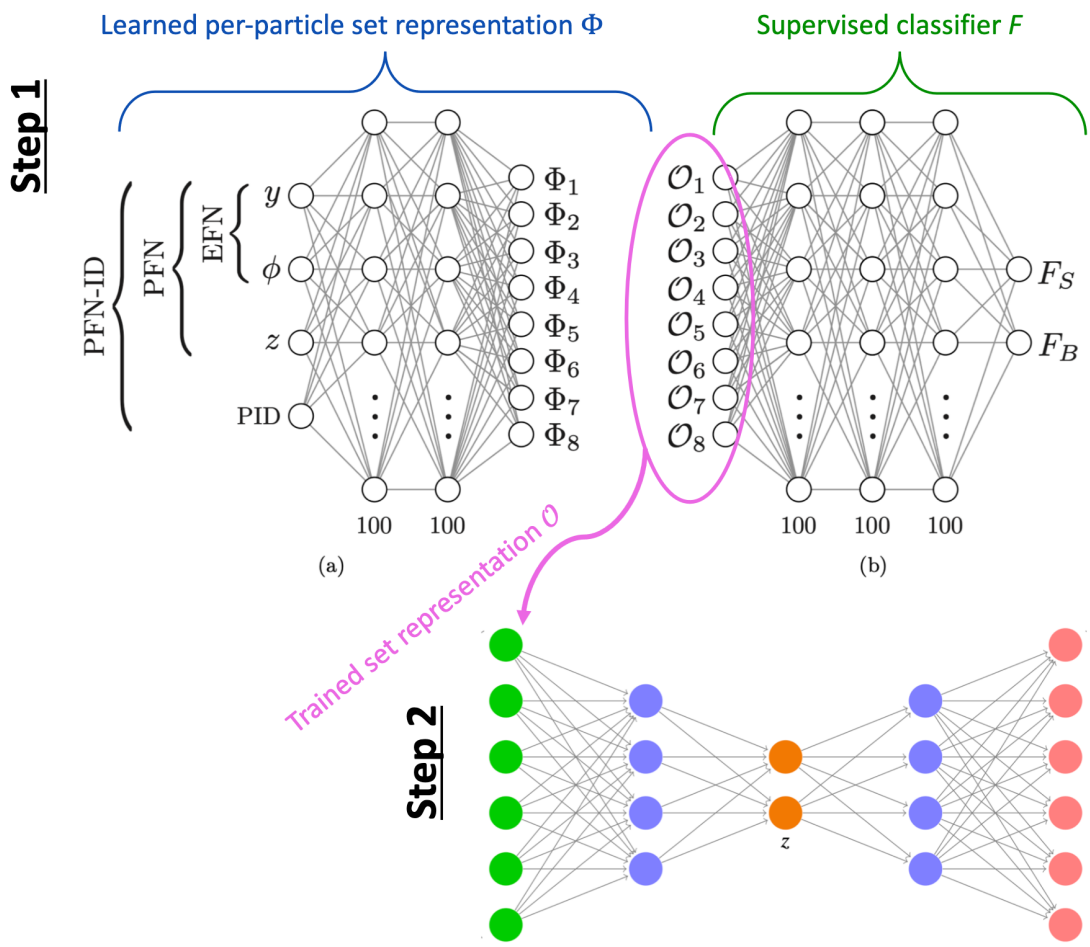


Figure 7.15: An annotated diagram of the ANTELOPE architecture.

1483 **Training**

1484 The VAE stage of the ANTELOPE network is trained directly over a subset of data events
1485 at preselection (6.7 million available, 500,000 used, with a 80% / 20% training/test split). The
1486 input dimensionality of the VAE has to match the encoded Φ dimension of the PFN, in this case
1487 64. The encoder has an encoding layer that brings the dimensionality to 32, and a final layer that
1488 compresses to the latent space dimension of 12. The network is trained for 50 epochs, with a
1489 learning rate of 0.00001. The loss \mathcal{L} is the sum of two terms, the mean-squared error (MSE) of
1490 input-output reconstruction, and the Kullback-Leibler divergence (KLD).

$$\mathcal{L} = \sum_i L_i = \sum_i |\Phi_i^2 - \Phi'_{\ell i}|^2 + \lambda D_{\text{KL}} \quad (7.2)$$

1491 As the PFN inputs are sufficiently normalized to remove any spurious information from train-
1492 ing, no additional normalization is applied to the PFN encoded inputs. The final ANTELOPE score
1493 used in the analysis is produced by applying a log + sigmoid transformation function to the total
1494 evaluated loss \mathcal{L} .

Figure 7.16 shows the loss during training.

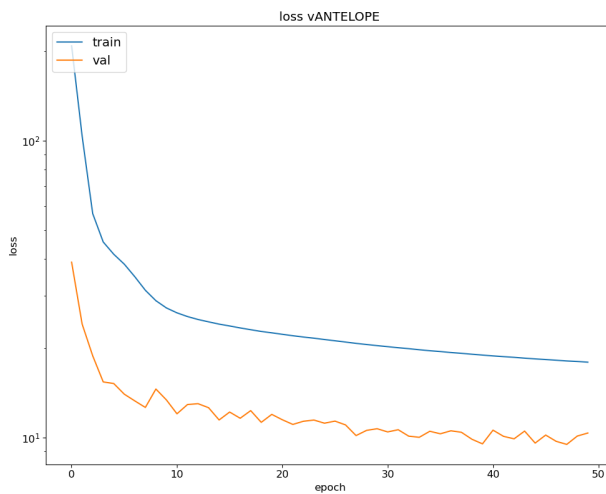


Figure 7.16: ANTELOPE architecture loss during training as a function of epoch.

1495

1496 **Performance**

1497 As with the PFN, the ANTELOPE performance is assessed via the area-under-curve (AUC) of
1498 the receiver operating characteristic (ROC) associated to evaluating the ANTELOPE on the test
1499 set of signal and background events. Figure 7.17 shows the output score distribution in data and
1500 total background MC, showing a very flat ratio and motivating the use of MC for studies of the
1501 ANTELOPE score.

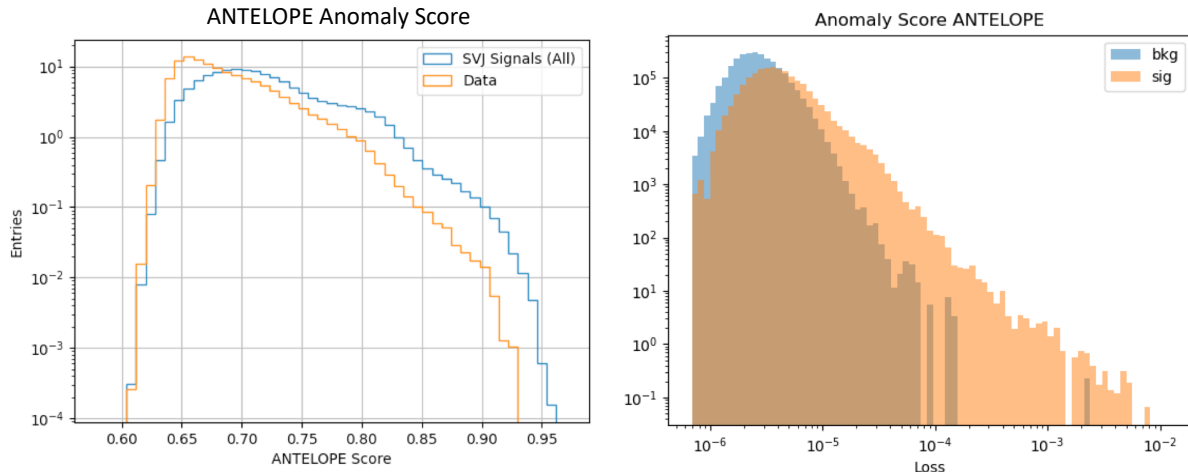


Figure 7.17: ANTELOPE score distribution comparing data and the total background MC (left), with good agreement observed between data and simulated background, and comparing all background MC to signals (right), revealing good discrimination power.

1502 Figure 7.18 shows the AUC of the ANTELOPE across the SVJ signal grid, demonstrating
1503 strong discrimination capability even in the varying corners of phase space. Compared to the
1504 supervised PFN method, the ANTELOPE is not as performant (as expected due to the absence of
1505 signal model in training). However, a selection on events with high ANTELOPE score nonetheless
1506 provides a 10-40% increase in signal significance by removing background and isolating the long
1507 tail of anomalous events.

1508 **Model Independence** The unsupervised component of training the ANTELOPE network is ex-
1509 pected to give it a more generalized sensitivity to new physics with E_T^{miss} and jet activity, beyond
1510 the scope of the SVJ grid. To assess this, alternative signal models are evaluated with the trained

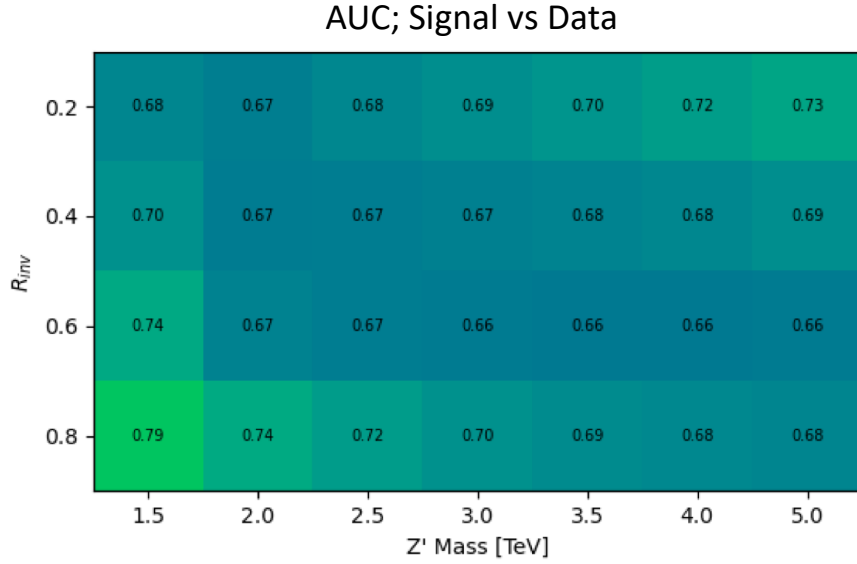


Figure 7.18: AUC from the ANTELOPE score for each signal in the SVJ grid.

1511 ANTELOPE network, as optimized for the SVJ grid, and their sensitivity in the analysis selection
 1512 is evaluated.

1513 The following alternate signal models were considered:

- 1514 • $Z' \rightarrow t\bar{t}$
- 1515 • $W' \rightarrow WZ$
- 1516 • Gluino pair production \rightarrow R-hadron + LSP (E_T^{miss}) with gluino masses 2000/3000 GeV, LSP
 1517 mass 100 GeV, and lifetime 0.03 ns (LSP = *lightest supersymmetric particle*)
- 1518 • Emerging jets s-channel with mass 1000 GeV and lifetime 1ns

1519 Figure 7.19 shows the distribution of these signals in the PFN score and the ANTELOPE score.
 1520 This comparison reveals that ANTELOPE is sensitive to E_T^{miss} in the event; it classifies signals
 1521 with no real E_T^{miss} , like the all-hadronic Z' and W' decays (given our imposed lepton veto) as
 1522 data-like, but the distributions for signals with E_T^{miss} such as SVJs, R-hadrons, and emerging jets
 1523 have distributions with higher anomaly score tails.

1524 Figure 7.20 shows a comparison of the sensitivity of the PFN and ANTELOPE regions across
 1525 a variety of signals, including the combined SVJ signal used to train the PFN. The benefit of the

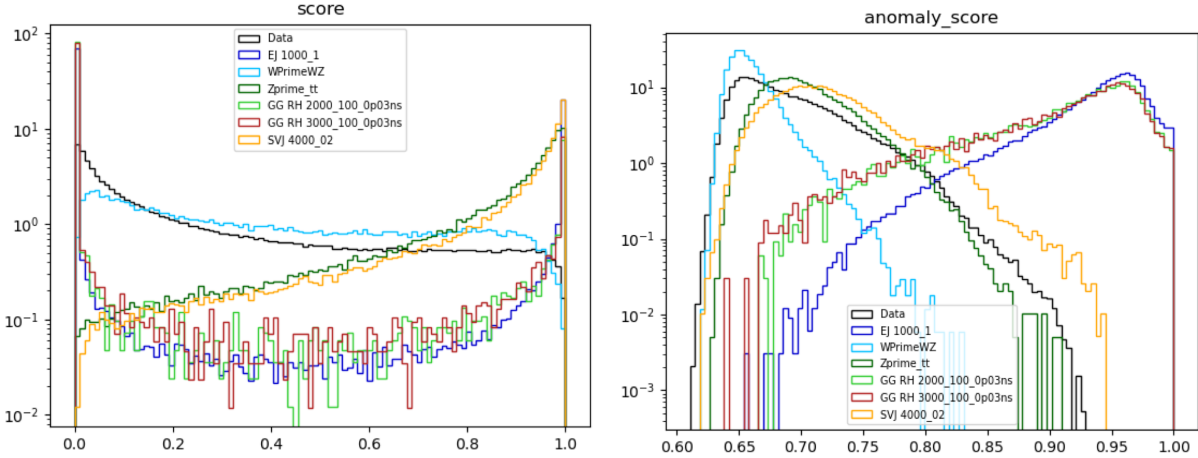


Figure 7.19: Comparing data and the alternate signal models for the PFN score (left) and ANTELOPE score (right). The emerging jet signal is an example of the gain of the model-independent ANTELOPE approach, where it has a bimodal shape in PFN score but is clearly tagged as anomalous by ANTELOPE.

1526 unsupervised stage of ANTELOPE in enhancing model independence is clearly seen through the
 1527 boost in performance for other signal models, namely the gluino and emerging jet signals, which
 1528 have more E_T^{miss} than the W' and Z' signals (all-hadronic) that were also tested. As commented
 1529 above, the PFN outperforms ANTELOPE as expected, because it was designed explicitly for the
 1530 task of classifying SVJs from background, demonstrating the power of supervised learning for the
 1531 model-specific approach.

$\text{sig eff} / \sqrt{\text{bkg eff}}$ for respective score cut (0.6 PFN, 0.7 ANTELOPE)

	EJ 1000	WprimeWZ	Zprime tt	GG RH 2000	GG RH 3000	SVJ
PFN	0.57	0.65	1.92	0.30	0.32	1.97
ANTELOPE	1.73	0.07	0.84	1.72	1.72	1.13

Figure 7.20: Comparing data and the alternate signal models in terms of sensitivity (S/\sqrt{B}) for the PFN and ANTELOPE tools, applying the selection that is used in the analysis. The ANTELOPE network is found to provide significant added sensitivity to alternate signals such as the gluino→R-hadron and emerging jets, which have higher E_T^{miss} than the SVJs.

1532 Studies on the ANTELOPE architecture and comparisons to other methods can be found in
 1533 Appendix B.1.

1534

1535

Chapter 8: Analysis Strategy

1536 This chapter will present the strategies used to isolate ATLAS data events most consistent with
1537 the SVJ model and to estimate the relevant background. The data and MC samples discussed in
1538 Chapter 6 are studied to create the analysis strategy, and the ML scores discussed in Chapter 7
1539 are used to isolate the most signal like events. A *preselection* selects events consistent with the
1540 SVJ topology based on basic features of the jets and E_T^{miss} . Preselected events are then split into
1541 a *control region* (CR), *validation region* (VR), and *signal region* (SR). The CR is used to estimate
1542 the estimate the background and the VR is used to validate that estimation. The SR is blinded
1543 during the development of the analysis strategy, and only unblinded to make the final measurements
1544 presented in Chapter 9. The final result is a polynomial fit of the *transverse mass* (m_T) spectrum
1545 in the SR. The preselection, region definitions, and polynomial fit will be discussed in detail in the
1546 following sections.

1547 **8.1 Preselection**

1548 The preselection isolates the phase space of events that most closely match the SVJ signal
1549 topology. Each cut was determined to reduced the background and enhance signal sensitivity. The
1550 list of preselection cuts and the motivation behind each cut are as follows. Here “jets” refer to
1551 anti- k_t R=0.4 jets, as discussed in Chapter 5.

- 1552 • At least 2 jets; in order to reconstruct the resonance mass
1553 • Leading jet $p_T > 450$ GeV; to ensure the use of the trigger in its efficiency plateau
1554 • Subleading jet $p_T > 150$ GeV; to mitigate the presence of non-collision background (Ap-
1555 pendix B.6.1)

- 1556 • $|\eta_{j1,j2}| < 2.1$; to ensure jets are fully within the tracker
- 1557 • $\Delta Y < 2.8$ (difference in rapidity between the two leading jets); to ensure central production
1558 associated to hard scatter
- 1559 • $E_T^{\text{miss}} > 200 \text{ GeV}$; to focus phase space on events with dark particles
- 1560 • $m_T > 1.2 \text{ TeV}$, to ensure a smoothly falling m_T distribution for fitting (Section 8.4)
- 1561 • At least 3 tracks for each of the two leading jets; to ensure good modeling
- 1562 • $\Delta\Phi(j_1, j_2) > 0.8$; to mitigate the presence of non-collision background (Appendix B.6.1).

A cutflow showing the impact of these cuts in data and signal is shown in Figure 8.1.

Data			Signals - All		
Cut	Statistics	Rel. Efficiency	Cut	Statistics	Rel. Efficiency
Initial	1.71E+10		Init	6.66E+05	
Trigger	3.45E+08	0.0202	Trigger	2.83E+05	0.4245
N. jets ≥ 2	2.84E+08	0.8233	N. jets ≥ 2	2.80E+05	0.9896
Leading Jet Pt $> 450 \text{ GeV}$	1.49E+08	0.5235	Leading Jet Pt $> 450 \text{ GeV}$	2.21E+05	0.7900
Lead Jet Eta < 2.1	1.42E+08	0.9528	Lead Jet Eta < 2.1	2.19E+05	0.9922
Subleading Jet Eta < 2.1	1.33E+08	0.9432	Subleading Jet Eta < 2.1	2.12E+05	0.9661
$dY < 2.8$	1.29E+08	0.9628	$dY < 2.8$	2.11E+05	0.9934
MET > 200	7.07E+05	0.0055	MET > 200	1.13E+05	0.5370
$mT > 1200$	5.38E+05	0.7613	$mT > 1200$	7.94E+04	0.7019
Jet2 pT > 150	5.03E+05	0.9343	Jet2 pT > 150	6.14E+04	0.7739
$d\Phi(j_1, j_2) > 0.8$	4.97E+05	0.9890	$d\Phi(j_1, j_2) > 0.8$	5.83E+04	0.9494

Figure 8.1: Preselection cutflow for data (left) and signal (right).

1563

1564 With the exception of the cuts necessary to reduce the non-collision background, all cuts were
1565 verified to enhance signal sensitivity by improving s/\sqrt{b} , a standard estimate of discovery sensi-
1566 tivity, where s is the number of signal events and b is the number of background events. The cuts
1567 on ΔY and E_T^{miss} were optimized to enhance s/\sqrt{b} , and the other cuts were informed by the physics
1568 motivations provided above.

1569 Vетос are applied to reject any events where an error for a subdetector is flagged. This covers
1570 Tile/LAr calorimeter errors, single event upsets in the SCT, and incomplete events. To reject non-
1571 collision backgrounds (NCB), such as calorimeter noise, beam halo interactions, or cosmic rays,

1572 the standard ATLAS event cleaning procedure is applied. As this analysis is very dependent on
1573 E_T^{miss} associated to jets, the TIGHT event cleaning working point is applied. Tight cleaning requires
1574 jets to pass a stricter set of quality requirements compare to the LOOSE cleaning option. Due to
1575 the alignment between jets and E_T^{miss} in this phase space, it was found that two additional cuts
1576 (indicated above) are needed to remove NCB. The process for selecting these cuts is presented in
1577 Appendix B.6.1.

1578 The two leading in p_T jets in the event are considered as the dark quark candidates. This choice
1579 was determined by truth studies matching the dark quark to reconstructed jets in simulation, which
1580 indicate that the leading p_T assignment allows for high accuracy in ΔR matching to dark quarks.
1581 These studies can be found in Appendix C.

1582 Figure 8.2 and Figure 8.3 show the distribution of signal and background MC in several key
1583 analysis variables after preselection is applied.

1584 **8.2 SVJ Fit and Discovery Analysis Strategies**

1585 As was introduced in Chapter 7 this analysis is interested in achieving dual goals: to make
1586 the best possible measurement of the SVJ signal model generated for this analysis, and to broadly
1587 search for any signals consistent with dark QCD behavior and inconsistent with a Standard-Model-
1588 only background hypothesis. To this end, two parallel analysis strategies are developed.

1589 The SVJ Fit strategy uses the supervised PFN ML score in defining the signal region. Recall,
1590 the PFN is trained over simulated MC background and a combination of all MC SVJ signals. This
1591 gives this ML tool high sensitivity to the particular nuances of the SVJ shower predicted by the
1592 modeled theory. In addition to using the supervised ML tool, the SVJ Fit analysis strategy sets
1593 limits on the expected cross-section of each signal point in the SVJ signal grid. To achieve this, the
1594 shape of the SVJ signals are considered in the final fit, as will be elaborated on Section 8.5.1. The
1595 combination of the supervised PFN ML score and the signal-shape sensitive fitting strategy allows
1596 for the greatest possible sensitivity to the modeled signal process, thus allowing the analysis the
1597 best chance at discovery of this model, or enabling the analysis to set the best possible limits on

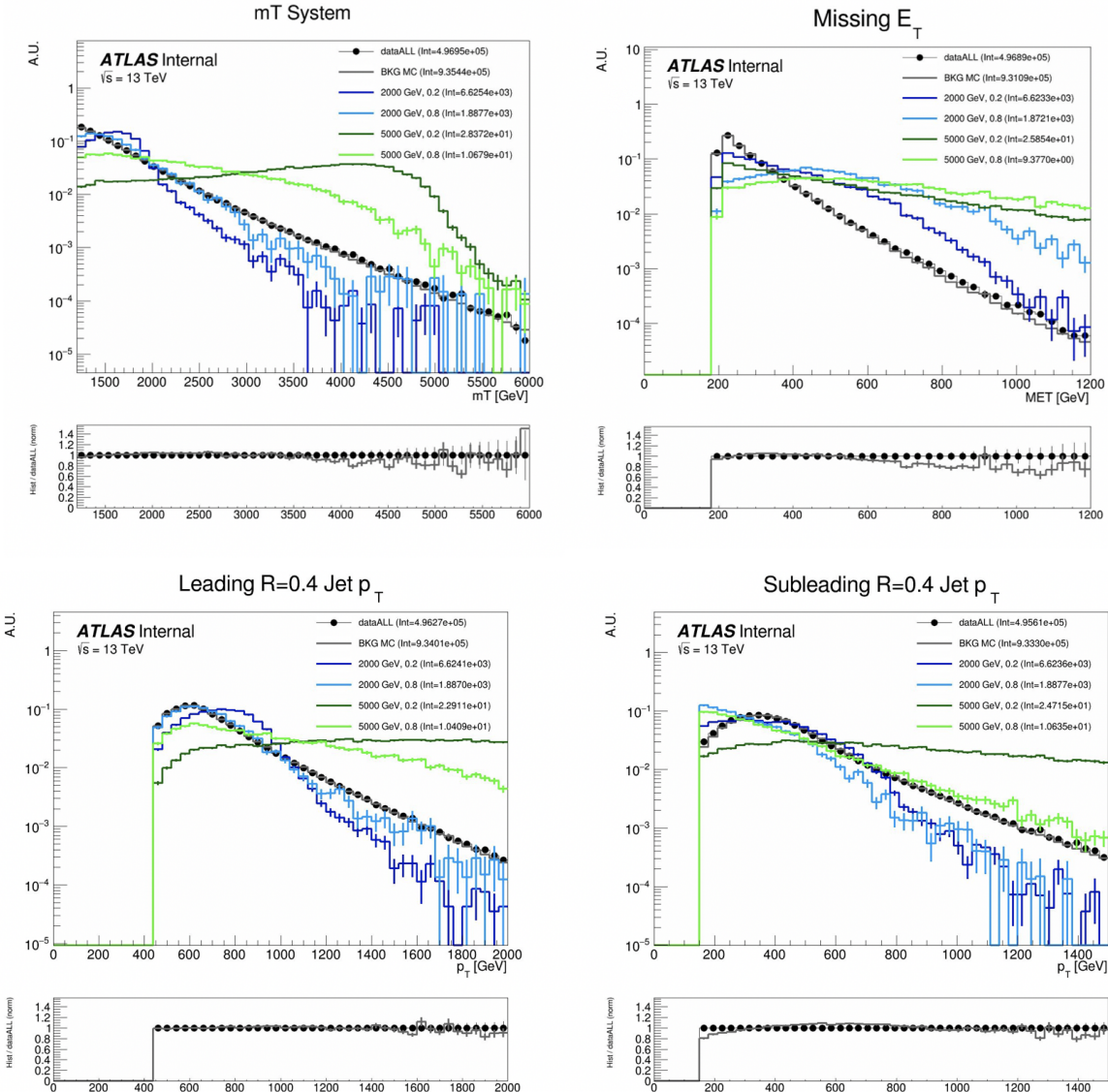


Figure 8.2: Energy and momentum analysis variables at preselection, for data, all background MC and representative signal models. m_T is the key fit variable, and this plot illustrates the smoothly falling background in comparison to the resonant shape of the signals. m_T is further illustrated in Figure 8.9.

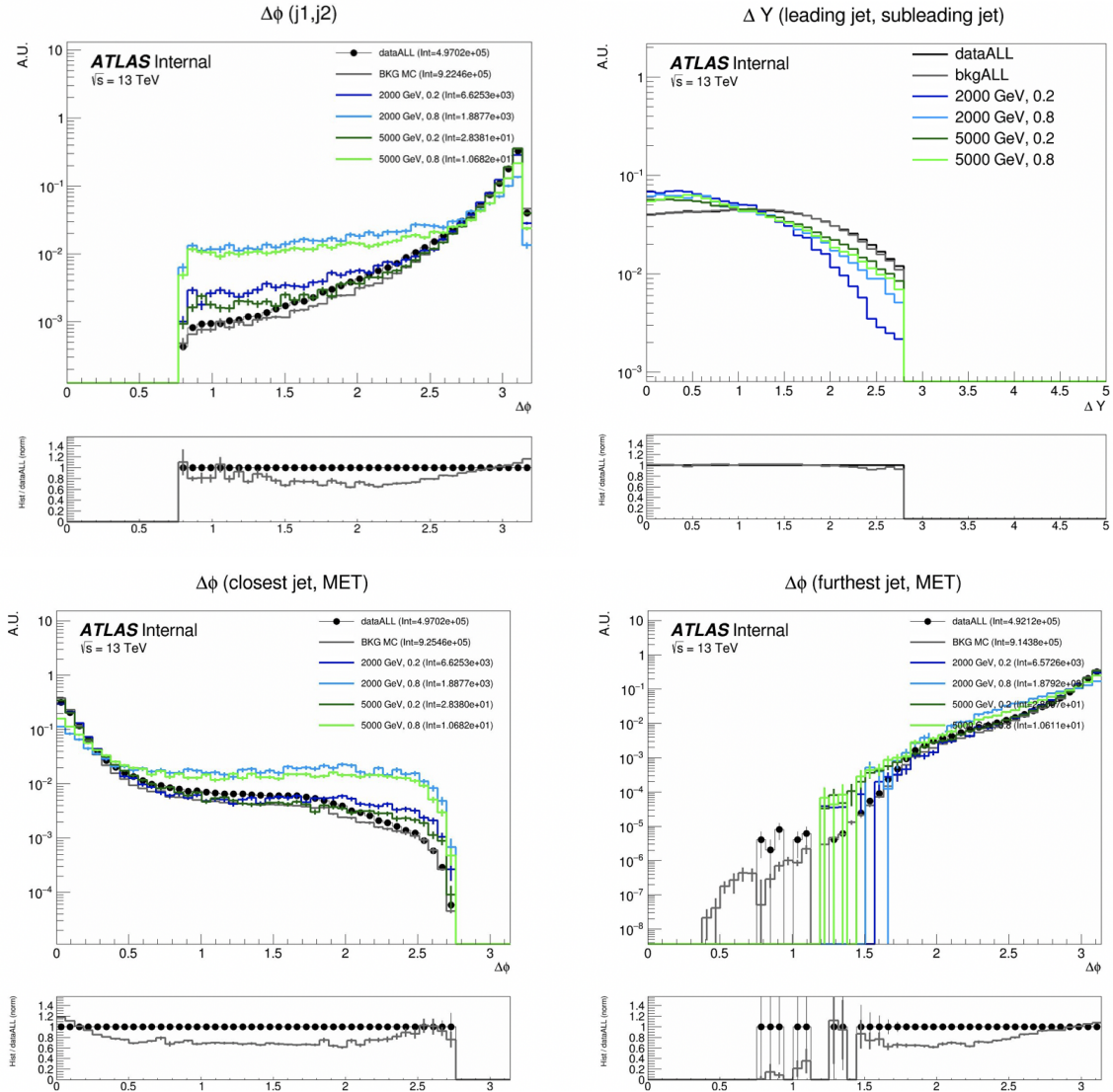


Figure 8.3: Orientation analysis variables at preselection, for data, all background MC and representative signal models. While $\Delta\phi(E_T^{\text{miss}}, j)$ variables are not used explicitly in the analysis flow, they help create a picture of the event.

1598 the observed cross-section.

1599 In contrast, the Discovery analysis strategy attempts to design a more general search, which
1600 could be sensitive to SVJs, but also to other possible hidden valley dark QCD models, such as
1601 fully dark jets or emerging jets [21]. The Discovery analysis strategy uses the semi-supervised
1602 ANTELOPE ML score in defining the signal region. Recall, the ANTELOPE is trained over AT-
1603 LAS data only, with no explicit knowledge of the SVJ signal behavior. The Discovery fit strategy
1604 is also signal model agnostic, by employing a bump hunt [74] strategy, which searches a smoothly
1605 falling template for any bumps inconsistent with a background only hypothesis. Therefore any
1606 signal which could present a resonant signature in m_T could show up as an excess in this strategy.

1607 The details of both strategies will be explored in the follow sections which detail the design
1608 of the signal regions and fit strategies. A diagram demonstrating the analysis flows can be seen in
Figure 8.4. Details on each selection and region can be found in the following subsections.

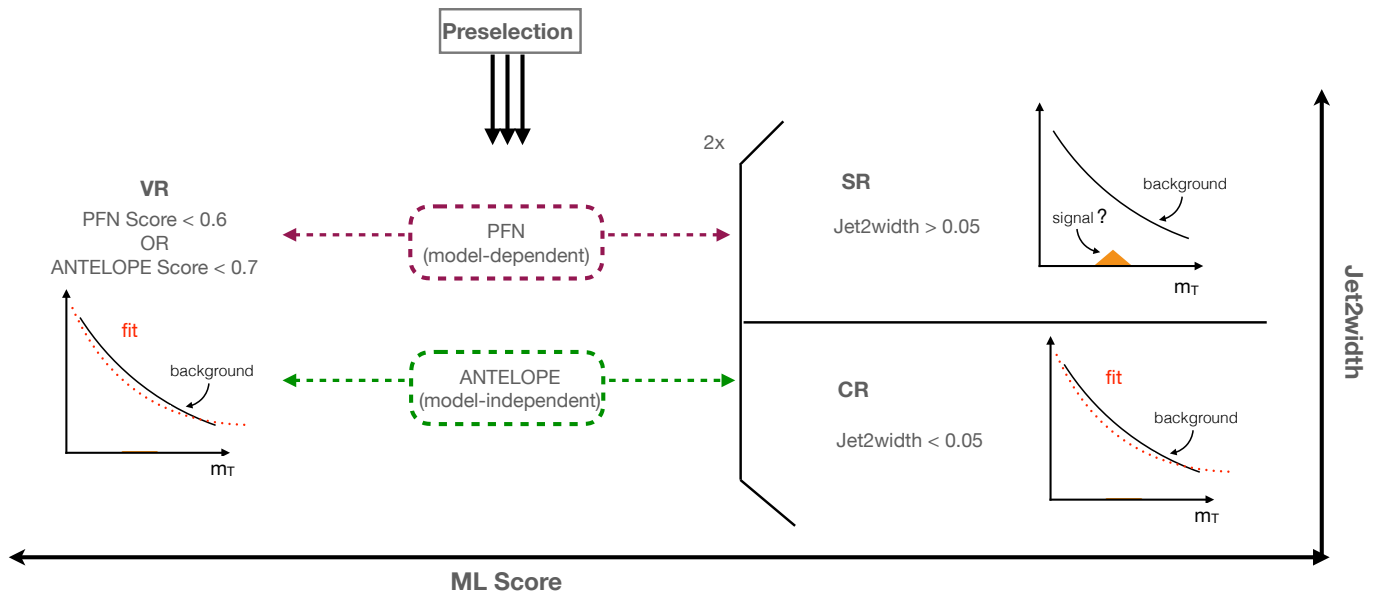


Figure 8.4: Flow of analysis selections, regions, and background estimation/validation fitting strat-
egy. TODO: diagram needs to be corrected

1609

1610 **8.3 Analysis Regions**

1611 **8.3.1 Control and Validation Regions**

1612 The final background estimation will come from a polynomial fit to the m_T distribution in the
1613 signal region. The control and validation regions are needed to develop and test this fit in data.

1614 To define the CR selection, a variable is needed that isolates background from all signals across
1615 the (R_{inv}, m_Z) grid, which is challenging due to the varying nature of the signal models in quantities
1616 such as E_T^{miss} and p_T balance, as illustrated in Figure 8.2. The variable *jet width* is chosen, which
1617 is the calorimeter measurement of the width of a small-R jet as defined by the distance between
1618 the cluster and the jet axis scaled by the jet energy [75]. Figure 8.5 shows this variable specifically
1619 for the subleading jet width, in data, background MC and signal at preselection. The leading jet
1620 width, which was determined to be less useful for isolating signal from background is also shown.
1621 The subleading jet is more likely to be the jet aligned with MET, which is why the signal jet width
1622 is consistently wider in the subleading jet, but not the leading jet. A selection of $\text{width}_{j2} < 0.05$ is
1623 chosen for the CR, with the VR and SR therefore having a selection of $\text{width}_{j2} \geq 0.05$.

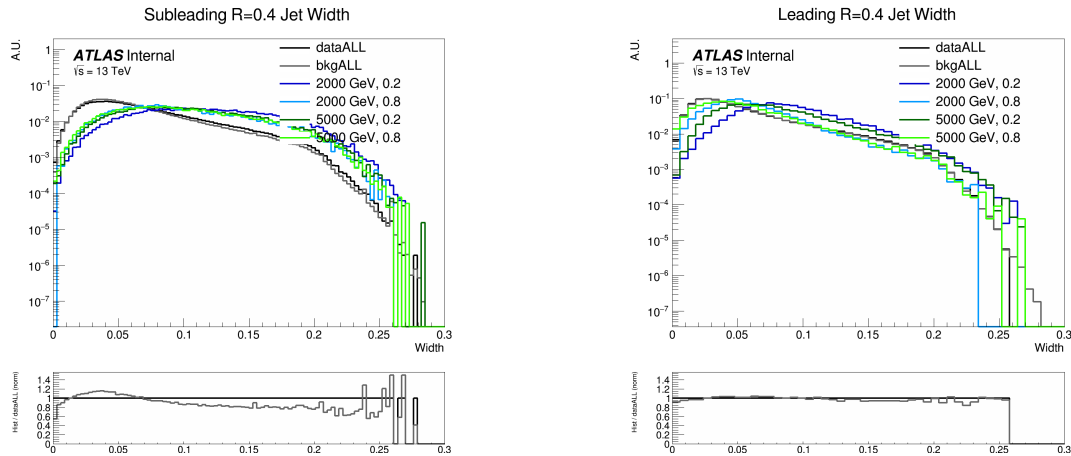


Figure 8.5: Distributions of the subleading jet width width_{j2} (left) and leading jet width width_{j1} (right) in data, background MC and signals at preselection. All SVJ signals are seen to be wider than the background in width_{j2} . The same is not true for width_{j1} , where some signals are observed to closely match the background.

1624 While the CR was used to develop the polynomial strategy, and is the primary region used in

many of the fit studies, a validation region is used as an additional check of the estimation strategy
 in data. The VR is defined using the region of events with low ML score by either the PFN or
 ANTELOPE networks. Here the analysis strategy splits into the two parallel strategies presented
 in Section 8.2: the SVJ fit strategy and the Discovery strategy. A selection of [PFN score ≤ 0.6
 & $\text{width}_{j2} \geq 0.05$] defines the SVJ Fit VR, while [ANTELOPE score ≤ 0.7 & $\text{width}_{j2} \geq 0.05$]
 defines the discovery VR.

There are therefore three variables that are crucial to the analysis strategy: width_{j2} , ML score,
 and m_T . Figure 8.6 shows the correlations of all three variables to one another. Any outstanding
 correlations are shown in Figure 8.7 to not sculpt the m_T distribution and only affect its slope,
 making these variables trustworthy for extrapolation across background/signal regions and final
 fitting procedures.

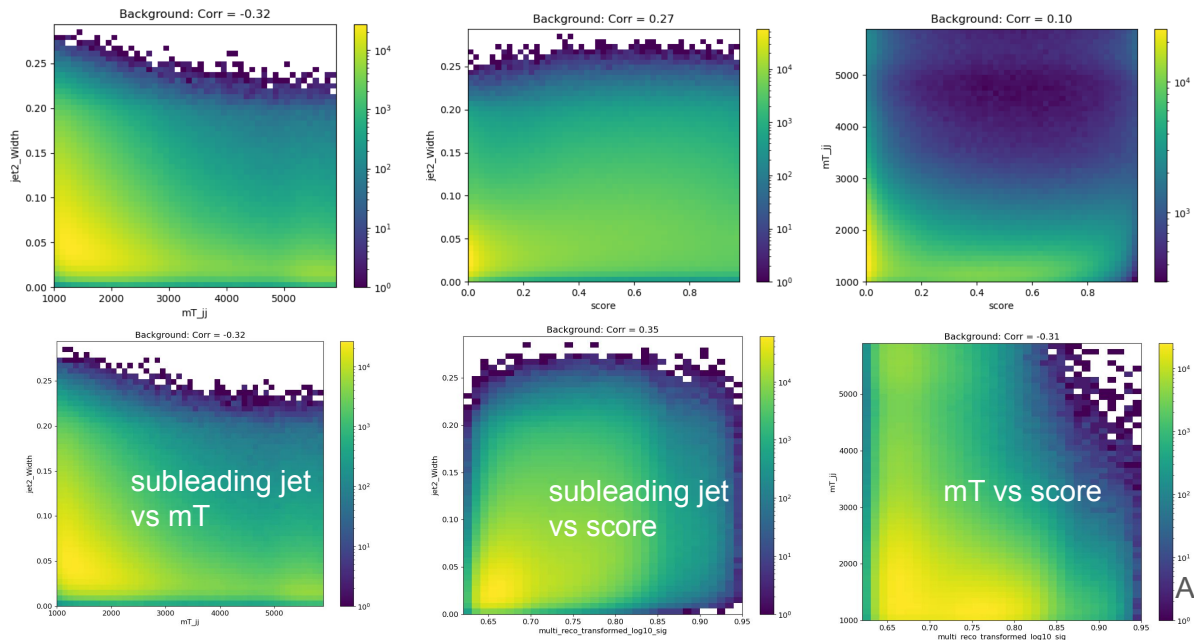


Figure 8.6: 2D plots revealing correlations between width_{j2} and m_T (left), width_{j2} and ML score (middle), and m_T with ML score (right). For the top row, the ML score is the PFN score, and for the bottom three, the ML score is the ANTELOPE score. Minimal correlations are observed and are shown to not sculpt m_T , validating these variables for analysis region construction and statistical treatment.

The most important variable for shape robustness across the CR, VR, and SR is m_T , as this
 is the variable that is fit for the statistical results. Figure 8.7 shows the distribution of m_T across

1638 the CR, VR, and SR, for both the PFN (supervised) and ANTELOPE (semi-supervised) strategies.
 1639 Some slope is observed in the ratio of the CR to the VR/SR shapes; however, the chosen back-
 1640 ground estimation strategy of polynomial fitting is expected to accommodate this slope. Further,
 1641 the ability of the background polynomial to fit both tail shapes will flex the fit framework in a
 1642 way that will generate higher confidence in the final ability to fit the SR. No significant bumps or
 sculpting are observed.

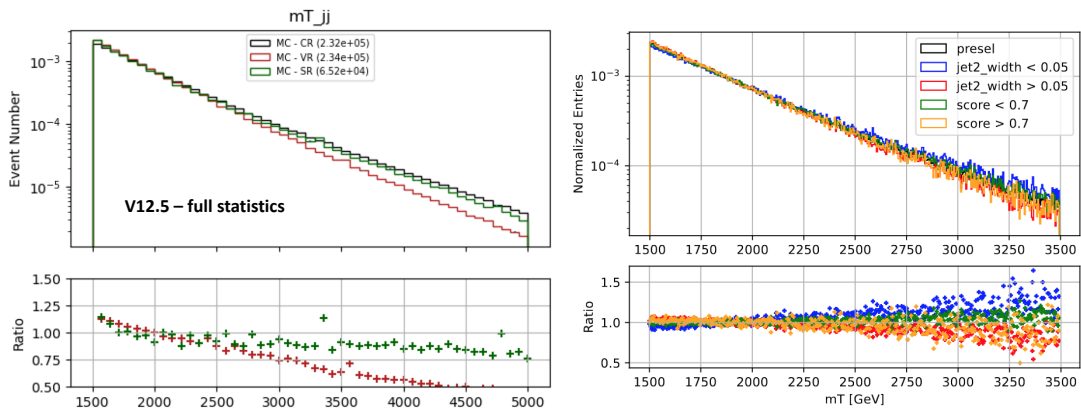


Figure 8.7: m_T in simulation across the CR, VR, and SR for both PFN (left) and ANTELOPE (right) selections.

1643

1644 8.3.2 Signal Region

1645 A selection of PFN score > 0.6 in the SVJ Fit region and ANTELOPE score > 0.7 in the
 1646 Discovery region is made to provide the primary signal-to-background enrichment, as motivated
 1647 by Section 7.1.1. These values are determined to maximize s/\sqrt{b} in each region. The additional
 1648 selection of $\text{width}_{j2} \geq 0.05$ orthogonalizes the SR to the CR. Note that the PFN and ANTELOPE
 1649 regions are not orthogonal; this is because the two analysis flows serve different purposes, their
 1650 statistical treatments are different, and they will not be combined.

1651 A summary of the SR, CR, and VR definitions can be seen in Figure 8.8, along with the relative
 1652 data statistics in each region.

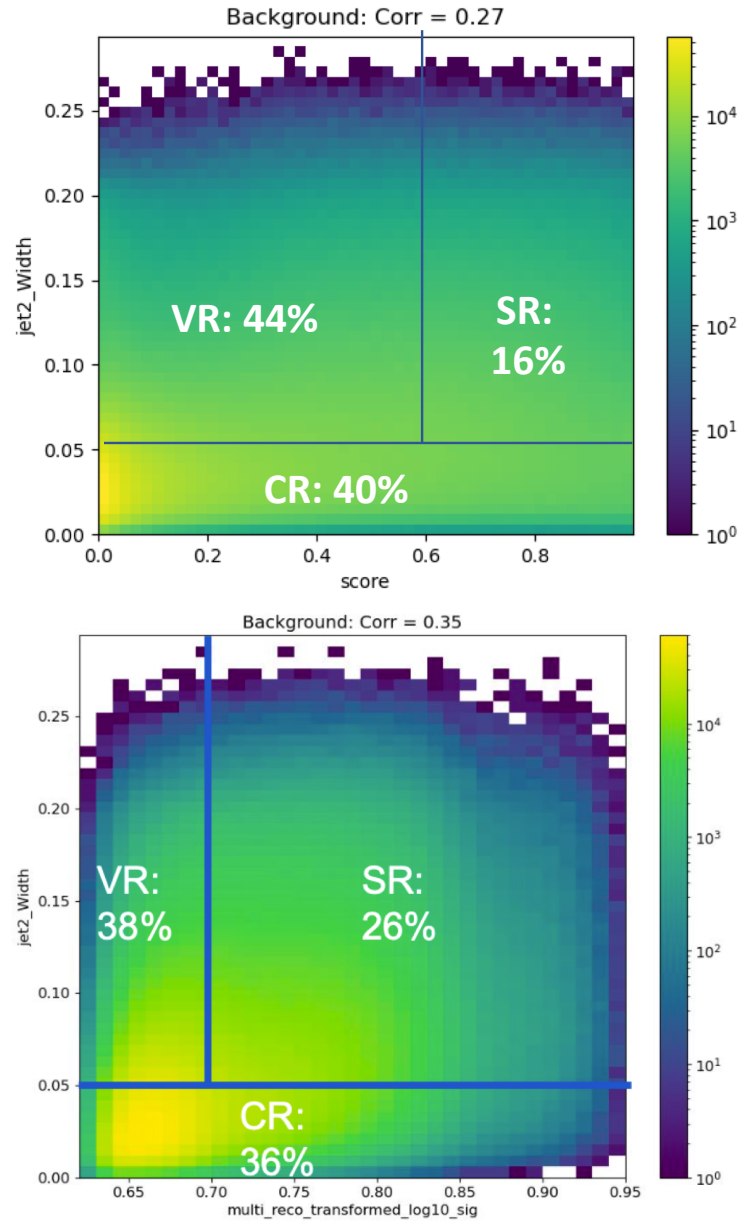


Figure 8.8: Definition of CR, VR, and SR regions using width_{j2} and the ML score, along with the population of each region in data statistics. The SVJ Fit region is shown on top with the PFN score on the x-axis, and Discovery region is shown on the bottom, with the ANTELOPE score on the x-axis.

1653 8.4 Background Estimation

1654 The transverse mass m_T is chosen as the search variable due to the potential for the SVJ signal
 1655 to create a resonant shape around the mass of the Z' . m_T is the total transverse mass of the two
 1656 leading jets and the E_T^{miss} , expressed in Equation 8.1 as:

$$m_T^2 = [E_{T,jj} + E_T^{\text{miss}}]^2 - [\vec{p}_{T,jj} + \vec{p}_T^{\text{miss}}]^2 \quad (8.1)$$

1657 where $E_{T,jj}$ is the transverse energy of the dijet system. We take $E_{T,jj} = m_{jj}^2 + |\vec{p}_{T,jj}|^2$, where
 1658 m_{jj}^2 is the invariant mass of the two leading jets, and $\vec{p}_{T,jj}$ is the vector sum of the p_T of the two
 1659 leading jets. m_T is selected as the search variable in place of simpler invariant mass m_{jj} because
 1660 substantial energy from the Z' decay is captured in the E_T^{miss} . Therefore incorporating E_T^{miss} into
 1661 m_T improves the resonance around the mass of the Z' .

Figure 8.9 illustrates the resonance in m_T of the SVJ signals.

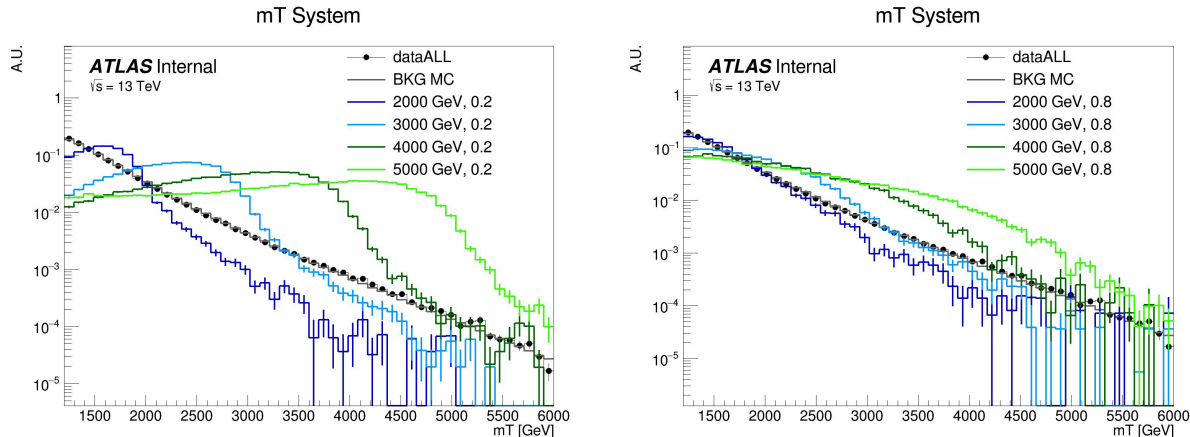


Figure 8.9: The resonant shape of the SVJ signals in m_T , in contrast to the smoothly falling m_T background. The high R_{inv} signals (right) boast a wider shape, making them more difficult to detect, while the low R_{inv} signals (left) produce a more narrow resonance in m_T .

1662
 1663 The SM background in the SR is predominantly composed of QCD events, and due to the poor
 1664 modeling of QCD at high energies by MC, it is estimated in a fully data-driven way. An empirical
 1665 functional form is used for the background shape of m_T . The ability of this function to model
 1666 the background behavior is tested both the CR and the VR for each analysis strategy. The shape

1667 parameters are left free in all the fits.

1668 The fits are performed for $1500 \text{ GeV} < m_T < 6000 \text{ GeV}$. The polynomial chosen is a standard

1669 5-parameter function used in several similar dijet search analyses such as [76] [77] [78] and shown

1670 in Equation 8.2:

$$f(x) = p_1(1 - x)^{p_2}x^{p_3+p_4\ln x+p_5\ln^2 x} \quad (8.2)$$

1671 Here $x = m_{jj}/\sqrt{s}$ and the p_i are free parameters. The fit function is required to be fully positive, and

1672 the m_T distribution is fit to 90 even-width bins. The resulting fit shape is used as the background

1673 estimation for both the SVJ Fit strategy and the Discovery strategy. Validation of the fit and its

1674 ability to both model the background and detect signal are shown in Section 8.5. Higher order

1675 polynomials were also considered, but an F-test was performed and the five parameter function

1676 was determined to be adequate and optimal for capturing the shape of the background.

1677 **8.5 Fit Strategy and Validation**

1678 The steps taken to validate the fitting approach for both the SVJ Fit strategy and the Discovery

1679 strategy will be outlined in the following sections. The signal region fits which compromise the

1680 final result will be presented in Chapter 9.,

1681 **8.5.1 SVJ Fit Strategy**

1682 The ability of the five parameter fit function to capture the shape of the background is studied

1683 extensively, using data from the CR and VR. Signal injection tests are performed to determine the

1684 ability of the fit to recover and quantify any SVJ signal excess. Finally, estimates of the expected

1685 sensitivity are made.

1686 **Background Only Fits**

1687 Three validations are used for the background fit polynomial: MC across all analysis regions,

1688 data in the CR and VR, and pseudo-data in the CR and VR.

1689 Figure 8.10 shows the ability of this polynomial to fit the smoothly falling m_T background in
 1690 simulation across all 3 analysis regions (CR, VR, SR). The m_T spectrum is fit in 90 even bins.
 1691 These distributions are obtained by downsampling the MC statistics to match the relevant statis-
 1692 tics of the data region, in accordance with the MC weights. The high background-only p -value
 indicates a good fit.

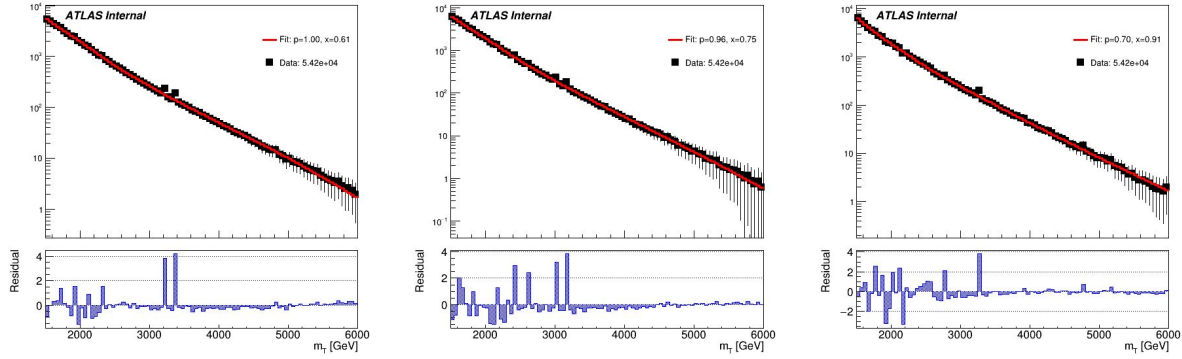


Figure 8.10: Background-only m_T fits using representative MC in the CR (left), VR (middle), and SR (right).

1693
 1694 A slight sinusoidal pattern in the residuals may be observed. This arises due to the “stitching”
 1695 of the p_T slices for the QCD MC (as shown in Figure 6.1), which is picked up by the fit. For this
 1696 reason, fitting to MC is only checked to verify that the differences in the slope of m_T between the
 1697 three regions (as shown in Figure 8.7) do not pose a problem for the fitting strategy.

1698 The nature of the functional fitting method allows it to easily adapt to changes in slope of a
 1699 smoothly falling distribution. Thus validation of the fit can be performed in data using the CR and
 1700 the VR distributions to model the expected behavior in the SR. Figure 8.11 shows the a successful
 1701 fit performed on the full statistics CR and VR regions.

1702 Figure 8.12 shows the post-fit values of the fit parameters and their uncertainties for each fit.

1703 To further validate the fit stability of the fit against potential statistical fluctuations, *pseudo-data*
 1704 (also known as *toy datasets*) are created from the CR data distribution. The pseudo-data is created
 1705 following an *Asimov* prescription [79], using a template to generate a set of toys representing
 1706 different possible statistical fluctuations. When studied as a group, the performance of the pseudo-
 1707 data collection represents the range of possible behavior for an unknown distribution (the SR data

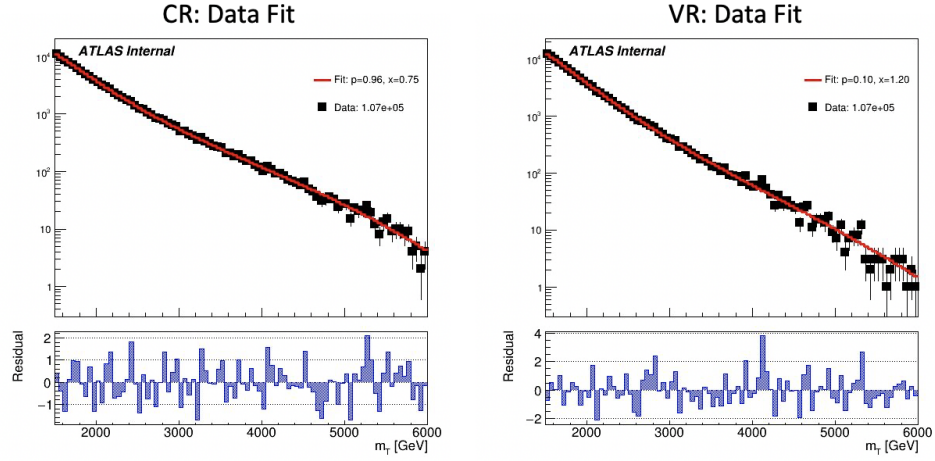


Figure 8.11: Background-only m_T fits using data in the full statistics CR and VR regions.

Parameter	CR		VR	
	Value	Error	Value	Error
p1	1.0716e+05	4.64e+02	1.0686e+05	4.63e+02
p2	4.2479e+01	2.97e+00	3.4279e+01	3.71e+00
p3	5.3888e+01	3.81e+00	4.0798e+01	4.50e+00
p4	2.3804e+01	1.47e+00	1.9424e+01	1.71e+00
p5	3.6683e+00	2.18e-01	3.1583e+00	2.51e-01

Figure 8.12: Post-fit parameters for the PFN CR and VR. p_1 can also be considered N_{bkg} or the normalization factor.

1708 in this case), given its statistical uncertainties.

1709 The template used to generate the pseudo-data is a *smoothed* and *scaled* version of the CR.

1710 The smoothing applied follows the procedure for functional decomposition described in Ref. [80].

Figure 8.13 shows the impact of smoothing on the source data distribution in the CR.

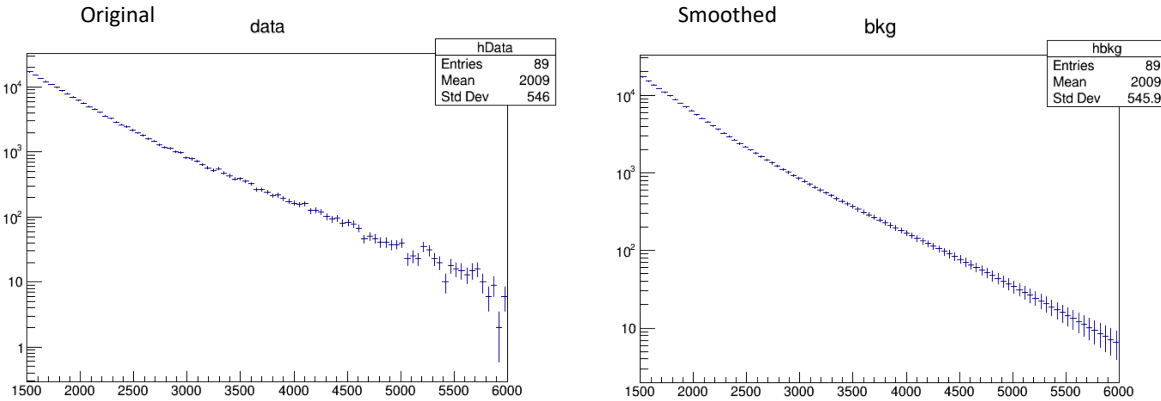


Figure 8.13: m_T distribution in the data CR, before (left) and after (right) smoothing.

1711

1712 The scaling adjusts the statistics of the smoothed template to the expected statistics of the SR.

1713 Recall Figure 8.8, which illustrates that the statistics of the CR and the VR are almost 3x the

1714 expected statistics of the SR. The polynomial fitting strategy is sensitive to the statistics of the

1715 fitted template, so its performance can very substantially depending on the statistical power of the

1716 fitted distribution. To mitigate this, the smoothed template is scaled to the expected statistics of

1717 the SR. Toys are then generated from the smoothed distribution, by varying each bin within its

1718 statistical uncertainty according to a Poisson distribution. Each toy has the same statistical power

1719 as the SR, within statistical uncertainty.

1720 Figure 8.14 shows example fits to three such toy datasets. Figure 8.15 shows the resulting

1721 p-values after an ensemble of 100 Asimov pseudo-datasets are each individually fit. This test

1722 determines the likelihood of exceptionally good (high p-value) or poor (low p-value) fits due to

1723 randoms statistical fluctuations in the data. A flat distribution is observed, indicating good statisti-

1724 cal behavior.

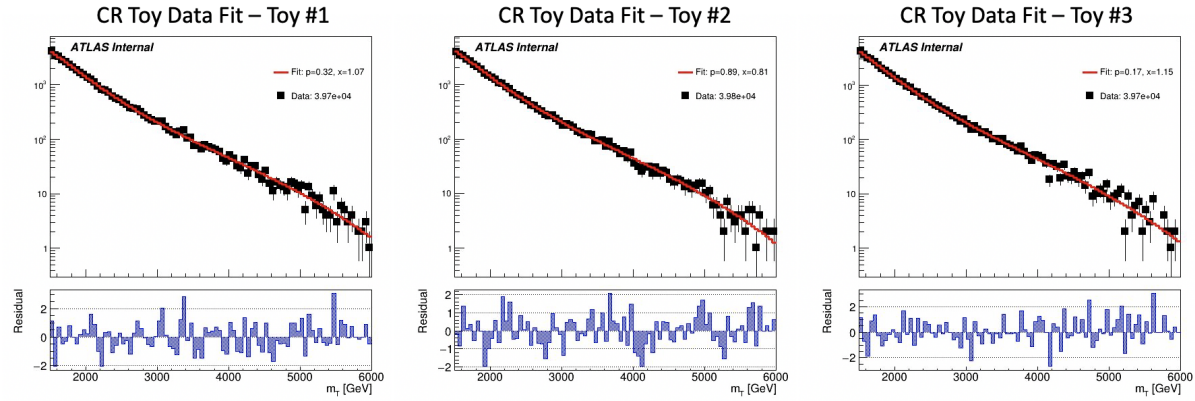


Figure 8.14: Background-only m_T fits using pseudo-data from the CR template.

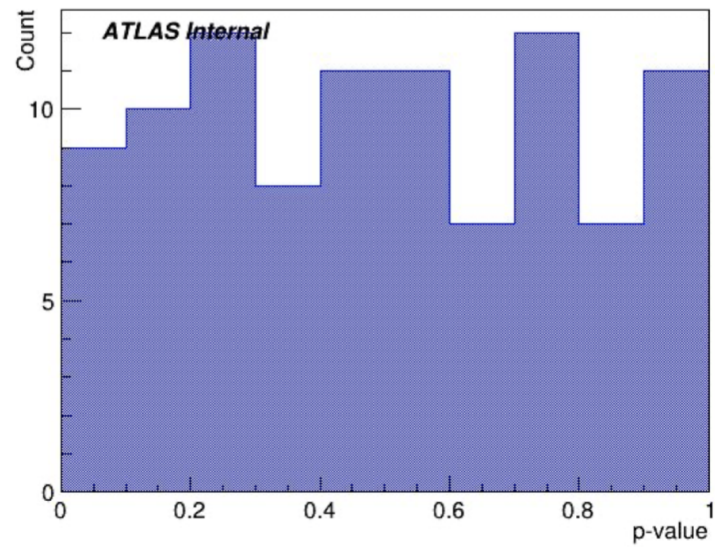


Figure 8.15: p -value histograms from 100 fits to Asimov data in the CR.

1725 **Signal + Background Fits**

1726 Figure 8.16 shows an example of an injected signal into the exclusion region m_T spectrum, and
the ability of the fit framework to accurately fit the number of signal events. TODO: updated fit

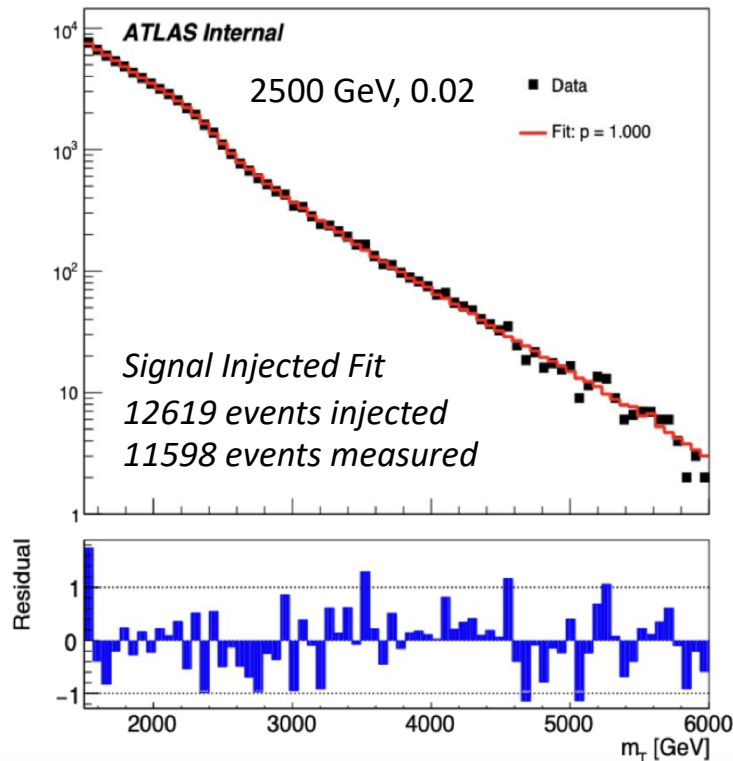


Figure 8.16: Example S+B fits on a background m_T spectrum with injected signal from the point (2500 GeV, $R_{inv}=0.2$).

1727
1728 Signal injection tests demonstrate the a linear relationship between the amount of signal in-
1729 jected and the amount of signal measured by the fit. The signal injection tests are performed in
1730 Asimov datasets to counter the impact of statistical fluctuations in any given template. 50 Asimov
1731 trials are run for all signal points across Z' mass and R_{inv} .

1732 Figure 8.17 provides the results of these tests. The uncertainty of the measurement varies
1733 according to the Z' mass, due to the larger relative background for lower mass points. However,
1734 a strong linear relationship between amount of signal injected and amount of signal measured is
1735 observed for all signal points, which is the key feature.

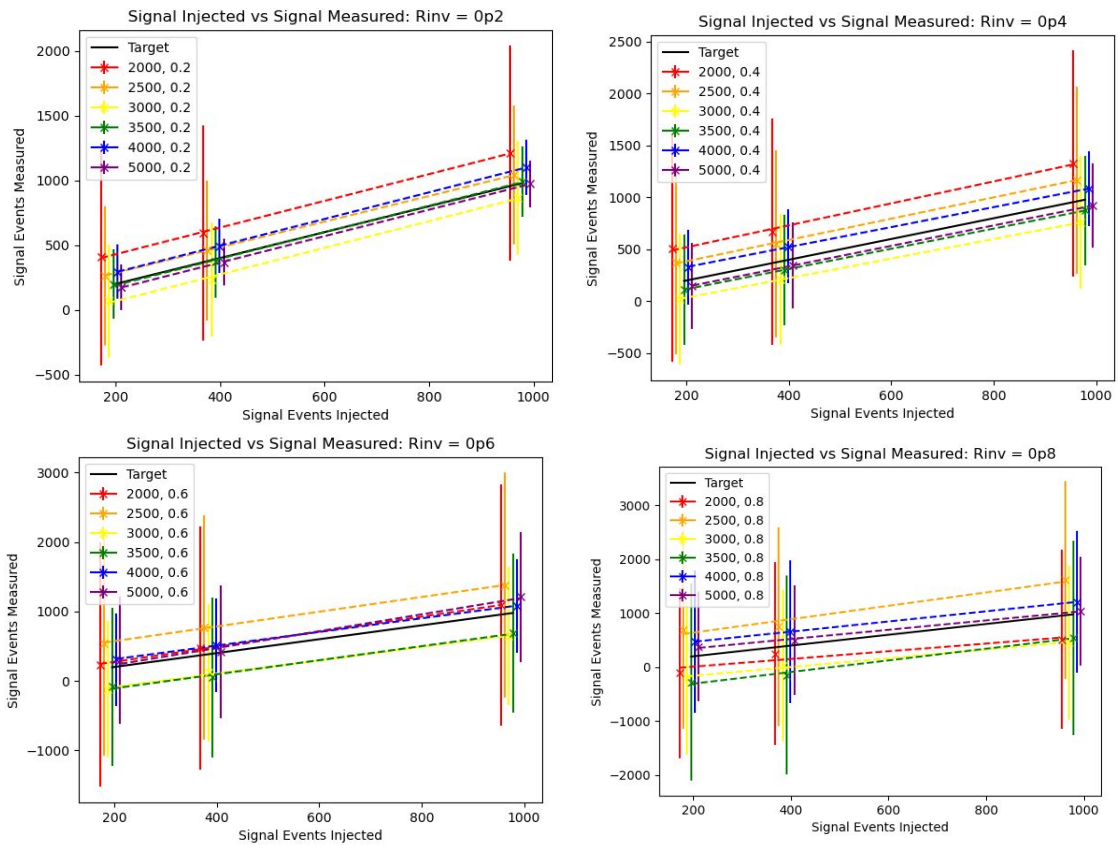


Figure 8.17: Measured signal at a variety of injected values ($1x$, $2x$, and $5x\sqrt{b}$), for all signal points in the grid, $R_{inv}=0.2$ (top left), 0.4 (top right), 0.6 (bottom left), and 0.8 (bottom right).

1736 **Expected Sensitivity**

1737 Limits on the signal process are obtained by determining the cross section of the signal that can
1738 be excluded to 95% confidence. Figure 8.18 shows the expected limits obtained from an average
1739 of Asimov data fits. The limits shown do not include systematics uncertainties in the fit, which
1740 will be discussed in Section ??.

1741 Considerable exclusion power is predicted for low R_{inv} signal points, with the higher R_{inv} points
1742 presenting more difficulty due to the very broad signal bump. TODO: update limit plots

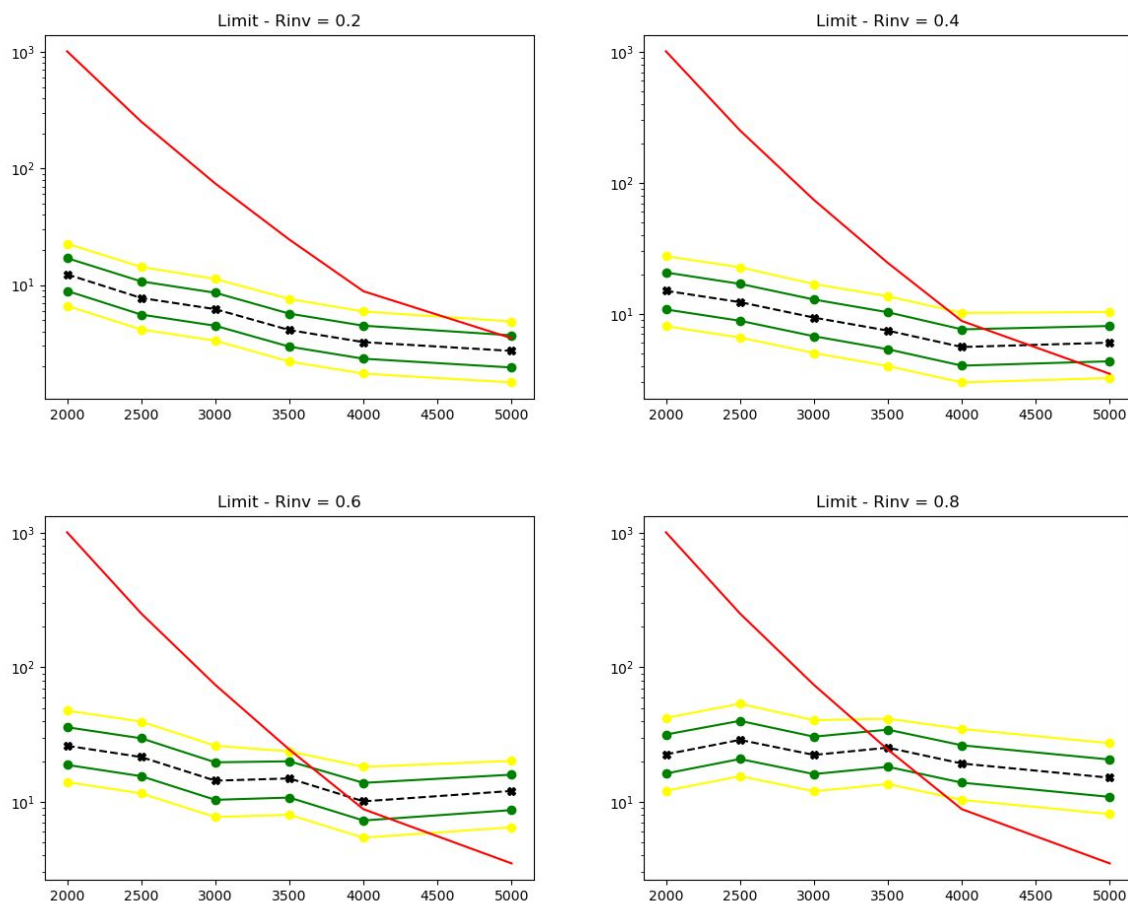


Figure 8.18: 95% C.L. upper limits for signal models across Z' mass, for four different R_{inv} fractions, from the CR region (without systematics).

1743 TODO: 2D limit A 2D limit presentation is also being considered, in the (R_{inv}, mass) plane.

1744 The ability of the fit to identify is a significant excess is tested by calculating the limits on

1745 signal injected toys. 5σ of signal is injected for each signal point into 50 Asimov data toys. The
1746 number of signal events necessary for a 5σ excess is calculated for each signal point from the
1747 expected limits in the background-only case shown in Figure 8.18. The expected limit represents
1748 the limit on a 2σ excess, so a 5σ excess requires 2.5x as much signal. Figure ?? demonstrates
1749 the impact of this signal injection on the limits. The observed limit is significantly higher than the
1750 expected limit for all signal points, indicating the ability of the fit to identify a significant signal
1751 excess. TODO: observed limit plots

1752 8.5.2 Discovery Strategy

1753 Model-independent fits for the discovery region are performed using *pyBumpHunter* [74]. The
1754 strategy consists of comparing the data in a given m_T spectrum of interest to a background esti-
1755 mation derived by performing the polynomial fit and sampling from the post-fit function into a
1756 histogram.

1757 The polynomial fit is done to an m_T distribution with 180 bins (25 GeV wide), half the width
1758 of the fits in the SVJ Fit region (50 GeV wide). The narrower bins allow for rebinning based on
1759 the *signal mass resolution* of the SVJ signals. The binning strategy is outlined in Appendix D.1.

1760 Figure 8.19 shows the fit and residuals with of the polynomial with the narrower binning in the
1761 CR and the Discovery VR data. Figure 8.20 shows the post-fit values of the fit parameters and their
1762 uncertainties for the CR and VR. These results indicate good ability of the 5-parameter polynomial
1763 to model the ANTELOPE selected data.

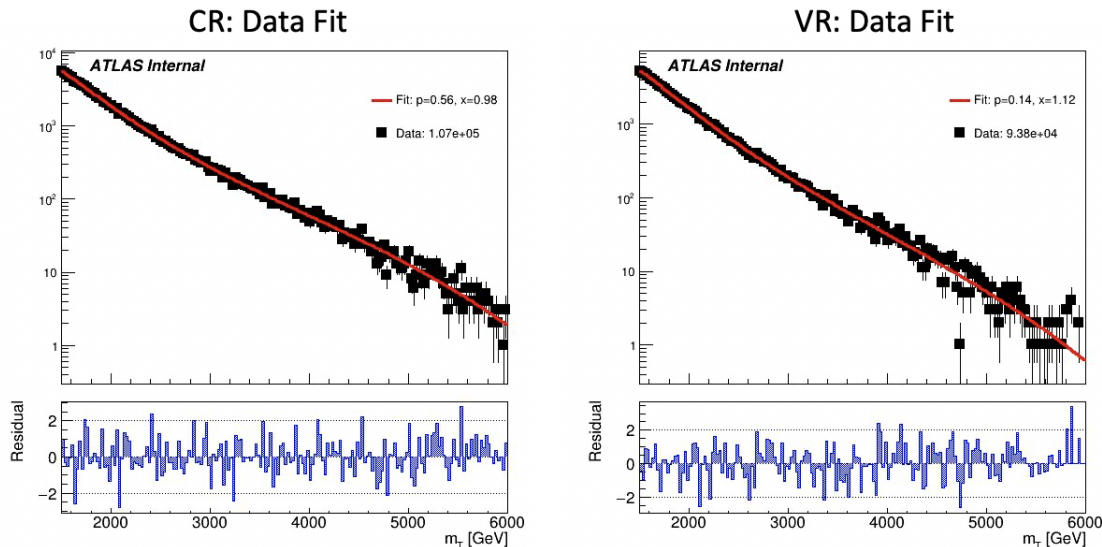


Figure 8.19: Post-fit function and residuals for the ANTELOPE CR and VR.

1764 The studies shown in Section 8.5.1 validate the robustness of the background polynomial fit.
1765 The narrower bins are the only difference for polynomial fitting between the SVJ Fit and Discovery
1766 Fit strategies, and they are not observed to reduce the quality or consistency of the fit.

Parameter	CR		VR	
	Value	Error	Value	Error
p1	1.0709e+05	4.65e+02	9.3776e+04	4.34e+02
p2	4.5945e+01	3.03e+00	4.5787e+01	3.78e+00
p3	5.8566e+01	3.88e+00	5.6014e+01	4.58e+00
p4	2.5593e+01	1.50e+00	2.4914e+01	1.73e+00
p5	3.9196e+00	2.22e-01	3.8809e+00	2.53e-01

Figure 8.20: Post-fit parameters for the ANTELOPE CR and VR.

1767 BumpHunter Fits

1768 The signal mass resolution binning strategy described in Appendix D.1 creates a monotonically
 1769 increasing set of bins. While the SVJ signals help inform the binning, the binning is still broadly
 1770 applicable to a variety of potential signal models. The mass resolution of any resonant signal
 1771 generally widens as the mass of the mediator particle increases. A similar strategy and binning
 1772 was used in the generic heavy resonance search presented in Ref. [73]. The resulting set of 15 bins
 1773 to be used in the BumpHunter fits varies in width from 100 GeV at the m_T core to 925 GV in the
 1774 m_T tail.

1775 Figure 8.21 shows the result of running BumpHunter over the rebinned CR and VR m_T spectra.
 1776 The background estimation is given by polynomial fit function. The high p-values (>0.01) indicate
 1777 good agreement with the background estimation.

1778 Figure 8.22 shows BumpHunter p-values over 100 Asimov trials, where each toy is scaled to
 1779 the statistics of the SR. The agreement is generally very good, as the p-values trend towards higher
 1780 values. No fits with a *spurious signal* are found. A spurious signal would be indicated by a fit with
 1781 a p-value < 0.01 , indicating a bump of at least 2σ significance.

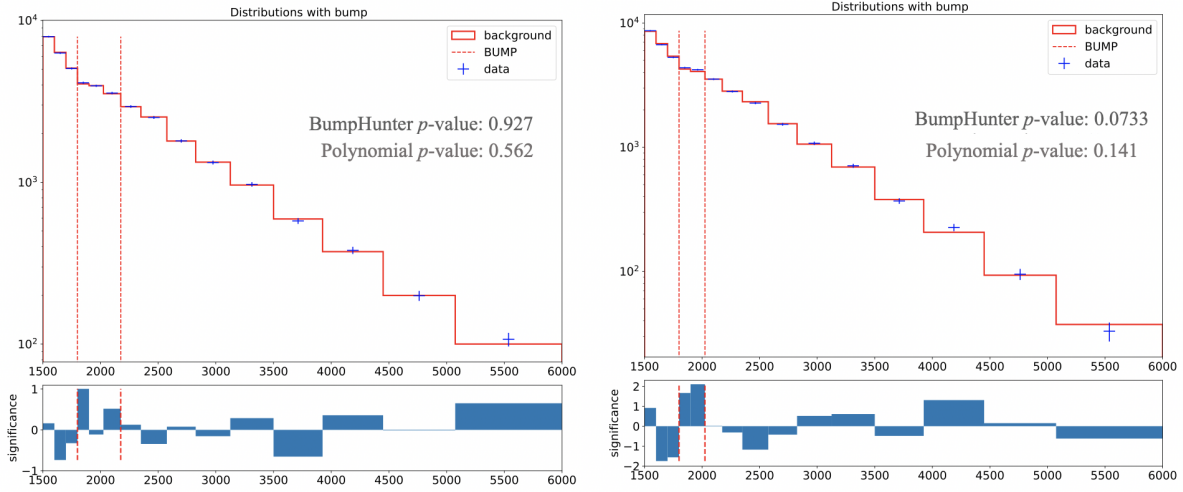


Figure 8.21: BumpHunter fits on the ANTELOPE m_T spectra for both the CR (left) and VR (right). In a signal-depleted region, good agreement with the background estimation is observed.

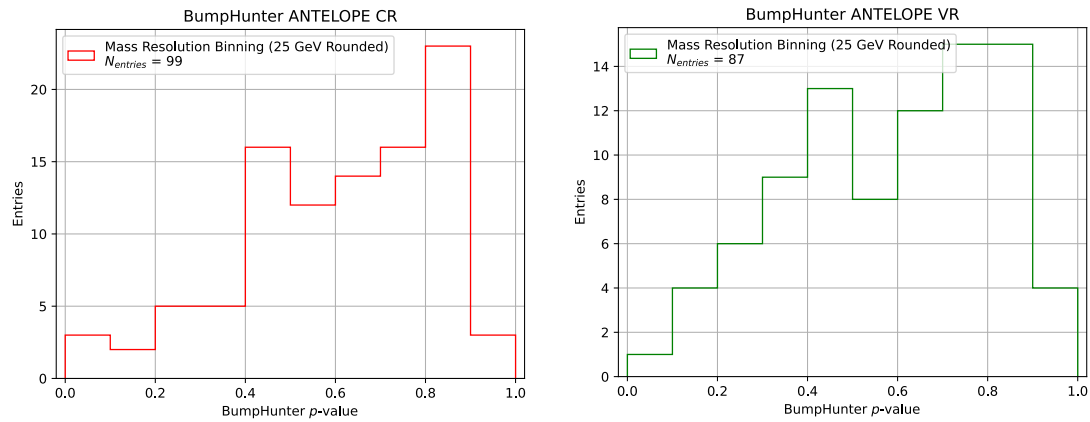


Figure 8.22: BumpHunter p-values extracted for 100 Asimov toys for both the ANTELOPE CR (left) and VR (right).

1782

1783

Chapter 9: Results

1784

Conclusion or Epilogue

1785 Use this page for your epilogue or conclusion if applicable; please use only one of the titles
1786 for this page. Otherwise, you may delete it. Use this page for your epilogue or conclusion if
1787 applicable; please use only one of the titles for this page. Otherwise, you may delete it. Use this
1788 page for your epilogue or conclusion if applicable; please use only one of the titles for this page.
1789 Otherwise, you may delete it. Use this page for your epilogue or conclusion if applicable; please
1790 use only one of the titles for this page. Otherwise, you may delete it. Use this page for your
1791 epilogue or conclusion if applicable; please use only one of the titles for this page. Otherwise,
1792 you may delete it. Use this page for your epilogue or conclusion if applicable; please use only one
1793 of the titles for this page. Otherwise, you may delete it. Use this page for your epilogue or
1794 conclusion if applicable; please use only one of the titles for this page. Otherwise, you may delete
1795 it. Use this page for your epilogue or conclusion if applicable; please use only one of the titles for
1796 this page. Otherwise, you may delete it. Use this page for your epilogue or conclusion if
1797 applicable; please use only one of the titles for this page. Otherwise, you may delete it. Use this
1798 page for your epilogue or conclusion if applicable; please use only one of the titles for this page.
1799 Otherwise, you may delete it. Use this page for your epilogue or conclusion if applicable; please
1800 use only one of the titles for this page. Otherwise, you may delete it. Use this page for your
1801 epilogue or conclusion if applicable; please use only one of the titles for this page. Otherwise,
1802 you may delete it. Use this page for your epilogue or conclusion if applicable; please use only one
1803 of the titles for this page. Otherwise, you may delete it. Use this page for your epilogue or
1804 conclusion if applicable; please use only one of the titles for this page. Otherwise, you may delete

1805 it. Use this page for your epilogue or conclusion if applicable; please use only one of the titles for
1806 this page. Otherwise, you may delete it. Use this page for your epilogue or conclusion if
1807 applicable; please use only one of the titles for this page. Otherwise, you may delete it. Use this
1808 page for your epilogue or conclusion if applicable; please use only one of the titles for this page.
1809 Otherwise, you may delete it. Use this page for your epilogue or conclusion if applicable; please
1810 use only one of the titles for this page. Otherwise, you may delete it. Use this page for your
1811 epilogue or conclusion if applicable; please use only one of the titles for this page. Otherwise,
1812 you may delete it. Use this page for your epilogue or conclusion if applicable; please use only one
1813 of the titles for this page. Otherwise, you may delete it. Use this page for your epilogue or
1814 conclusion if applicable; please use only one of the titles for this page. Otherwise, you may delete
1815 it. Use this page for your epilogue or conclusion if applicable; please use only one of the titles for
1816 this page. Otherwise, you may delete it. Use this page for your epilogue or conclusion if
1817 applicable; please use only one of the titles for this page. Otherwise, you may delete it. Use this
1818 page for your epilogue or conclusion if applicable; please use only one of the titles for this page.
1819 Otherwise, you may delete it. Use this page for your epilogue or conclusion if applicable; please
1820 use only one of the titles for this page. Otherwise, you may delete it. Use this page for your
1821 epilogue or conclusion if applicable; please use only one of the titles for this page. Otherwise,
1822 you may delete it. Use this page for your epilogue or conclusion if applicable; please use only one
1823 of the titles for this page. Otherwise, you may delete it. Use this page for your epilogue or
1824 conclusion if applicable; please use only one of the titles for this page. Otherwise, you may delete
1825 it. Use this page for your epilogue or conclusion if applicable; please use only one of the titles for
1826 this page. Otherwise, you may delete it. Use this page for your epilogue or conclusion if
1827 applicable; please use only one of the titles for this page. Otherwise, you may delete it. Use this
1828 page for your epilogue or conclusion if applicable; please use only one of the titles for this page.
1829 Otherwise, you may delete it. Use this page for your epilogue or conclusion if applicable; please
1830 use only one of the titles for this page. Otherwise, you may delete it. Use this page for your
1831 epilogue or conclusion if applicable; please use only one of the titles for this page. Otherwise,

1832 you may delete it. Use this page for your epilogue or conclusion if applicable; please use only one
1833 of the titles for this page. Otherwise, you may delete it. Use this page for your epilogue or
1834 conclusion if applicable; please use only one of the titles for this page. Otherwise, you may delete
1835 it. Use this page for your epilogue or conclusion if applicable; please use only one of the titles for
1836 this page. Otherwise, you may delete it. Use this page for your epilogue or conclusion if
1837 applicable; please use only one of the titles for this page. Otherwise, you may delete it. Use this
1838 page for your epilogue or conclusion if applicable; please use only one of the titles for this page.
1839 Otherwise, you may delete it. Use this page for your epilogue or conclusion if applicable; please
1840 use only one of the titles for this page. Otherwise, you may delete it. Use this page for your
1841 epilogue or conclusion if applicable; please use only one of the titles for this page. Otherwise,
1842 you may delete it. Use this page for your epilogue or conclusion if applicable; please use only one
1843 of the titles for this page. Otherwise, you may delete it. Use this page for your epilogue or
1844 conclusion if applicable; please use only one of the titles for this page. Otherwise, you may delete
1845 it. Use this page for your epilogue or conclusion if applicable; please use only one of the titles for
1846 this page. Otherwise, you may delete it. Use this page for your epilogue or conclusion if
1847 applicable; please use only one of the titles for this page. Otherwise, you may delete it. Use this
1848 page for your epilogue or conclusion if applicable; please use only one of the titles for this page.
1849 Otherwise, you may delete it. Use this page for your epilogue or conclusion if applicable; please
1850 use only one of the titles for this page. Otherwise, you may delete it. Use this page for your
1851 epilogue or conclusion if applicable; please use only one of the titles for this page. Otherwise,
1852 you may delete it. Use this page for your epilogue or conclusion if applicable; please use only one
1853 of the titles for this page. Otherwise, you may delete it. Use this page for your epilogue or
1854 conclusion if applicable; please use only one of the titles for this page. Otherwise, you may delete
1855 it. Use this page for your epilogue or conclusion if applicable; please use only one of the titles for
1856 this page. Otherwise, you may delete it. Use this page for your epilogue or conclusion if
1857 applicable; please use only one of the titles for this page. Otherwise, you may delete it. Use this
1858 page for your epilogue or conclusion if applicable; please use only one of the titles for this page.

1859 Otherwise, you may delete it. Use this page for your epilogue or conclusion if applicable; please
1860 use only one of the titles for this page. Otherwise, you may delete it. Use this page for your
1861 epilogue or conclusion if applicable; please use only one of the titles for this page. Otherwise,
1862 you may delete it. Use this page for your epilogue or conclusion if applicable; please use only one
1863 of the titles for this page. Otherwise, you may delete it. Use this page for your epilogue or
1864 conclusion if applicable; please use only one of the titles for this page. Otherwise, you may delete
1865 it. Use this page for your epilogue or conclusion if applicable; please use only one of the titles for
1866 this page. Otherwise, you may delete it. Use this page for your epilogue or conclusion if
1867 applicable; please use only one of the titles for this page. Otherwise, you may delete it. Use this
1868 page for your epilogue or conclusion if applicable; please use only one of the titles for this page.
1869 Otherwise, you may delete it. Use this page for your epilogue or conclusion if applicable; please
1870 use only one of the titles for this page. Otherwise, you may delete it. Use this page for your
1871 epilogue or conclusion if applicable; please use only one of the titles for this page. Otherwise,
1872 you may delete it. Use this page for your epilogue or conclusion if applicable; please use only one
1873 of the titles for this page. Otherwise, you may delete it. Use this page for your epilogue or
1874 conclusion if applicable; please use only one of the titles for this page. Otherwise, you may delete
1875 it. Use this page for your epilogue or conclusion if applicable; please use only one of the titles for
1876 this page. Otherwise, you may delete it. Use this page for your epilogue or conclusion if
1877 applicable; please use only one of the titles for this page. Otherwise, you may delete it. Use this
1878 page for your epilogue or conclusion if applicable; please use only one of the titles for this page.
1879 Otherwise, you may delete it. Use this page for your epilogue or conclusion if applicable; please
1880 use only one of the titles for this page. Otherwise, you may delete it. Use this page for your
1881 epilogue or conclusion if applicable; please use only one of the titles for this page. Otherwise,
1882 you may delete it. Use this page for your epilogue or conclusion if applicable; please use only one
1883 of the titles for this page. Otherwise, you may delete it. Use this page for your epilogue or
1884 conclusion if applicable; please use only one of the titles for this page. Otherwise, you may delete
1885 it.

References

- [1] Jens Erler and Paul Langacker. “Electroweak model and constraints on new physics”. In: (July 2004). arXiv: hep-ph/0407097.
- [2] David J Griffiths. *Introduction to elementary particles; 2nd rev. version*. Physics textbook. New York, NY: Wiley, 2008.
- [3] M. Tanabashi et al. “Review of Particle Physics”. In: *Phys. Rev. D* 98 (3 2018), pp. 847–851.
- [4] E. Noether. “Invariante Variationsprobleme”. In: *Nachr. d. König. Gesellsch. d. Wiss. zu Göttingen, Math-phys. Klasse*, Seite 235–157 (1918). eprint: www.physics.ucla.edu/\sim\cwp/articles/noether.trans/german/emmy235.html.
- [5] J. H. Christenson et al. “Evidence for the 2π Decay of the K_2^0 Meson”. In: *Phys. Rev. Lett.* 13 (1964), pp. 138–140.
- [6] Michael Gronau. “CP Violation in B Meson Decays”. In: *Nuclear Physics B - Proceedings Supplements* 142 (May 2005), 263–270.
- [7] J. E. Augustin et al. “Discovery of a Narrow Resonance in e^+e^- Annihilation”. In: *Phys. Rev. Lett.* 33 (1974), pp. 1406–1408.
- [8] J. J. Aubert et al. “Experimental Observation of a Heavy Particle J ”. In: *Phys. Rev. Lett.* 33 (1974), pp. 1404–1406.
- [9] Martin L. Perl et al. “Evidence for Anomalous Lepton Production in e+ - e- Annihilation”. In: *Phys. Rev. Lett.* 35 (1975), pp. 1489–1492.
- [10] S. W. Herb et al. “Observation of a Dimuon Resonance at 9.5-GeV in 400-GeV Proton-Nucleus Collisions”. In: *Phys. Rev. Lett.* 39 (1977), pp. 252–255.
- [11] F. Abe et al. “Observation of top quark production in $\bar{p}p$ collisions”. In: *Phys. Rev. Lett.* 74 (1995), pp. 2626–2631. arXiv: hep-ex/9503002.
- [12] S. Abachi et al. “Observation of the top quark”. In: *Phys. Rev. Lett.* 74 (1995), pp. 2632–2637. arXiv: hep-ex/9503003.
- [13] K. Kodama et al. “Observation of tau neutrino interactions”. In: *Phys. Lett. B* 504 (2001), pp. 218–224. arXiv: hep-ex/0012035.

- 1913 [14] G. Arnison et al. “Experimental Observation of Lepton Pairs of Invariant Mass Around 95-
 1914 GeV/c**2 at the CERN SPS Collider”. In: *Phys. Lett. B* 126 (1983), pp. 398–410.
- 1915 [15] P. Bagnaia et al. “Evidence for $Z^0 \rightarrow e^+e^-$ at the CERN $\bar{p}p$ Collider”. In: *Phys. Lett. B* 129
 1916 (1983), pp. 130–140.
- 1917 [16] Serguei Chatrchyan et al. “Observation of a New Boson at a Mass of 125 GeV with the
 1918 CMS Experiment at the LHC”. In: *Phys. Lett. B* 716 (2012), pp. 30–61. arXiv: 1207.7235
 1919 [hep-ex].
- 1920 [17] Georges Aad et al. “Observation of a new particle in the search for the Standard Model
 1921 Higgs boson with the ATLAS detector at the LHC”. In: *Phys. Lett. B* 716 (2012), pp. 1–29.
 1922 arXiv: 1207.7214 [hep-ex].
- 1923 [18] K. G. Begeman, A. H. Broeils, and R. H. Sanders. “Extended rotation curves of spiral galax-
 1924 ies: Dark haloes and modified dynamics”. In: *Mon. Not. Roy. Astron. Soc.* 249 (1991), p. 523.
- 1925 [19] Y. Ashie et al. “Evidence for an oscillatory signature in atmospheric neutrino oscillation”.
 1926 In: *Phys. Rev. Lett.* 93 (2004), p. 101801. arXiv: hep-ex/0404034.
- 1927 [20] C. Abel et al. “Measurement of the Permanent Electric Dipole Moment of the Neutron”. In:
 1928 *Phys. Rev. Lett.* 124.8 (2020), p. 081803. arXiv: 2001.11966 [hep-ex].
- 1929 [21] Guillaume Albouy et al. “Theory, phenomenology, and experimental avenues for dark show-
 1930 ers: a Snowmass 2021 report”. In: *The European Physical Journal C* 82.12 (Dec. 2022).
- 1931 [22] Timothy Cohen et al. “LHC searches for dark sector showers”. In: *Journal of High Energy
 1932 Physics* 2017.11 (Nov. 2017).
- 1933 [23] Lyndon Evans and Philip Bryant. “LHC Machine”. In: *Journal of Instrumentation* 3.08
 1934 (2008), S08001.
- 1935 [24] “The ATLAS Experiment at the CERN Large Hadron Collider”. In: *JINST* 3 (2008). Also
 1936 published by CERN Geneva in 2010, S08003.
- 1937 [25] “The CMS experiment at the CERN LHC”. In: *Journal of Instrumentation* 3.08 (2008),
 1938 S08004.
- 1939 [26] “The ALICE experiment at the CERN LHC”. In: *Journal of Instrumentation* 3.08 (2008),
 1940 S08002.
- 1941 [27] “The LHCb Detector at the LHC”. In: *Journal of Instrumentation* 3.08 (2008), S08005.
- 1942 [28] Ana Lopes and Melissa Loyse Perrey. *FAQ-LHC The guide*. 2022.

- 1943 [29] Esma Mobs. “The CERN accelerator complex in 2019. Complexe des accélérateurs du
1944 CERN en 2019”. In: (2019). General Photo.
- 1945 [30] *Pulling together: Super Conducting electromagnets*. <https://home.cern/science/engineering/pulling-together-superconducting-electromagnets>.
1946 Accessed: 2024-01-05.
1947
- 1948 [31] *The High-Luminosity LHC*. <https://voisins.web.cern.ch/en/high-luminosity-lhc-hl-lhc>. Accessed: 2024-01-05.
1949
- 1950 [32] Aad G., et al. (ATLAS Collaboration and CMS Collaboration). “Combined Measurement of
1951 the Higgs Boson Mass in pp Collisions at $\sqrt{s} = 7$ and 8 TeV with the ATLAS and CMS
1952 Experiments”. In: *Phys. Rev. Lett.* 114 (19 2015), p. 191803.
- 1953 [33] O. Aberle et al. *High-Luminosity Large Hadron Collider (HL-LHC): Technical design re-*
1954 *port*. CERN Yellow Reports: Monographs. Geneva: CERN, 2020.
- 1955 [34] The ATLAS Collaboration. “The ATLAS Experiment at the CERN Large Hadron Collider”.
1956 In: *Journal of Instrumentation* 3.08 (2008), S08003.
- 1957 [35] G Aad, B Abbott, and ATLAS Collaboration. “Performance of the reconstruction of large
1958 impact parameter tracks in the inner detector of ATLAS”. In: *Eur. Phys. J. C Part. Fields*
1959 83.11 (Nov. 2023).
- 1960 [36] Joao Pequenao. *Computer Generated image of the ATLAS calorimeter*. 2008.
- 1961 [37] *ATLAS liquid-argon calorimeter: Technical Design Report*. Technical design report. AT-
1962 LAS. Geneva: CERN, 1996.
- 1963 [38] H A Gordon. “Liquid argon calorimetry for the SSC”. In: () .
- 1964 [39] Henric Wilkens and (on behalf of the ATLAS LArg Collaboration). “The ATLAS Liquid
1965 Argon calorimeter: An overview”. In: *Journal of Physics: Conference Series* 160.1 (2009),
1966 p. 012043.
- 1967 [40] *Technical Design Report for the Phase-II Upgrade of the ATLAS Tile Calorimeter*. Tech.
1968 rep. Geneva: CERN, 2017.
- 1969 [41] “Technical Design Report for the Phase-II Upgrade of the ATLAS Muon Spectrometer”. In:
1970 () .
- 1971 [42] L Pontecorvo. “The ATLAS Muon Spectrometer”. In: (2004). revised version number 1
1972 submitted on 2003-07-27 16:31:16.

- 1973 [43] *ATLAS magnet system: Technical Design Report, 1*. Technical design report. ATLAS. Geneva:
 1974 CERN, 1997.
- 1975 [44] 2024.
- 1976 [45] Tommaso Colombo. “Data-flow Performance Optimisation on Unreliable Networks: the AT-
 1977 LAS Data-Acquisition Case”. In: *Journal of Physics: Conference Series* 608 (May 2015),
 1978 p. 012005.
- 1979 [46] Joao Pequenao. “Event Cross Section in a computer generated image of the ATLAS detec-
 1980 tor.” 2008.
- 1981 [47] ATLAS Collaboration. “ATLAS Experiment Implements Heterogeneous Particle Recon-
 1982 struction with Intel oneAPI Tools”. General Photo. 2023.
- 1983 [48] ATLAS Collaboration. “Electron and photon performance measurements with the ATLAS
 1984 detector using the 2015–2017 LHC proton-proton collision data”. In: *Journal of Instrumen-*
 1985 *tation* 14.12 (2019), P12006.
- 1986 [49] Chiara Deponte. “Studies on the properties of non-prompt photons at the ATLAS experi-
 1987 ment”. Presented 16 Aug 2022. Technische Universitaet Dortmund (DE), 2022.
- [50] ATLAS Collaboration. “Muon reconstruction performance of the ATLAS detector in pro-
 ton–proton collision data at
 \sqrt{s}
 1988 $s = 13 \text{ TeV}$ ”. In: *The European Physical Journal C* 76.5 (2016).
- 1989 [51] Sebastien Rettie. *Muon identification and performance in the ATLAS experiment*. Tech. rep.
 1990 Geneva: CERN, 2018.
- 1991 [52] B. R. Webber. *Fragmentation and Hadronization*. 1999. arXiv: hep-ph/9912292 [hep-ph].
- 1992 [53] Eric M. Metodiev. *The Fractal Lives of Jets* | Eric M. Metodiev — ericmetodiev.com. <https://www.ericmetodiev.com/post/jetformation/>. 2019, note = [Accessed 18-
 1993 05-2024],
- 1995 [54] Matteo Cacciari, Gavin P Salam, and Gregory Soyez. “The anti-ktjet clustering algorithm”.
 1996 In: *Journal of High Energy Physics* 2008.04 (Apr. 2008), 063–063.
- 1997 [55] Matteo Cacciari, Gavin P. Salam, and Gregory Soyez. “FastJet user manual: (for version
 1998 3.0.2)”. In: *The European Physical Journal C* 72.3 (Mar. 2012).
- 1999 [56] Steven Schramm. *ATLAS Jet Reconstruction, Calibration, and Tagging of Lorentz-boosted
 2000 Objects*. Tech. rep. Geneva: CERN, 2017.

- 2001 [57] ATLAS Collaboration. “Topological cell clustering in the ATLAS calorimeters and its performance in LHC Run 1”. In: *The European Physical Journal C* 77.7 (July 2017).
- 2003 [58] ATLAS Collaboration. “Jet reconstruction and performance using particle flow with the ATLAS Detector”. In: *The European Physical Journal C* 77.7 (July 2017).
- 2005 [59] Stephen D. Ellis and Davison E. Soper. “Successive combination jet algorithm for hadron collisions”. In: *Physical Review D* 48.7 (Oct. 1993), 3160–3166.
- 2007 [60] M. Wobisch and T. Wengler. *Hadronization Corrections to Jet Cross Sections in Deep-Inelastic Scattering*. 1999. arXiv: hep-ph/9907280 [hep-ph].
- 2009 [61] Gavin P Salam and Gr  gory Soyez. “A practical seedless infrared-safe cone jet algorithm”. In: *Journal of High Energy Physics* 2007.05 (May 2007), 086–086.
- 2011 [62] Gavin P. Salam. “Towards jetography”. In: *The European Physical Journal C* 67.3–4 (May 2010), 637–686.
- 2013 [63] *A Monte Carlo study of track association to jets for b-tagging*. Tech. rep. Geneva: CERN, 2021.
- 2015 [64] *Flavor Tagging with Track Jets in Boosted Topologies with the ATLAS Detector*. Tech. rep. All figures including auxiliary figures are available at <https://atlas.web.cern.ch/Atlas/GROUPS/PHYSICS/PHYS-PUB-2014-013>. Geneva: CERN, 2014.
- 2018 [65] ATLAS Collaboration. “Performance of missing transverse momentum reconstruction with the ATLAS detector using proton-proton collisions at $\sqrt{s} = 13$ TeV”. In: *Eur. Phys. J. C* 78.11 (2018), p. 903. arXiv: 1802.08168.
- 2021 [66] GEANT4 Collaboration, S. Agostinelli, et al. “GEANT4 – a simulation toolkit”. In: *Nucl. Instrum. Meth. A* 506 (2003), p. 250.
- 2023 [67] Christian Bierlich et al. *A comprehensive guide to the physics and usage of PYTHIA 8.3*. 2022. arXiv: 2203.11601 [hep-ph].
- 2025 [68] J. Alwall et al. “The automated computation of tree-level and next-to-leading order differential cross sections, and their matching to parton shower simulations”. In: *JHEP* 07 (2014), p. 079. arXiv: 1405.0301 [hep-ph].
- 2028 [69] Jon Butterworth et al. “PDF4LHC recommendations for LHC Run II”. In: *J. Phys. G* 43 (2016), p. 023001. arXiv: 1510.03865 [hep-ph].
- 2030 [70] Peter Skands, Stefano Carrazza, and Juan Rojo. “Tuning PYTHIA 8.1: the Monash 2013 Tune”. In: *Eur. Phys. J. C* 74.8 (2014), p. 3024. arXiv: 1404.5630 [hep-ph].

- 2032 [71] Patrick T. Komiske, Eric M. Metodiev, and Jesse Thaler. “Energy flow networks: deep sets
2033 for particle jets”. In: *Journal of High Energy Physics* 2019.1 (2019).
- 2034 [72] A. Kahn et al. “Anomalous jet identification via sequence modeling”. In: *Journal of Instrumentation* 16.08 (Aug. 2021), P08012.
- 2036 [73] Georges Aad et al. “Anomaly detection search for new resonances decaying into a Higgs
2037 boson and a generic new particle X in hadronic final states using $\sqrt{s} = 13$ TeV pp collisions
2038 with the ATLAS detector”. In: *Phys. Rev. D* 108 (2023), p. 052009. arXiv: 2306.03637
2039 [[hep-ex](#)].
- 2040 [74] Georgios Choudalakis. *On hypothesis testing, trials factor, hypertests and the BumpHunter*.
2041 2011. arXiv: 1101.0390.
- 2042 [75] Peter Loch. “Jet measurements in ATLAS”. In: *J. Phys. Conf. Ser.* 323 (2011). Ed. by Gior-
2043 gio Bellettini, p. 012002.
- 2044 [76] The ATLAS Collaboration. “Search for diboson resonances in hadronic final states in 139
2045 fb-1 of pp collisions at $\sqrt{s} = 13$ TeV with the ATLAS detector”. In: *Journal of High Energy
2046 Physics* 2019.9 (Sept. 2019).
- 2047 [77] *Recommendations for the Modeling of Smooth Backgrounds*. Tech. rep. Geneva: CERN,
2048 2020.
- 2049 [78] The CMS Collaboration. “Search for resonant production of strongly coupled dark matter
2050 in proton-proton collisions at 13 TeV”. In: *Journal of High Energy Physics* 2022.6 (June
2051 2022).
- 2052 [79] Glen Cowan et al. “Asymptotic formulae for likelihood-based tests of new physics”. In: *The
2053 European Physical Journal C* 71.2 (Feb. 2011).
- 2054 [80] Ryan Edgar et al. *Functional Decomposition: A new method for search and limit setting*.
2055 2018. arXiv: 1805.04536 [[physics.data-an](#)].

Appendix A: Trigger Studies

2058 Both the lowest unprescaled E_T^{miss} and single small-R jet triggers were considered for this
 2059 analysis. The E_T^{miss} trigger is observed to have higher efficiency for low mass, high R_{inv} points,
 2060 while the single small-R trigger favors high mass, low R_{inv} points. Figure A.1 shows the yields
 2061 and signal efficiencies across the grid for both these strategies.

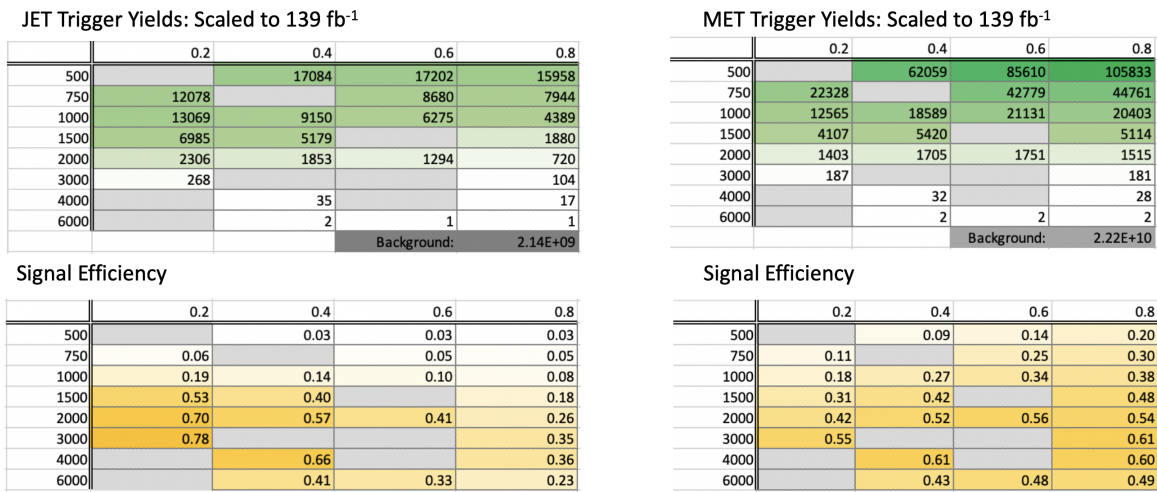


Figure A.1: Trigger yield and efficiency for both the MET trigger and small-R jet trigger approach. Each entry represent a signal point, labelled by the Z' mass and the R_{inv} fraction.

2062 The cross section is higher for the lower Z' mass signal points. As a result, our sensitivity
 2063 to these points and ability to set limits on them is already naturally enhanced. Figure A.2 shows
 2064 the factor of improvement in the inclusive S/\sqrt{B} using each trigger strategy. A cross-check was
 2065 also done calculating S/\sqrt{B} in windows around the mT mass. The results of this cross-check
 2066 confirmed the results shown in Figure A.2.

2067 Figure A.3 shows the ratio of S/\sqrt{B} across the signal grid for the jet trigger compared to the
 2068 E_T^{miss} trigger.

2069 This plot makes clear that the E_T^{miss} trigger favors the low mass, high R_{inv} signal points, while

$(\text{JET Trigger } S/\sqrt{B}) / (\text{Untriggered } S/\sqrt{B})$				
	0.2	0.4	0.6	0.8
500		1.26	1.43	1.53
750	2.99		2.52	2.68
1000	9.24	6.74	5.03	4.07
1500	26.45	20.15		8.83
2000	34.66	28.24	20.57	12.85
3000	39.05			17.35
4000		32.94		17.96
6000		20.57	16.55	11.53

$(\text{MET Trigger } S/\sqrt{B}) / (\text{Untriggered } S/\sqrt{B})$				
	0.2	0.4	0.6	0.8
500		1.43	2.21	3.15
750	1.72		3.86	4.69
1000	2.76	4.26	5.26	5.89
1500	4.83	6.56		7.47
2000	6.55	8.08	8.65	8.40
3000	8.46			9.38
4000		9.51		9.32
6000		6.68	7.43	7.59

Figure A.2: The factor of improvement in S/\sqrt{B} for each trigger method compared to the untriggered case.

	0.2	0.4	0.6	0.8
500		0.89	0.65	0.49
750	1.74		0.65	0.57
1000	3.35	1.58	0.96	0.69
1500	5.47	3.07		1.18
2000	5.29	3.49	2.38	1.53
3000	4.62			1.85
4000		3.46		1.93
6000		3.08	2.23	1.52

Figure A.3: The ratio of S/\sqrt{B} of jet trigger over E_T^{miss} trigger selection.

2070 the single jet trigger favors the high mass, low R_{inv} signal points. A number of considerations led
2071 us to selecting the single jet trigger. First, Figure A.2 illustrates that the sensitivity enhancement is
2072 greater for signals favored by the jet trigger than signals favored by the E_T^{miss} trigger. This indicates
2073 we have more to gain from focusing on the region of our signal grid where the jet trigger is most
2074 efficient. We combined this with the observation that the jet trigger is beneficial for high mass
2075 points where the cross-section is lower and we need to maximize sensitivity to hope to set limits
2076 on these points.

2077 Second, there are a number of analysis variables at our disposal which are more discriminant for
2078 high R_{inv} signals than for low R_{inv} signals. A collection of these variables are shown in Figure A.4.
2079 Given that we had multiple avenues available to enhance sensitivity to low R_{inv} signals through
2080 analysis strategy cuts, we opted for a trigger strategy that benefitted the low R_{inv} signal points.
2081 Additionally, we know E_T^{miss} is highly correlated with these discriminant analysis variables, and a
2082 E_T^{miss} trigger would reduce the effectiveness of these variables. Not implementing the E_T^{miss} trigger
2083 allows us to explore other ways of leveraging E_T^{miss} in the analysis using a cut that is more finely
2084 tuned to the specifics of the signal model than the E_T^{miss} trigger is.

2085 Third, we know that fitting the high R_{inv} mass points would be challenging given their very
2086 broad shapes in the key analysis variable m_T . Given the analysis decision to do a search for
2087 resonant features in m_T , we chose to design a search that emphasized maximizing sensitivity
2088 to the signal points that we were mostly to appear as a resonant feature in m_T . The shape of
2089 m_T and our reduced ability to set limits on high R_{inv} points is demonstrated in the body of this
2090 note. Another search strategy may be more optimal for setting limits on high R_{inv} semi-visible jet
2091 signals, but it is currently outside the scope of this analysis.

2092 A jet or E_T^{miss} trigger was also considered, but abandoned due to concerns about sculpting
2093 features in the smoothly falling E_T^{miss} or leading jet p_T distributions, as shown in Figure A.5.

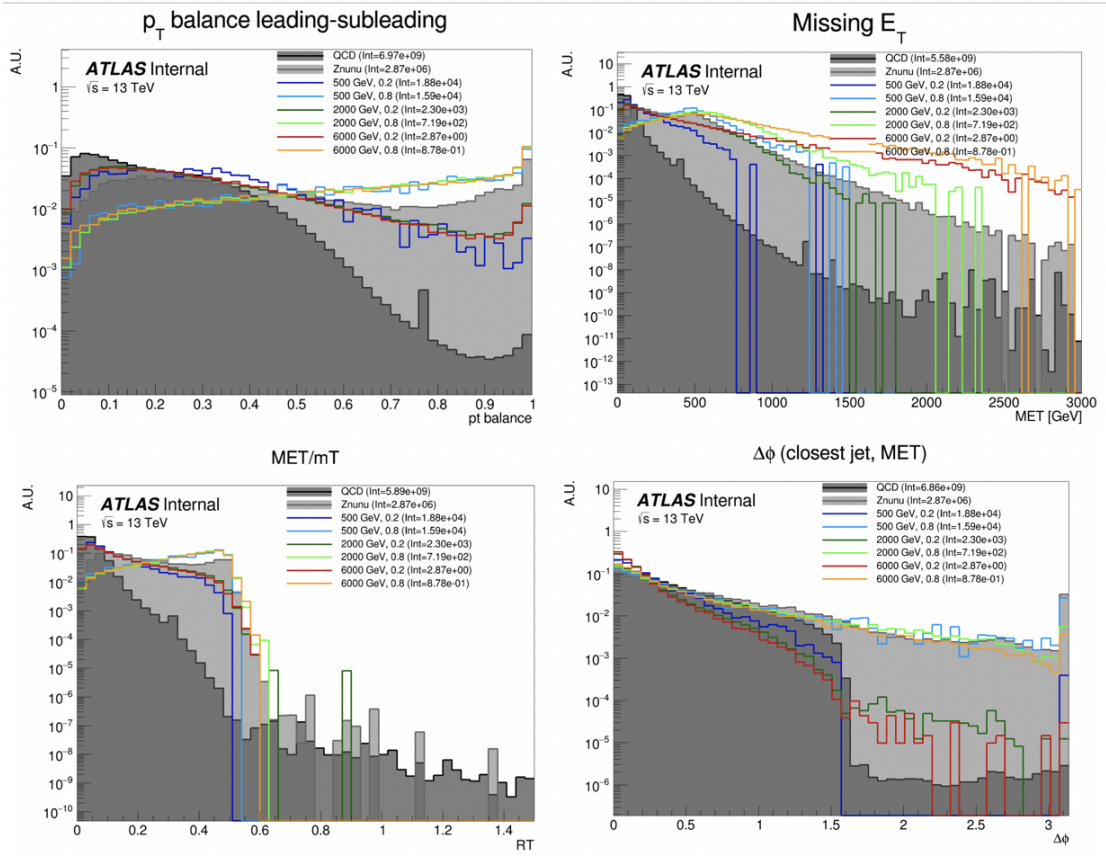


Figure A.4: Analysis variables where high R_{inv} signals a clearly distinct from background and low R_{inv} variables. On the contrary, leading jet p_T is one of the only variables where low R_{inv} signals are distinct from background.

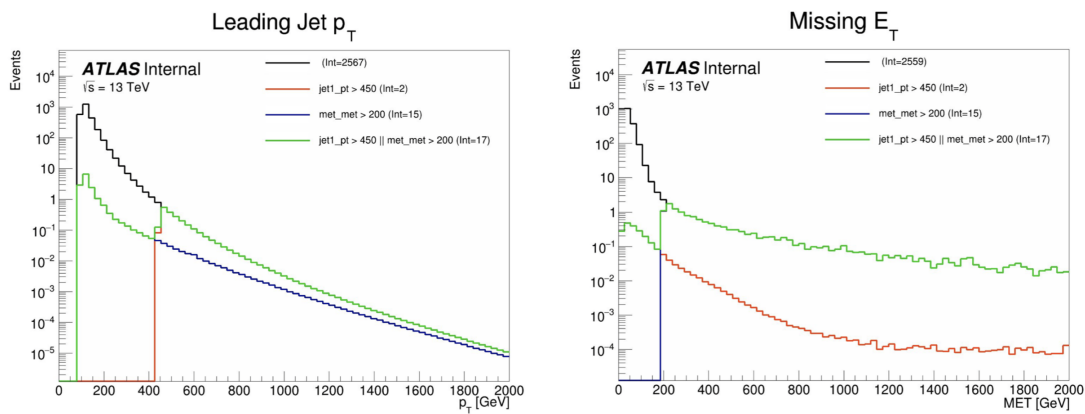


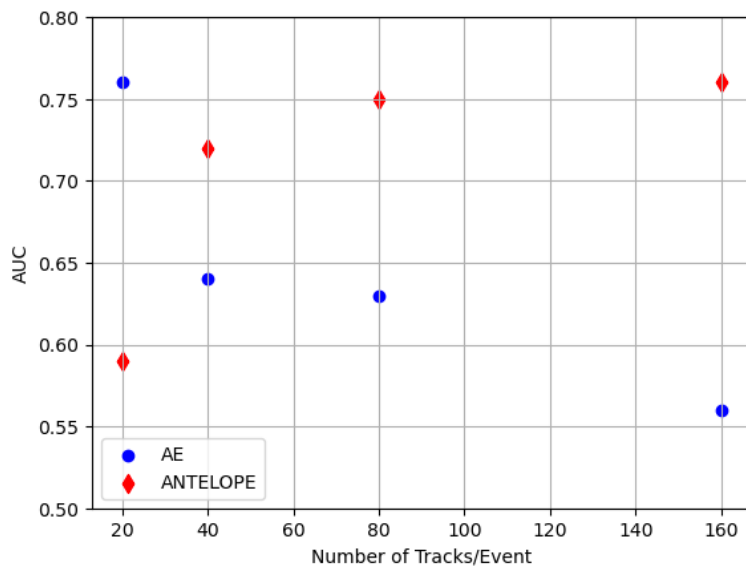
Figure A.5: OR of jet and E_T^{miss} triggers.

Appendix B: Machine Learning Approaches

2096 B.1 Unsupervised: AE vs. ANTELOPE

2097 To understand the benefits of the semi-supervised ANTELOPE approach, we study the AN-
 2098 TELOPE in comparison to a traditional anomaly detection architecture like an autoencoder. The
 2099 autoencoder cannot accommodate variable length or permutation invariant inputs.

2100 Figure B.1 shows the AUC determined by each of these two tools as a function of number
 2101 of tracks. The trend is that the AE suffers when more information is given, due to the presence
 2102 of 0-padding. In contrast, the ANTELOPE architecture performs better with more information,
 motivating the use of high dimensional input modelin with this method.

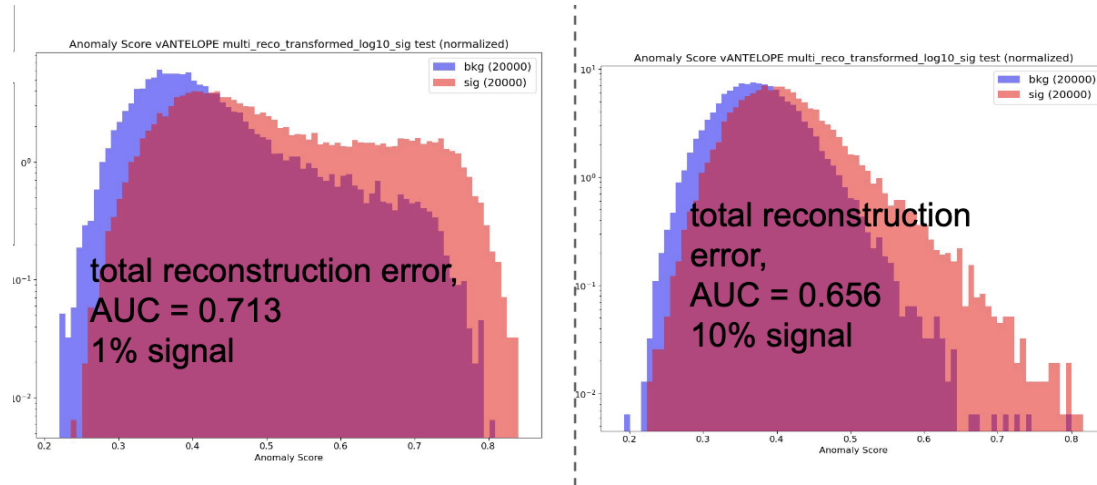


- Confirms that AE is negatively sensitive to zero padding while ANTELOPE sees a performance improvement as it sees more “information”

2103 Figure B.1

2104 **Signal Contamination**

2105 To understand the effect of signal contamination in training on the ANTELOPE score, we inject
2106 a percent of signal events into the data used to train the ANTELOPE autoencoder stage and look
2107 at the AUC on signals. Figure B.2 shows no variation in AUC with 1% contamination in training
data, but a few % drop going up to 10%.



2108 Figure B.2

2109 **B.2 PFN Optimality Checks**

2110 The PFN is trained using QCD as the background. A study was done to compare the perfor-
2111 mance of the tool in the analysis context if it trains against QCD or a representative MC background
2112 considering the small fractions of other processes ($V+jets$, top) that would contribute at preselec-
2113 tion. Figure B.3 shows the AUC across the grid for both training approaches, revealing better
2114 performance if the tool focuses on learning QCD differences.

2115 Further studies were done to ensure the relatively optimality of the single PFN model, trained
2116 over combined signals, across the grid. As the grid spans signals with a large range of E_T^{miss} , their
2117 varying input features and background composition may be conducive to separate PFN models
2118 trained on high and low E_T^{miss} signal points to better capture the signal-background differences.
2119 Figure B.4 shows a comparison of the signal-inclusive PFN model performance and the perfor-

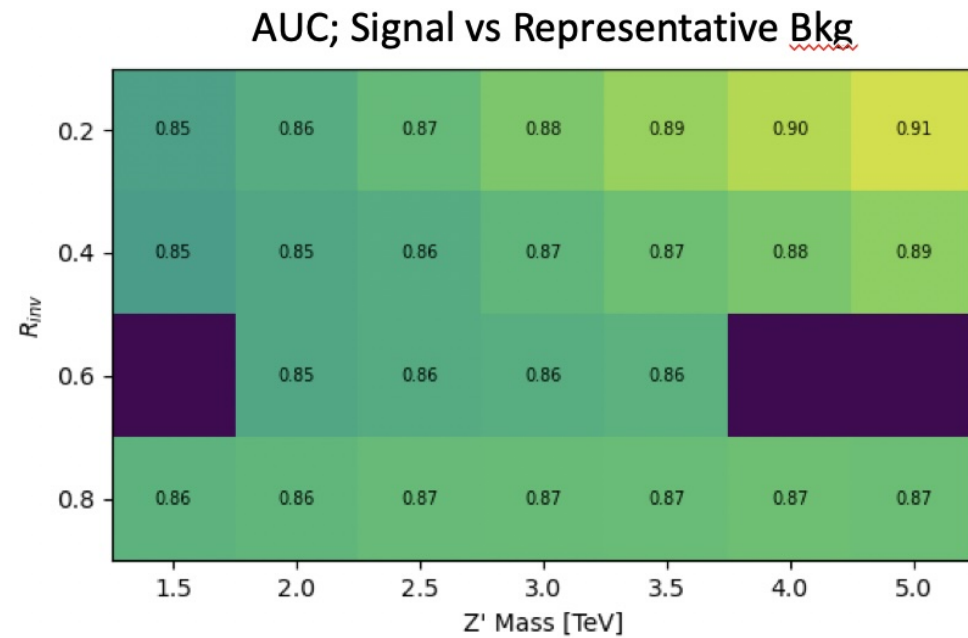
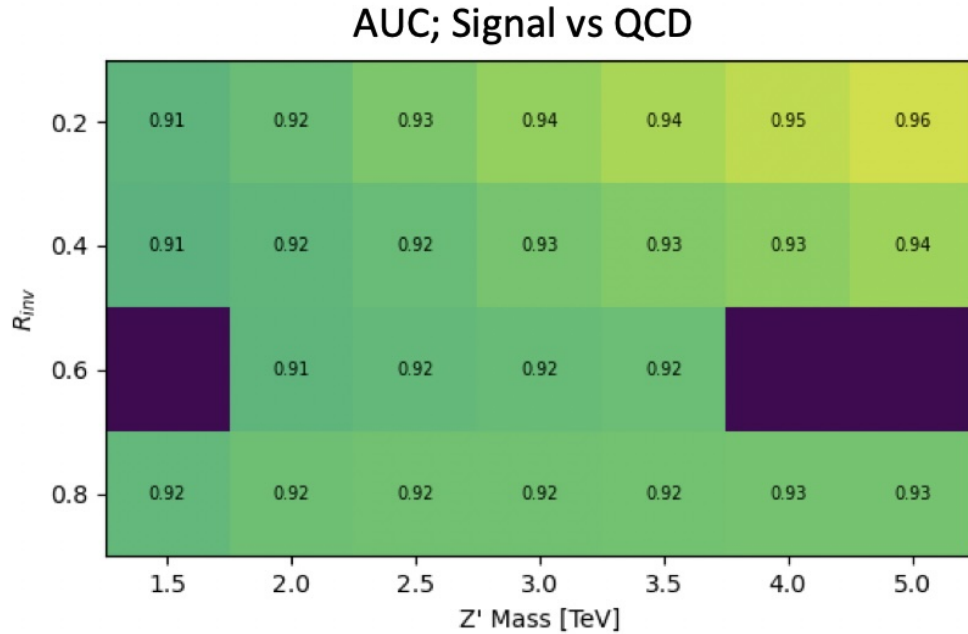


Figure B.3: AUC from the PFN score for each signal in the SVJ grid, shown versus the QCD-only training sample (top) and the total MC background (bottom). Note the three missing points will be added shortly - they were delayed due to a DAOD production mistake.

2120 mance of models separated into high and low R_{inv} signals in training. The most notable impact is
 2121 found for the low R_{inv} and high mass points, indicating that the signal-inclusive PFN is learning
 2122 morning about the distinction between high- E_T^{miss} signals and backgrounds. However, these high
 2123 mass points are also the most challenging to find due to their very wide resonance on top of m_T ,
 2124 and in the final projected sensitivity in the m_T window the differences are $< 10\%$ across the grid.
 2125 To maintain a harmonized strategy with the ANTELOPE region we keep the inclusive PFN model
 2126 as the final version.

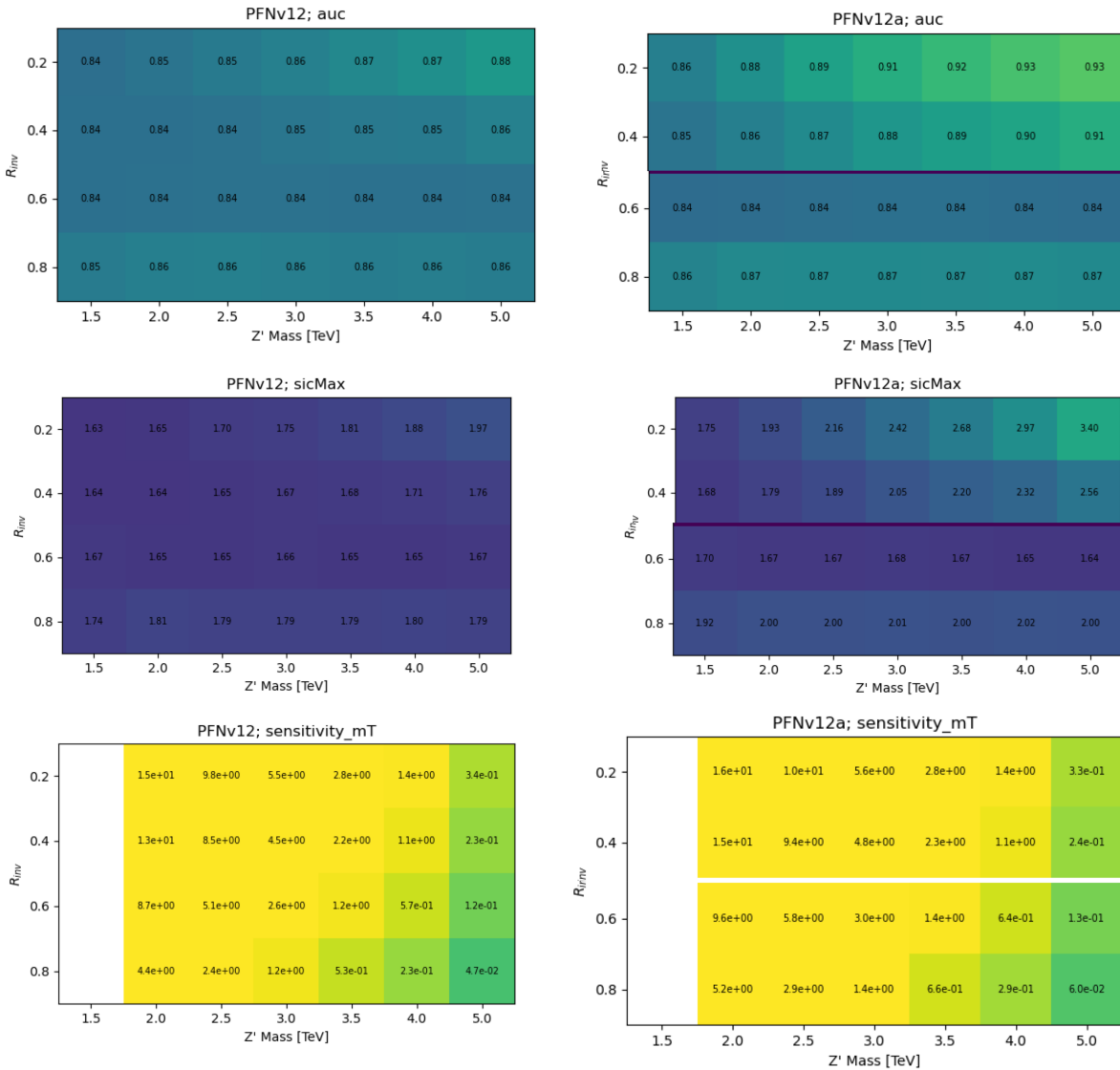


Figure B.4: Comparison of PFN AUC (top), SIC (middle), and sensitivity in the m_T mass window (bottom) for a single PFN model (left) vs. two models, trained on $R_{inv} < 0.5$ and > 0.5 separately.

2127 Figure B.5 shows the optimal cut on the PFN score for each point in the signal grid, motivating
the loose inclusive choice used to define the SR.

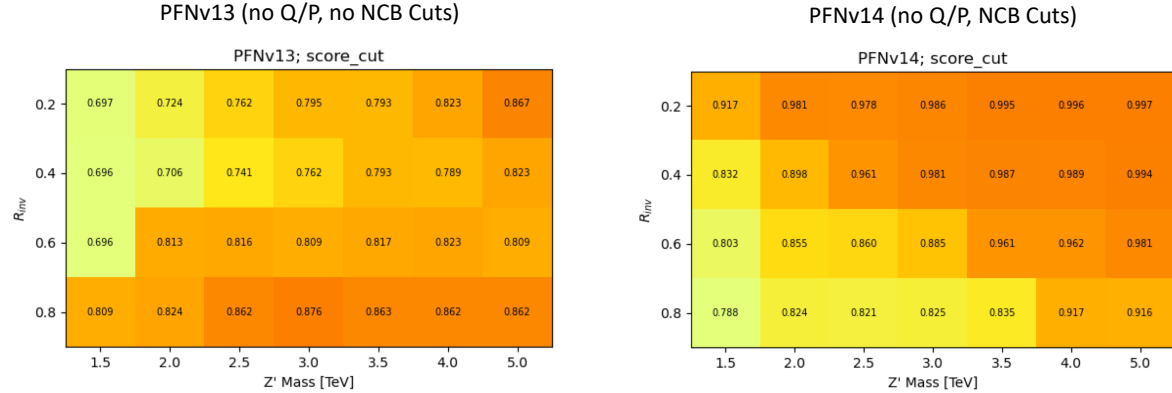


Figure B.5: Preferred cuts on the PFN score for each point in the grid, comparing the effect of adding the NCB preselection.

2128
2129 Grid cans for optimality were also performed on the number of training epochs, number of
2130 training events, batch size, learning rate, number of neurons, and dimension of the Φ space. The
2131 results of these scans are summarized in the tables in Figure B.6. The selected or default parameters
2132 were found to be optimal, or close enough to optimal to justify not increasing the training time or
2133 complexity of the network for negligible increases in performance.

2134 B.3 Supervised: BDT vs. PFN

2135 Studies of the BDT compared to the PFN performance, where training over events modeled
2136 with jet-related HLVs (high-level track variables, etas, angles, etc.) are compared to events mod-
2137 eled by the tracks of the 2 leading jets. Figure B.7 shows the performance of the BDT with and
2138 without explicit use of energy scale variables.

2139 B.4 Single Jet vs Jet System ML Approach

2140 The analysis considered both a single jet and jet system ML approach. A jet system approach,
2141 where the leading two jets and their orientation with respect to each other was selected for a variety
2142 of reasons. The jet system approach captures the MET information which is crucial to identifying

	default s_events=500096 b_events=501396	s_events:49135 b_events: 48220 *	s_events:246205 b_events:245136
AUC	.905	.874	.892

	default n_neuro n 40	n_neuro n 150	phi_dim 32	phi_dim 128	learning rate 0.0005	learning rate 0.002	nepochs 50	nepochs 200*	
AUC	.905	.898	.906	.902	.906	.898	.905	.893	.909

	default	batchsize_pfn 250	batchsize_pfn 1000
AUC	.905	.903	.902

Figure B.6: Scans done to check for optimality of PFN training parameters.

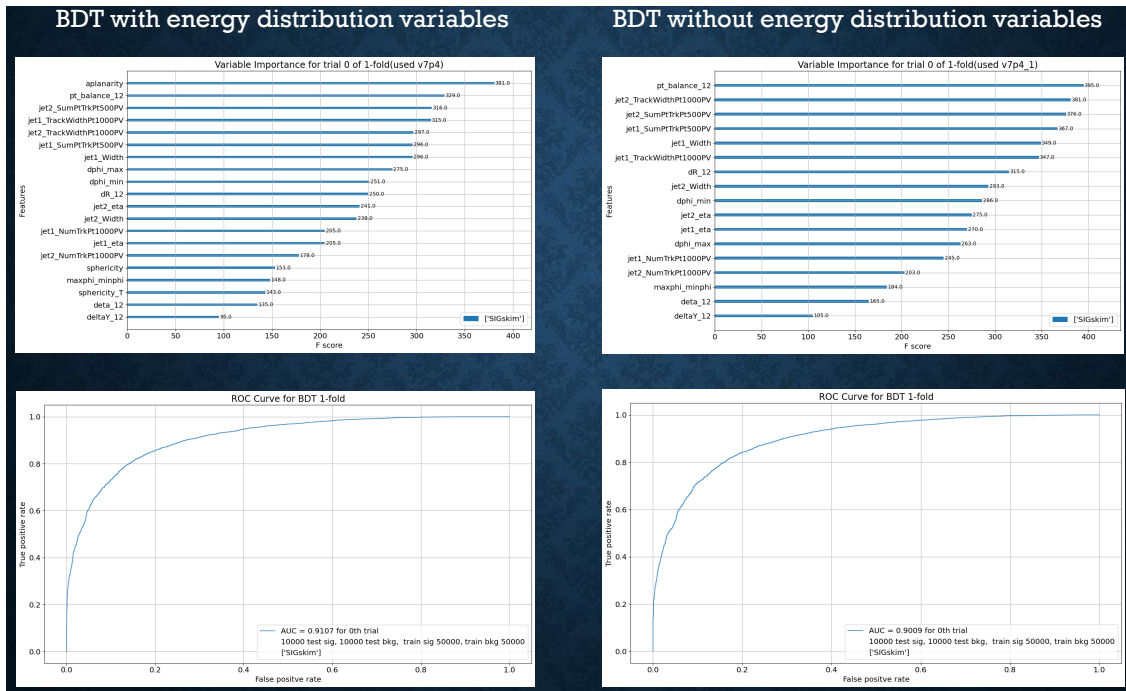


Figure B.7

2143 SVJs. In the topology where the dark quarks come from a heavy Z' decay and are back to back,
 2144 the measurable MET will have to be aligned with one or the other.

2145 Additionally, the performance of both a supervised PFN approach and an unsupervised AE ap-
 2146 proach was studied in the case of a single jet tagger. While the PFN approach was still performant
 2147 on a single jet case, the unsupervised approach was significantly improved by using both jets. This
 2148 is shown in Figure B.8.

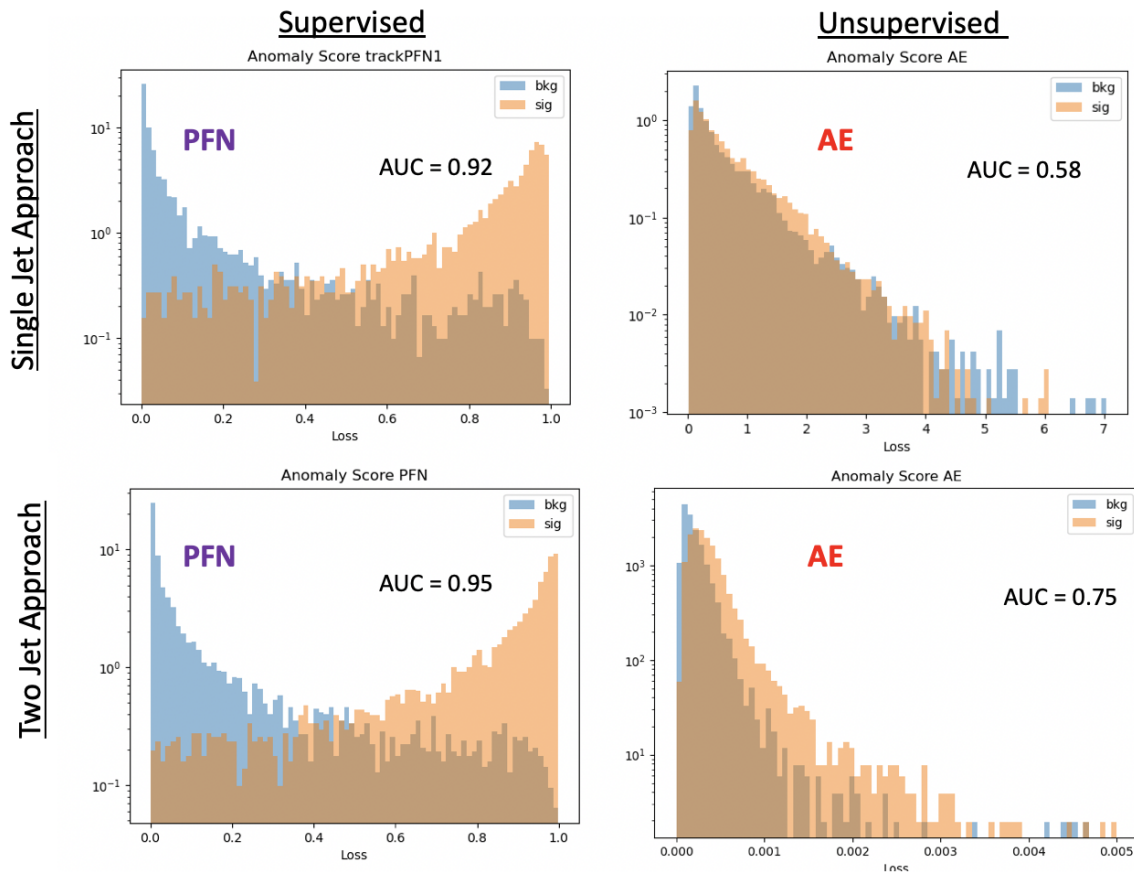


Figure B.8: ϕ Performance comparison between single jet and jet system ML approach

2149 B.5 PFN Training Composition

2150 The overall sensitivity and stability across the signal grid is observed to benefit by training
 2151 the ML tool to reject only the dominant background, QCD. This is evidenced by the PFN response
 2152 plots shown in Section 7.1.1 and the following AUC and sensitivity comparison plots in Figure B.9.

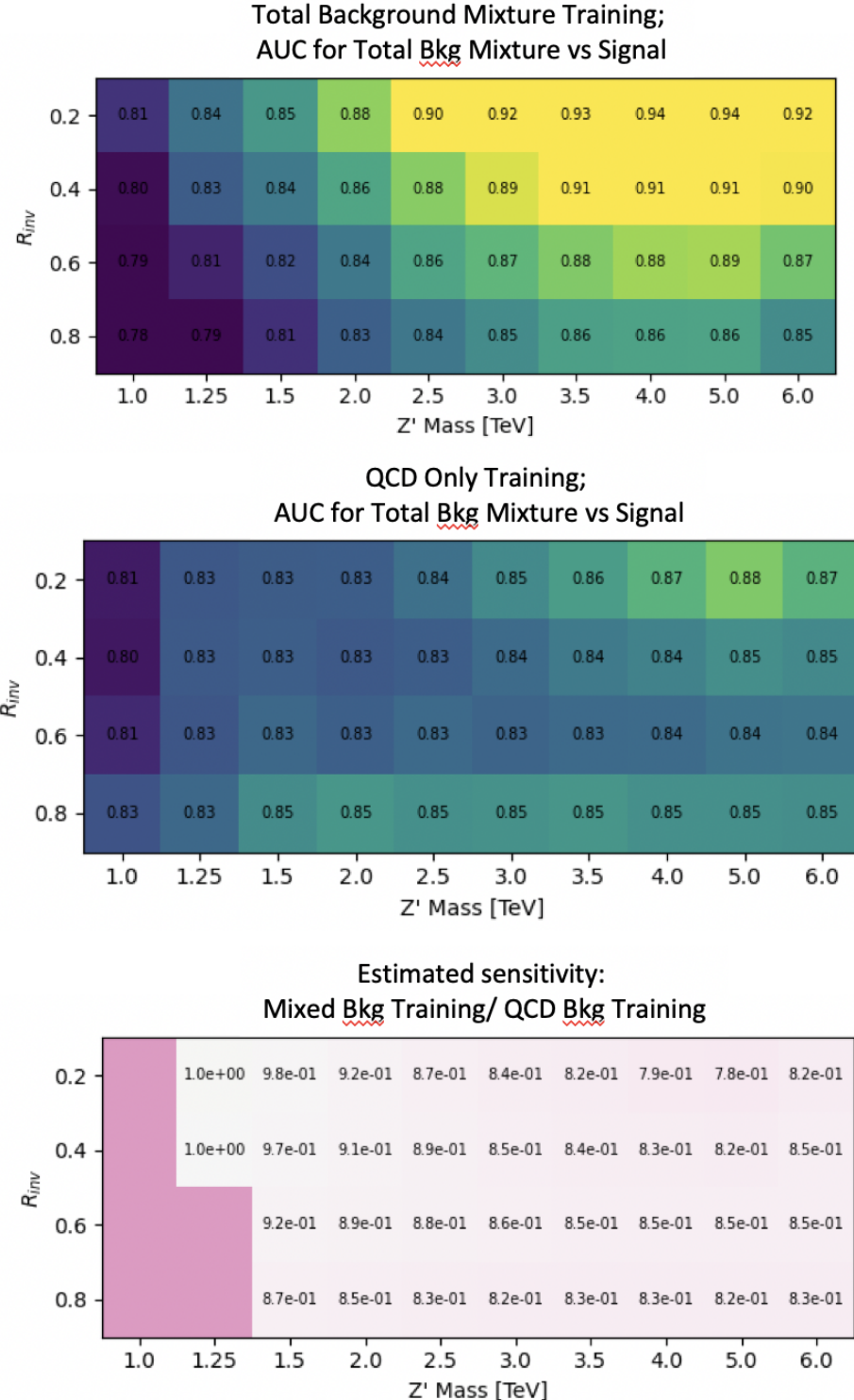


Figure B.9: ϕ Comparison in the AUC score across the grid for the mixed background strategy vs the QCD only strategy. The bottom table highlights that the QCD only strategy gives superior sensitivity across the signal grid.

2153 **B.6 E_T^{miss} and $E_T^{\text{miss}}\phi$ Shapes**

2154 The Tight cleaning working point was found to be necessary due to the nature of our signal
 2155 being E_T^{miss} and hadronic activity that are closely aligned, presenting a signature that is very af-
 2156 fected by beam-induced background (BIB). As per the cleaning recommendations, any event with
 2157 a jet that fails Tight criteria is rejected. Figure B.10 shows the effect of Tight cleaning on the shape
 of E_T^{miss} in data, fixing a feature present in Loose cleaning only.

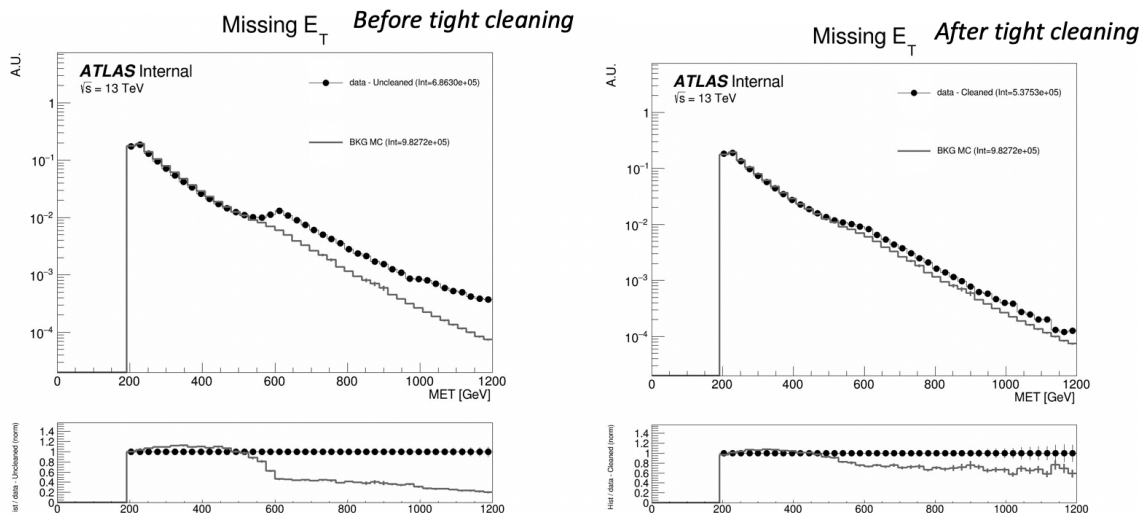


Figure B.10: E_T^{miss} in data before and after Tight event cleaning is applied.

2158
 2159 Figure B.11 further illustrates the correlation between the excess events and the leading jet p_T ,
 2160 and illustrates the impact of the tight cleaning in reducing this feature.

2161 Figure B.12 illustrates the 2D η vs ϕ distribution of the leading and subleading jets before and
 2162 after tight cleaning. No major spikes or hot areas are observed. One bright spot in the subleading
 2163 jet map at $\eta \approx 0$ and $\phi \approx -1.0$ was studies and found to have no impact on the E_T^{miss} shape, indicating
 2164 a likely missed spot in the Tile cleaning which does not affect E_T^{miss} .

2165 **B.6.1 NCB Preselection**

2166 A final preselection was derived to entirely remove the presence of non-collision background,
 2167 particularly noted through its impact on the E_T^{miss} shape. Cuts are added on the subleading jet

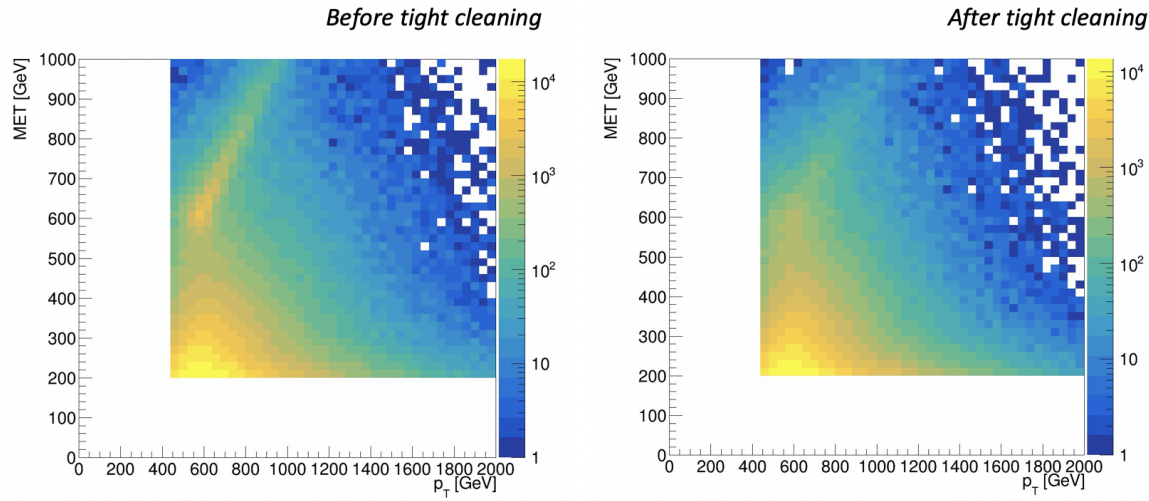


Figure B.11: E_T^{miss} vs jet1 p_T in data before and after Tight event cleaning is applied.

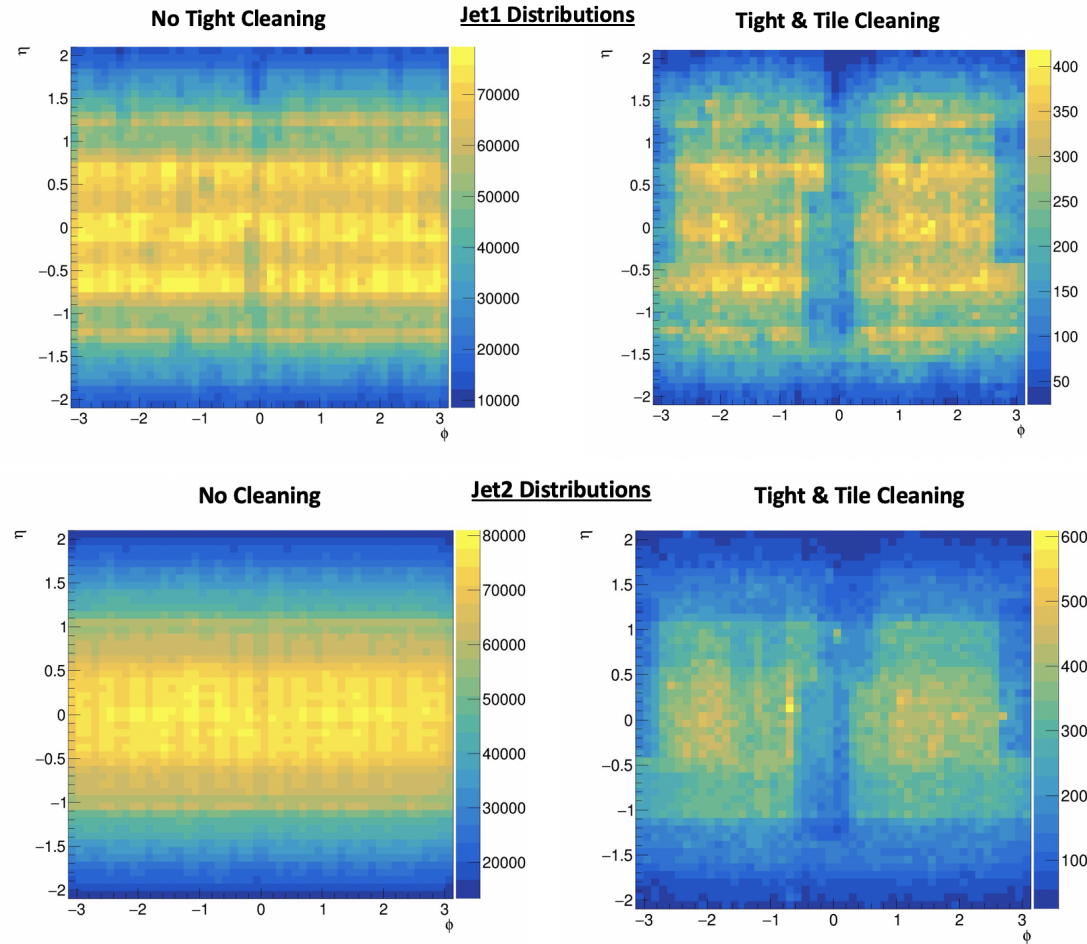


Figure B.12: η vs ϕ for leading and subleading jets, before and after the application of tight cleaning.

2168 $p_T > 150$ GeV and $\Delta\Phi(j1,j2) > 0.8$. Figure B.13 shows the impact of these cuts to create a fully
 2169 smoothly falling E_T^{miss} distribution. Figure B.14 shows the impact on the data yields in the CR and
 2170 VR and several signals in the SR; the greatest inefficiencies are found for the signal points that are
 2171 not sensitive in the analysis anyway. The reduction in background ultimately means that no impact
 is noticed on the limits.

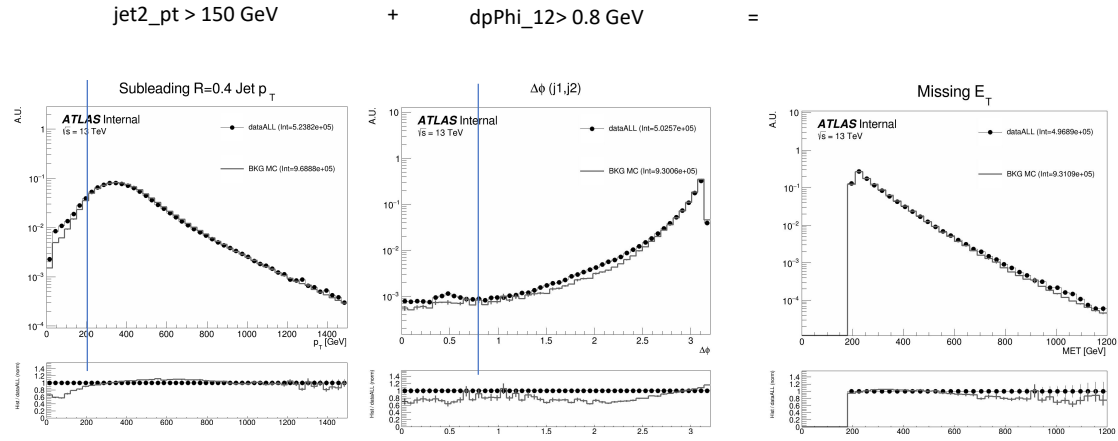


Figure B.13: Added NCB preselection and impact on E_T^{miss} shape.

2172
 2173 Figure B.15 shows the impact of these cuts on the 2D E_T^{miss} vs jet1 p_T distribution, where the
 2174 feature is also observed to be smoothed.

2175 This strategy was discussed and signed off by the Jet/ E_T^{miss} CP group ¹.

2176 B.6.2 TileCal Correction

2177 The $E_T^{\text{miss}}\phi$ distribution was fixed through the implementation of an offline TileCal correction
 2178 tool, which removes certain lumiblocks of certain runs based on poor functioning in TileCal mod-
 2179 ules. Figure B.16 shows the $E_T^{\text{miss}}\phi$ distribution in data across runs, before and after the application
 2180 of the tool, showing the ability of the tool to remove spikes due to instrumental problems.

¹<https://indico.cern.ch/event/1413217/>

Region	Before Extra Cleaning Cuts	After Extra Cleaning Cuts	Efficiency
Data - CR	108957	107435	0.99
Data - VR	116917	116008	0.99
2500, 0.2 - SR	1921	1709	0.89
2500, 0.4 - SR	1819	1424	0.78
2500, 0.6 - SR	1150	735	0.64
2500, 0.8 - SR	543	251	0.46
5000, 0.2 - SR	21.5	20.3	0.94
5000, 0.4 - SR	22.3	19.4	0.87
5000, 0.6 - SR	16.0	11.6	0.73
5000, 0.8 - SR	8.1	4.1	0.51

Figure B.14: NCB preselection impact on data and signal yields.

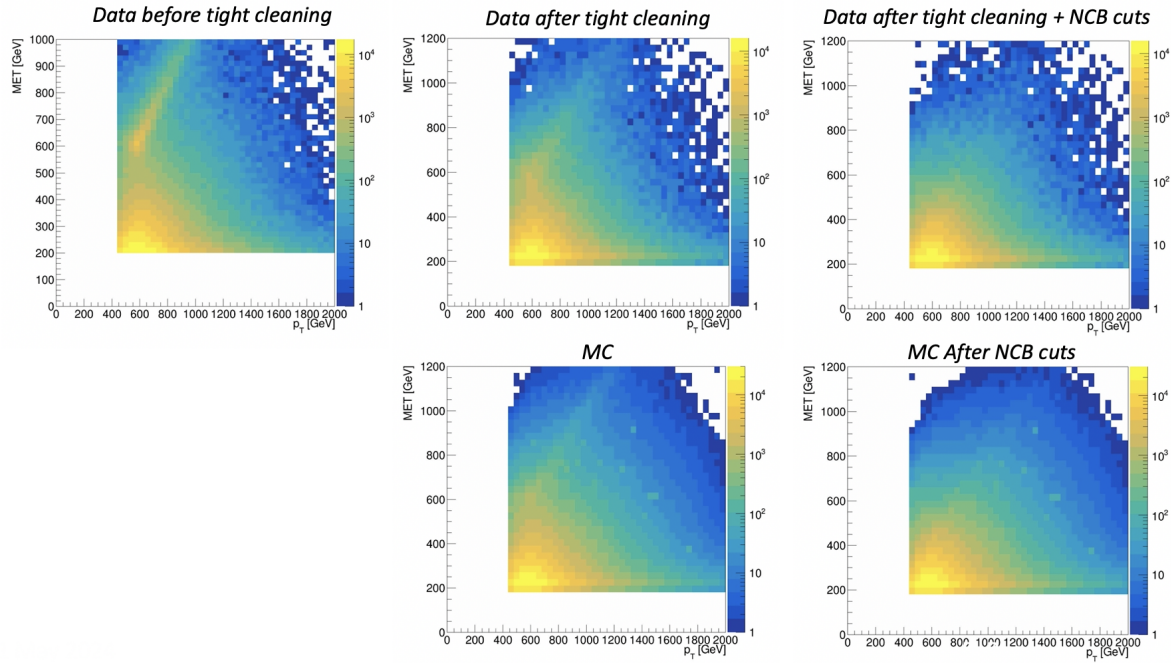


Figure B.15: Impact of tight cleaning and non-collision background preselection.

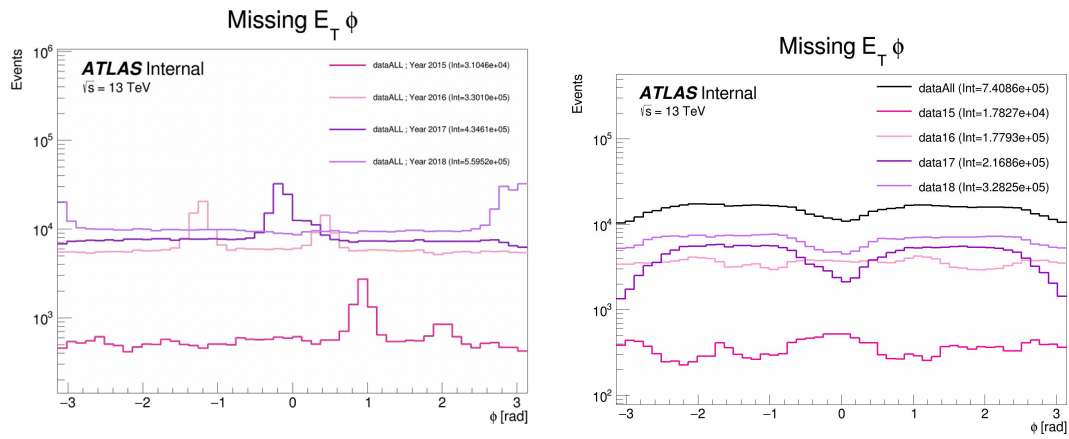


Figure B.16: $E_T^{\text{miss}}\phi$ in data, before (left) and after (right) application of the TileCal correction tool.

2181

2182

Appendix C: Truth Studies

2183 C.1 Jet dR Matching

2184 Figure C.1 demonstrates that the leading and subleading jet are overwhelmingly the most likely
2185 jets to be matched to a dark quark.

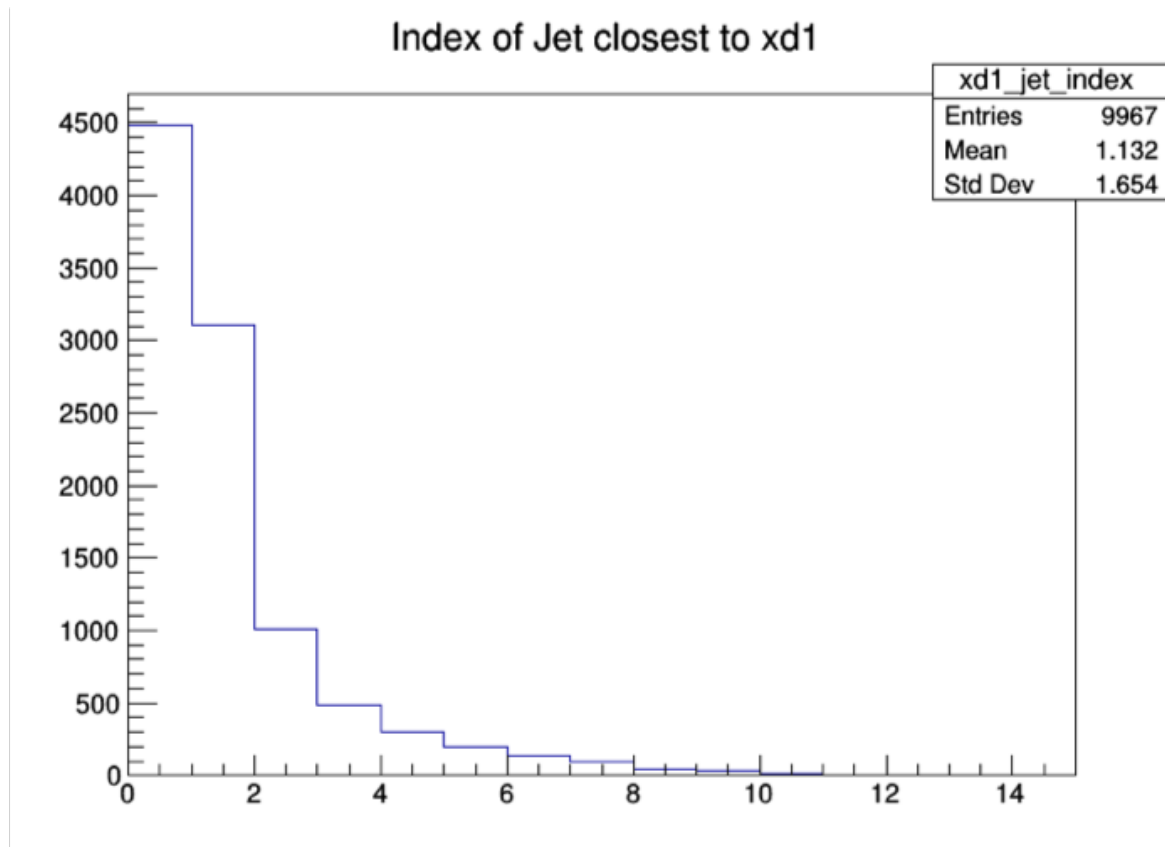


Figure C.1: Index of jets truth matched (by requirement of $\Delta R < 0.4$) with dark quark.

2186 Other matching strategies were explored, such as choosing the jet most aligned with $E_T^{\text{miss}}(\min$
2187 $\Delta\phi(j, E_T^{\text{miss}}))$ and the jet most anti-aligned with $E_T^{\text{miss}}(\max \Delta\phi(j, E_T^{\text{miss}}))$. However, in most cases
2188 these two measurements correspond to the subleading and leading jets respectively. Additionally,
2189 as shown in Figure C.2 the leading/subleading strategy generally results in more matched jets than

2190 the E_T^{miss} aligned and E_T^{miss} anti-aligned strategy. Therefore the leading and subleading jets were
 2191 chosen for consideration in this analysis.

Signal ($M_{Z'}$, r_{inv})	% Leading Jets dR Matched	% MET anti- aligned Jets dR matched	% Subleading Jets dR Matched	% MET aligned jets dR matched
750 GeV, 0.2	0.432883	0.3567	0.3777	0.3504
750 GeV, 0.8	0.187819	0.1589	0.1826	0.1803
3500 GeV, 0.2	0.692931	0.5408	0.5097	0.4144
3500 GeV, 0.8	0.344057	0.2927	0.2634	0.2585
6000 GeV, 0.2	0.647237	0.5047	0.4975	0.3919
6000 GeV, 0.8	0.345542	0.2882	0.2517	0.249

Figure C.2: Percent of jets with $\Delta R(j, E_T^{\text{miss}}) < 0.4$ comparing two jet identification strategies. Leading and subleading jets are seen to be the better metric for identifying jets associated with the dark quark decay.

Appendix D: BumpHunter

2194 D.1 Signal Mass Resolution m_T Binning

2195 In the discovery region, a binning for m_T is determined that is based on the expected signal
 2196 width. This is done to improve the BumpHunter performance. The signal mass resolution for a
 2197 given point is determined with a double-sided Crystal Ball fit to the mass. These fits are performed
 2198 across Z' mass, and a linear fit to these values is performed to determine the optimal bin width
 2199 across m_T .

2200 The x-axis value used is a data-driven way to determine the appropriate value of m_T for a given
 2201 signal, given that the considerable E_T^{miss} from the dark particles means that the truth Z' mass does
 2202 not well approximate the peak m_T value. The E_T^{miss} in the final state is generally an underestimate
 2203 of the amount of energy that could be attributed to dark hadrons, as any dark hadrons that are
 2204 back-to-back in the transverse plane will cancel out and not register as E_T^{miss} . Therefore m_T is
 2205 always an underestimate of the Z' mass, so the truth Z' mass can be used as an upper bound. An
 2206 integral is then performed backwards from that value until 60% of the total signal yield is included.
 2207 This window is referred to as the 60% mass window; the mean of this window then provides an
 2208 approximate localization of the signal mass peak in m_T . Figure D.1 shows some examples of this
 2209 algorithm on several signal points of varying R_{inv} and mass.

2210 Figure D.2 shows the result of this linear fit for the four R_{inv} values considered in the signal
 2211 grid. As expected, the resolution is considerably different for low and high R_{inv} points.

2212 A single m_T binning for the final SR plotting and BumpHunting is determined by selecting a
 2213 harmonized binning at low m_T , and moving to wider bins at high m_T . As for higher R_{inv} signal
 2214 points the mass resolution linear fit gives negative results, we require each bin to have a width of
 2215 at least 100 GeV. Figure D.3 shows the resulting bins for each R_{inv} category that comes from the

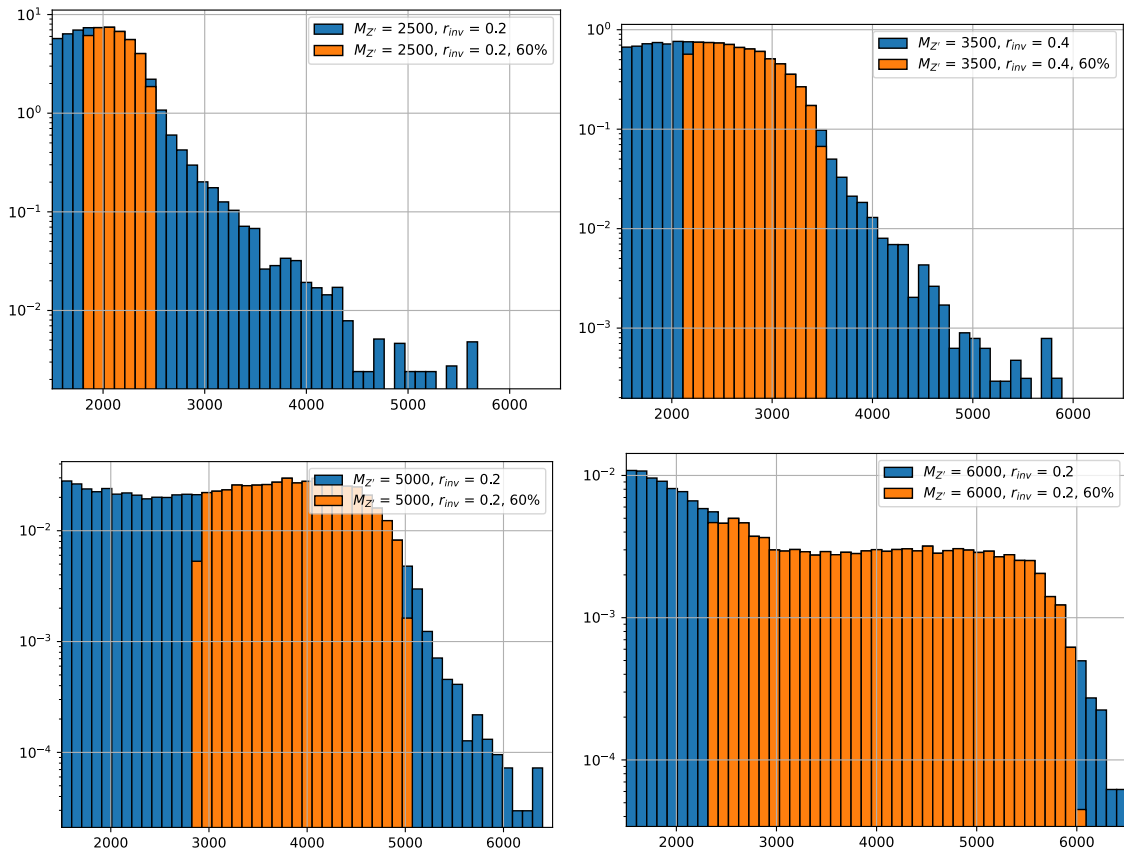


Figure D.1: Example determinations of the 60% mass window means for several signal points.

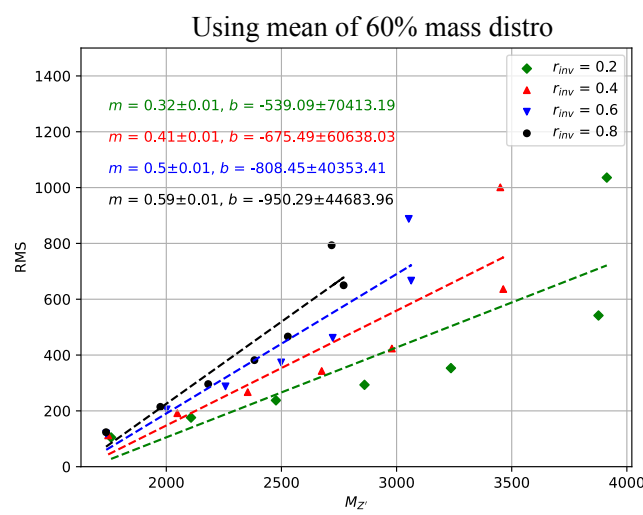


Figure D.2: Signal mass resolution for m_T binning for the signal grid in (R_{inv} , mass) space.

mass resolution fits, with the addition of the minimum 100 GeV bin width requirement.

$r_{inv} = 0.2 \rightarrow [1500, 1600, 1700, 1800, 1904, 2029, 2177, 2356, 2569, 2824, 3128, 3493, 3929, 4451, 5075, 5822, 6715]$

$r_{inv} = 0.4 \rightarrow [1500, 1600, 1700, 1800, 1910, 2053, 2238, 2477, 2787, 3187, 3704, 4374, 5240, 6361]$

$r_{inv} = 0.6 \rightarrow [1500, 1600, 1700, 1800, 1919, 2087, 2321, 2650, 3110, 3755, 4659, 5925, 7698]$

$r_{inv} = 0.8 \rightarrow [1500, 1600, 1700, 1800, 1927, 2117, 2400, 2823, 3455, 4400, 5811, 7918]$

Figure D.3: m_T bins based on the signal mass resolution and the minimum 100 GeV width requirement, for each R_{inv} signal category.

2216

2217 In order to have a final m_T binning that is not highly model-dependent, we consolidate these
2218 four different bins into a single binning which is provided below:

2219 **[1500, 1600, 1700, 1800, 1900, 2025, 2175, 2350, 2575, 2825, 3125, 3500, 3925, 4450, 5075,
2220 6000]**